Metal-insulator-metal nanoresonators for refractive index sensing

George Duffett

Doctor of Philosophy

University of York

Physics

June 2021

Abstract

Personalised healthcare, local environmental monitoring and food quality control drive the need for compact, cost-effective, reliable methods for detecting specific molecules. Resonant refractive index sensors can detect these molecules binding to their surfaces with label-free measurements. The resonators have a small device footprint which is ideal for miniaturisation and they are easily integrated with electronic systems through ubiquitous optoelectronic components.

These resonant refractive index sensors have evanescent fields which probe the detection layer. Their sensitivity is often optimised by maximising bulk sensitivity, which favours spatially extended modes. This strategy is not necessarily suitable for maximising biomolecule detection. The more relevant consideration is the sensitivity to changes within a molecule-length of the surface.

In this work, I show that high surface sensitivity can be achieved by tightly confined resonant modes in metal-insulator-metal (MIM) structures, which have relatively high surface sensitivity despite low bulk sensitivity compared to other resonant modes. I achieve 55 nm/RIU sensitivity to a 10 nm layer with lithographically fabricated arrays of third-order MIM resonators, approximately twice as high as that of an extended SPP mode also supported by the periodic array. I increase the MIM surface sensitivity by accessing the first order MIM mode with bottom-up methods and estimate 65nm/RIU sensitivity from displacing a ~3nm polymer capping layer. I complement the nanocube MIM resonators with a readout assembly using low-cost optoelectronic components which achieves a 5.7×10^{-4} RIU or 3.7×10^{-3} RIU bulk limit of detection when controlled by either research-grade or low-cost electronics respectively.

The simulations and experiments in this work emphasise the importance of surface sensitivity as a performance metric. The nanocube structures present a powerful sensing modality which achieves high surface sensitivity and forms an integral part of the low cost hand-held sensing assembly. These design considerations and prototypes inform the next generation of optical biosensors.

Table of Contents

List of Figures

Acknowledgements

I express my sincerest gratitude to the people who helped and encouraged me over the past the four years. The time, skills and knowledge they shared enabled me to accomplish this work.

First and foremost, I thank my supervisor, Professor Thomas Krauss, for his academic support and advice throughout this project and from whom I have learnt much that I will carry with me for the rest of my career.

I thank my examiners, Dr Ali Adawi and Dr Chris Murphy, whose constructive comments and corrections have added significant value to the thesis.

I also thank Dr Ralph Wirth and Dr Mathieu Rayer from OSRAM GmbH for meeting me on the bridge between academia and industry, discussing project management, implementation and providing useful feedback during many enjoyable phone calls.

I extend my gratitude to Professor Emiliano Martens for discussing theory and modelling in the early stages of the project, Dr Steven Johnson for providing vital feedback on the surface chemistry in the later stages of the project and Dr Matthew Simmons for teaching me how to design and assemble microfluidics.

I thank Christopher Reardon and Adam Stroughair for training me to use the cleanroom equipment and getting me started on much of the fabrication for this project.

Informal conversation extended my formal supervision and the discussions were often edifying and enlightening. For these discussions in a good-natured atmosphere, I thank Dr Casper Kuntsmann, Dr Ben Coulson, Dr Donato Conteduca, Dr Giampaolo Pitruzzello, Rhys Ashton, Dr Yue Wang, Dr Kezheng Li, Dr Lewis Reeves, Dr Graham Triggs and Dr Daan Stellinga. In particular, I thank Alex Drayton and Callum Silver, alongside whom it was a privilege to study.

Manuel Deckart, Joshua Male, Kalum Thurgood-Parkes and Dr Augusto Martins deserve a special mention for, among a great many things, their good humour and spirited discussions.

I am deeply grateful to my family for their emotional support during this project.

Declaration of Authorship

I, George Duffett, declare that this thesis titled Metal-insulator-metal nanoresonators for refractive index sensing is a presentation of original work and I am the sole author.

- This work was done wholly while in candidature for a research degree at this University.
- This work has not previously been presented for an award at this, or any other, University.
- All sources are acknowledged as References.
- I have acknowledged all main sources of help.
- Published work included within this thesis is indicated in the list below.

George Duffett

Publications:

- G. Duffett, R. Wirth, M. Rayer, E. R. Martins, and T. F. Krauss, "Metal-insulator-metal nanoresonators - Strongly confined modes for high surface sensitivity," *Nanophotonics*, vol. 9, no. 6, pp. 1547–1552, 2020.
- M. Rayer, T. F. Krauss, and G. Duffett, "Sensor arrangement, method for detecting molecules and method for forming a sensor arrangement," Patent Number: DE102018212243A1, 2020.

Other communications:

- Physics of Life Summer school 2018, Durham, Poster
- Metamaterials and nanophotonic structures in applications Summer School 2018, Karlsruhe, Poster

Chapter 1

Introduction and scope

Healthcare, environmental monitoring and food quality control require detecting specific molecules. For example, the spread and severity of infections can be dramatically reduced by detecting them early with antibody tests. These molecules of interest are found on a ~10nm length scale, 7 or 8 orders of magnitude smaller than everyday objects in our lives. Correspondingly, the changes caused by these molecules are also too small for people to ordinarily perceive. In order to gain information on this length scale, these changes must be transduced to signals measurable by people and digital equipment.

One such method to observe changes on a 10nm length scale is light. Separate colours appear distinct to the human eye but the wavelength change which corresponds to a perceivable colour change can be tens of nanometres, the length scale on which we wish to interrogate these molecular interactions. These colour changes may be used to determine properties via molecules which change colour when exposed to a property of interest. For example, a litmus test causes an indicating substance to change colour to determine whether the analyte is acidic or basic.

Emission of light may be used to detect the presence of a target molecule by using fluorescent labels. Fluorophores may be attached either to the biomolecule of interest or a molecule used to detect it. This fluorescence emission provides excellent signal-to-noise ratio but the process of adding fluorescent labels largely restricts this method to the laboratory setting.

Point-of-care or in-field applications require a simple, miniaturised devices which do not use labels. Specific molecules are bound to a surface by functionalising this surface with a selective layer to which only the target molecule binds, a research area in itself. This surface may be that of a resonant structure. Light trapped in the resonant structure probes this functionalised surface and bound target molecules change the resonance condition which provides the readout method. These resonant

structures transduce the small refractive index change caused by molecular binding to a measurable change in the resonance wavelength. In other words, these resonant structures are refractive index sensors.

The core research question of this thesis is: **How well do metal-insulator-metal nanoresonators perform as refractive index sensors for detecting molecules?**

This broad question contains within it smaller and more accessible questions of these metal-insulator-metal (MIM) resonators and their application to refractive index sensing for detecting the presence of molecules:

- How sensitive are MIM structures to refractive index changes within a (bio) molecule's length of their surfaces?
- Through what physical principles do MIM resonators acquire sensitivity to their surroundings?
- What are the best methods and crucial parameters to fabricate resonant MIM cavities?
- How sensitive are MIM structures to refractive index changes in their bulk surroundings?
- How can changes in the resonance wavelength be measured with low-cost components?
- How should the next researcher approach functionalising these resonator surfaces?

These questions are explored throughout the thesis with a complementary combination of simulations and experiments. Both the simulation and experiments consider MIM resonators fabricated by top-down lithography and bottom-up methods using nanocubes, both represented in figure 1.1. The scope of the thesis chapters is outlined below.

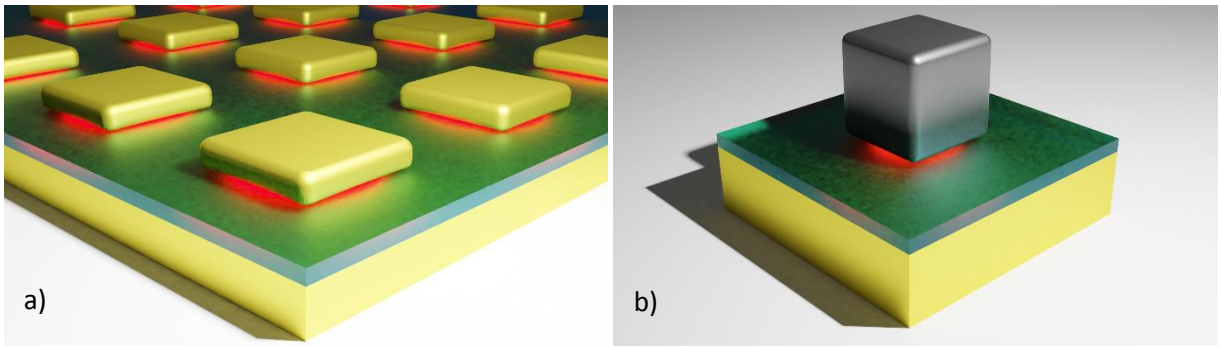

Figure 1.1. Artistic representation of MIM structures. a) Lithographically fabricated and b) nanocube based MIM resonators.

Chapter 2 provides context for the work. The work requires context from two areas. The first area is the underlying principles of plasmonics, including analytical results relating to surface plasmon

polaritons and MIM waveguides from which the MIM resonance emerges. These principles aid understanding of the second area: the state of the art, and performance metrics of prominent refractive index sensors, to which the MIM refractive index sensor will be compared.

Chapter 3 explains the methods used to design, fabricate and characterise MIM structures which are common to experiments throughout the rest of the thesis. The underlying principles of the computational tools are discussed, including their relative strengths and limitations. The deposition techniques for fabricating the bottom metal-insulator layer are presented, with a discussion of surface roughness which is crucial for fabricating MIM stacks. The MIM structures in chapters 5, 7 and 8 are characterised with an optical setup, also presented in this chapter. The two different patterning methods which form the top metal layer (lithography and nanocubes) are presented with their corresponding experimental results.

In **Chapter 4**, the lithography structures' design parameters are optimized with computational tools. These computational tools allow the sensing performance to be simulated and provide insight into origin of the MIM's high surface sensitivity. The design considerations presented in this chapter inform the fabrication process in chapter 5.

Chapter 5 describes the electron-beam lithography fabrication processes and experimental bulk and sensitivity performance for regular arrays of MIM resonators. The chapter presents experimental results which determine the bulk and surface sensitivity of these structures and concludes with the limitations of this fabrication process and areas in which the process requires improvement.

Chapter 6 models the tunability and sensitivity of isolated nanocubes on metal-insulator substrates with an eigenmode tool, particularly suited to such isolated plasmonic resonators. These simulations provide an experimental method of tuning the nanocube MIM resonance, despite the nanocubes' fixed width. The chapter discusses a semi-analytical prediction which quantitatively links the evanescent electric field with sensing performance and concludes with simulated bulk and surface sensitivity results.

Chapter 7 determines the bulk sensitivity of the nanocube MIMs through experiments. These results rely on fabricating the nanocube MIMs through bottom-up methods, which begin the chapter. Bulk sensitivity results obtained with a commercial spectrometer provide the benchmark for bulk sensitivity results from an intensity based setup. Both research-grade and low-cost versions of this intensity-based setup are presented.

Chapter 8 extends the sensing performance description of these nanocube MIM structures in chapter 7 to include their ability to detect changes at a molecular level. The experiments use two molecules with a known response: small mercapto-alcohol molecules and thiolated DNA molecules. I make surface sensitivity estimations from these molecular results, showing that these nanocube resonators achieve competitive surface sensitivity performance.

Chapter 9 concludes the work with explicit answers to the above research questions, evidenced by the designs, simulations and experiments in chapters 3 through 8. The chapter extends beyond these research questions by recommending development strategies for future MIM biosensors and their readout methods.

Chapter 2

Background

Plasmonic structures have already proved valuable for studying biochemical reactions [1] and for developing future point-of-care biosensors [2]. Before investigating their sensing abilities, I provide an overview of important concepts and relations in plasmonics as a distinct field of study. The section describes plasmonics in terms of basic principles rather than by duplicating rigorous derivations from a textbook [3] and by quoting the key results and the boundary conditions from which they arise.

2.1 Maxwell's equations

The customary starting point for classical descriptions of electromagnetic fields with matter is Maxwell's equations [3]:

$$\nabla \cdot \boldsymbol{D} = \rho_{ext}, \tag{2.1}$$

$$\nabla \cdot \boldsymbol{B} = 0, \tag{2.2}$$

$$\nabla \wedge \boldsymbol{E} = -\frac{\partial \boldsymbol{B}}{\partial t}, \tag{2.3}$$

$$\nabla \wedge \boldsymbol{H} = \boldsymbol{J_{ext}} + \frac{\partial \boldsymbol{D}}{\partial t}. \tag{2.4}$$

The four Maxwell equations describe the relationships between the electric field **E**, displacement field **D**, magnetic field **H**, magnetic induction **B** with currents and charges external to the materials, $\mathbf{J}_{ext}$ and ρ_{ext}. In this context, "external" refers to charges which drive the system as opposed to, for example, charges within materials which respond to external stimuli [3]. The electric and displacement fields are related by the relative permittivity of a material ε. Likewise, the magnetic field and magnetic induction are linked by the relative permeability μ. For linear isotropic media, the relations are:

$$\mathbf{D} = \epsilon_0 \epsilon \boldsymbol{E} \tag{2.5}$$

$$\boldsymbol{B} = \mu_0 \mu \boldsymbol{H} \tag{2.6}$$

In the absence of external charges and external current densities ($\rho_{ext} = 0$, $\mathbf{J}_{ext} = 0$), the two curl equations (2.3) and (2.4) may be combined using well-known vector identities to describe light propagation with the wave equation:

$$\nabla^2 E - \frac{\mu\epsilon}{c^2}\frac{\partial^2 E}{\partial t^2} = 0 \tag{2.7}$$

Where the permittivity and permeability of free space have been substituted for the speed of light in a vacuum c: $\sqrt{\epsilon_0 \mu_0} = \frac{1}{c}$. The materials in this work are nonmagnetic, so their relative permeability μ=1 and is fixed to unity for the remainder of this work. The wave equation can be simplified by assuming that the electric field has a harmonic time dependence $\boldsymbol{E}(\boldsymbol{r}, t) = \boldsymbol{E}(\boldsymbol{r})\mathrm{e}^{-\mathrm{i}\omega\mathrm{t}}$ where the wave oscillates with angular frequency ω. Substituting this time-harmonic dependence into the wave equation yields the Helmholtz equation:

$$\nabla^2 \boldsymbol{E}(\boldsymbol{r}) + k_0^2 \epsilon(\boldsymbol{r})\boldsymbol{E}(\boldsymbol{r}) = 0. \tag{2.8}$$

The Helmholtz equation has been further simplified by substituting the wave number $k_0 = \frac{\omega}{c}$. The distribution of the electric field $\boldsymbol{E}(\boldsymbol{r})$ is determined by the distribution of the permittivity $\epsilon(\boldsymbol{r})$**.** Thus, the Helmholtz equation is the starting point for calculating the electric field distribution as a function of the permittivity distribution in the analytical solutions presented later in this chapter and for the computational methods used in later chapters of this work.

2.2 Drude Model

In order to describe plasmonic devices, we must first be able to describe their constituent materials: metals. Electron behavior in solids is, in general, not trivial. Electrons and inter-atomic spacing fall well within the quantum regime. Despite the quantum length scale, metal permittivity can be modeled by classical forces acting on a negatively charged gas of electrons. This model is referred to as the Drude model and is particularly favoured for its analytical form and historical success in predicting metal permittivity sufficiently well.

The Drude model aims to link electron motion to a metal's macroscopic material properties. The conduction electrons in a metal are free to move against a background of positive metal ion cores. The electrons have a mass m^* which is adjusted from the standard electron mass to account for their motion between the positive ion cores. The electrons collide with the ion cores at a characteristic

frequency γ, proportional to their velocity $\dot{\boldsymbol{x}}$, which damps their oscillations. The electrons experience a force $m^*\ddot{\boldsymbol{x}}$ due to the electric field contained within incident light. We assume that this electric field has a time-harmonic dependence $\boldsymbol{E}(t) = \boldsymbol{E}\mathrm{e}^{-\mathrm{i}\omega\mathrm{t}}$. These terms are collected in the equation below [3]:

$$m^*\,\ddot{\boldsymbol{x}} + m^*\gamma\dot{\boldsymbol{x}} = -e\boldsymbol{E} \tag{2.9}$$

The time-harmonic electric field indicates a time-harmonic solution of the form $\boldsymbol{x} = \boldsymbol{x}_0\mathrm{e}^{-\mathrm{i}\omega\mathrm{t}}$, which provides the general solution:

$$\boldsymbol{x}(t) = \frac{e}{m^*(\omega^2 + i\gamma\omega)}\boldsymbol{E}(t) \tag{2.10}$$

The electron, or charge, displacement is expressed as a macroscopic polarization field $\boldsymbol{P} = -ne\boldsymbol{x}$ which contributes to the displacement field $\mathbf{D} = \epsilon_0\mathbf{E} + \mathbf{P}$:

$$\boldsymbol{D} = \epsilon_0\left(1 - \frac{\omega_p^2}{\omega^2 + i\omega\gamma}\right)\boldsymbol{E} \tag{2.11}$$

where the electron charge *e*, density *n* and mass *m* have been incorporated into the plasma frequency $\omega_p^2 = \frac{ne^2}{\epsilon_0 m^*}$. The term in brackets is simply the material permittivity as a function of frequency:

$$\epsilon = 1 - \frac{\omega_p^2}{\omega^2 + i\omega\gamma} \tag{2.12}$$

This model is made comparable to experimental data [4] by considering two extra contributions to the permittivity: the polarization of the positive ion cores and of the electrons undergoing inter-band transitions. Positive ion cores still have bound inner shell electrons. While these inner shell electrons remain bound to the ion cores, they still undergo a small displacement to create a polarized environment. This additional polarization from the ion cores manifests itself as an offset ε_∞ to the permittivity. Real metals also have energies at which an electron may be promoted from a lower energy band to a higher energy band: an interband transition. This energy absorption is represented in the classical model as a restoring force $m\omega_0^2\boldsymbol{x}$ which has a resonance at frequency ω_0, i.e. the frequency at which the interband transition occurs. These two additions extend the Drude model to the Drude-Lorentz model:

$$\epsilon(\omega) = \epsilon_\infty\left(1 - \frac{\omega_p^2}{\omega^2 - \omega_0^2 + i\omega\gamma}\right) \tag{2.13}$$

where here I give only a single Lorentz oscillator (or pole) in order to most clearly demonstrate the physics. A model may be extended to include N Lorentz poles, each representing an inter-band transitions at a given frequency ω_n.

Figure 2.1 compares the metal permittivities from experimental data [4] with Drude parameters found in the literature [5] between 500nm and 1000nm, the bandwidth within which the optical simulations and experiments in this work took place. The Drude-Lorentz model shows good agreement with silver and gold, the two metals used in this thesis. In order to achieve this congruency, silver requires a single Lorentz pole and gold requires two Lorentz poles to represent the corresponding inter-band transitions. The analytical nature of the Drude-Lorentz model makes it easy to insert into frequency-domain simulations [5]–[8]. The agreement between the Drude-Lorentz model and experimental data becomes worse at approximately 500nm because of the interband transition which occurs in gold, giving the metal its distinctive colour.

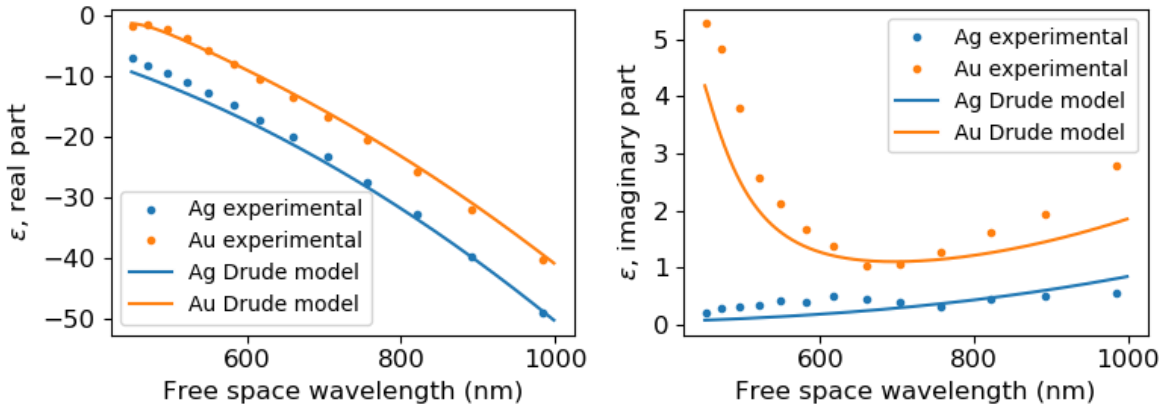

Figure 2.1. Comparison between Drude-Lorentz model and experimental data from ref [4] using Drude Lorentz parameters from the literature, ref [5].

2.3 Metal-dielectric interfaces

I extend the description of the Drude model in which charges oscillate in the metal bulk, to a description of charges oscillating on metal surfaces. These surface charge oscillations are called surface plasmons and they have two categories: propagating and localised. Propagating surface plasmons are supported by flat metal surfaces a schematic of which is shown in figure 2.2a. A single interface is described in section 2.3.1 then two interfaces are brought together to form a metal-insulator-metal heterostructure in section 2.3.2. In contrast, localized surface plasmon resonances are observed in discrete metal features, such as gold nanoparticles or discrete features in a patterned

metal film. The charges in the discrete metal feature oscillate in response to an external oscillating electric field shown in figure 2.2b. These discrete metal features form the top-most layer of a metal-insulator-metal cavity, described in 2.4.

2.3.1 A single interface

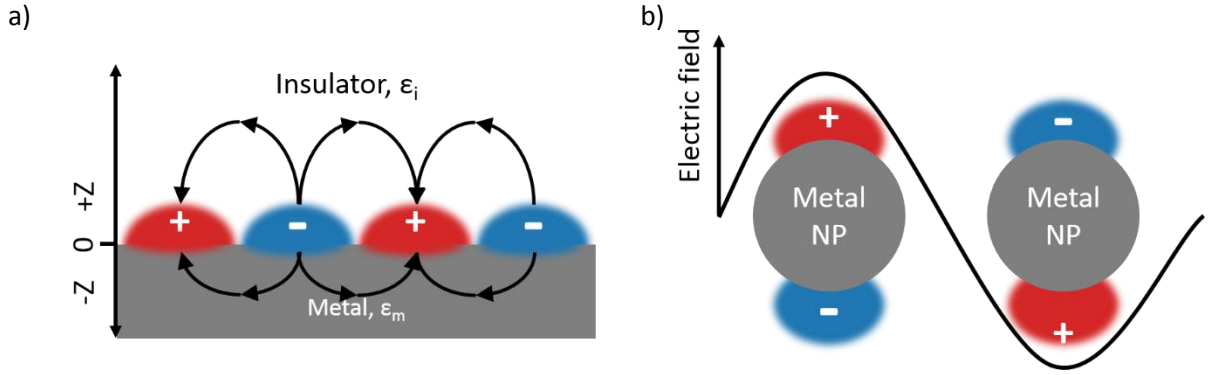

Figure 2.2. a) Schematic of geometry supporting a propagating surface plasmon, where the insulator space above the metal film extends to +∞ in the z direction and the metal extends to +∞ in the z direction. b) Localised surface plasmon resonance in a metal nanoparticle (NP).

The simplest geometry which supports surface plasmon polaritons (SPPs) is a single interface between a metal and an insulator. This geometry consists of a perfectly flat interface between a metal half-space (z<0) described by a negative complex dielectric constant ε_m, and a dielectric half-space (z>0) described by a positive real dielectric constant ε_i and shown in figure 2.2a.

We start with the Helmholtz equation (2.8), into which the metal-insulator geometry and material properties are inserted. The solution describes a propagating wave at the metal-dielectric interface. The H_y field amplitudes at the interface must be equal. Enforcing this continuity yields an analytical dispersion relation:

$$\beta = k_0 \sqrt{\frac{\epsilon_m \epsilon_i}{\epsilon_m + \epsilon_i}} \tag{2.14}$$

Where k_0 is the free space wavenumber at a given free space wavelength λ_0, $k_0 = 2\pi/\lambda_0$ and β is the component of the wave vector in the direction of propagation, or "propagation constant". This dispersion relation, for an air/silver interface, is plotted in figure 2.3a using Drude model parameters for silver from ref [7]: permittivity offset $\varepsilon\infty = 1$, plasma frequency, ω_p, = 1.35x10^{16} rad/s corresponding to λ_p = 138 nm in vacuum, damping term $\gamma = 0.0023\omega_p$ and no interband transition frequency: $\omega_0 = 0$. The gradient of this dispersion relation indicates the group velocity $\left(v_G = \frac{\mathrm{d}\omega}{\mathrm{d}k}\right)$ of

the wave, where a shallower gradient indicates that the wave is propagating more slowly. The effective refractive index, which indicates the phase velocity of the wave $\left(v_p = \frac{c}{n_{eff}}\right)$ is $n_{eff} = \beta/k_0$.

The SPP propagation constant β increases with frequency as the incident light couples to natural oscillations in the electron plasma and the wave takes on a more static "surface plasmon" character at the surface plasmon frequency ω_{sp}.

$$\omega_{sp} = \frac{\omega_p}{\sqrt{1+\epsilon_i}} \tag{2.15}$$

At frequencies above the Drude model plasma frequency ω_p corresponding to a plasmon wavelength λ_p = 138nm, the metal becomes transparent and consequently, the wave is no longer confined to the metal-insulator interface; this is apparent from the fact that its dispersion curve is now to the left of the light line in air, so no longer bound to the air-interface.

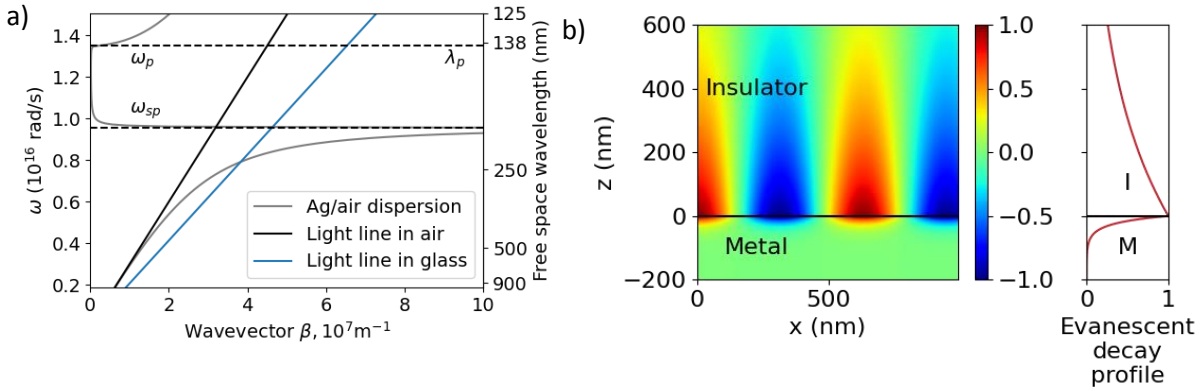

Figure 2.3. Surface plasmon polariton dispersion relation and field profile. a) Silver/air surface plasmon dispersion relation compared to the light line in air and glass. b) Field profile in 3D and 2D for silver SPP at 650nm free-space wavelength showing how the field decays over a smaller length in the metal than the insulator.

The wave decays exponentially into both the metal and the insulator half-spaces as it propagates, as shown in figure 2.3. The decay length of the wave is given by $1/|k_j|$ where k_j is the component of the wave vector perpendicular to the metal/insulator interface and the index j corresponds to either the metal *m* or insulator *i*. The wave vectors are given by the expression:

$$k_j^2 = \beta^2 - k_0^2\epsilon_j \tag{2.16}$$

which states the decay length depends on the material into which the wave decays. For example, when SPPs are excited with free space wavelength 650nm at an air/silver interface, the characteristic decay length is ~450nm into the air and only 23nm into the silver as can be seen in figure 2.3b. The

total field on the dielectric side is larger (positive z values in figure 2.3b), because there is so little field in the metal (negative z values in figure 2.3b) – hence their bulk sensitivity is higher.

Now that surface plasmon resonances have been established in theory, it is important to comment on how to couple to them in practice. The physical concept behind the coupling process is to make sure that the energy (frequency) and momentum (wave vector) of the incident light match a point on the SPP dispersion. These intersections can be readily identified in the dispersion diagram. For example, light in air below 800THz will not couple to a silver/air SPP because the air light line does not intersect the silver/air dispersion relation.

The dispersion relation in figure 2.3 also shows the light line for glass, which does indeed intersect the air/silver SPP dispersion. Forming an arrangement of light incident from glass onto a silver film therefore achieves the momentum matching required to excite an SPP. A suitable coupling configuration may be realised by depositing a thin (~50nm) silver film onto a glass prism to form the air/silver and air/glass interfaces. This prism configuration is known as the Kretchmann configuration and is commonly used in surface plasmon resonance biosensing [1], [9]

Another method to match the k-vector of the incident light is a grating. The grating itself is described by a vector, $G = \frac{2\pi}{a}$, where a is the grating period and it supports diffraction orders m. The coupling condition is:

$$\beta = k_{inc} \sin(\theta) \pm mG \tag{2.17}$$

Where light is incident from a medium with refractive index n_{inc} with wave number $k_{inc} = n_{inc} \frac{2\pi}{\lambda}$.A grating reshapes the phase front, so the diffracted order may match the coupling condition for an SPP. While including a grating overcomes the momentum mismatch between the incident light and the SPP, the presence of the grating also perturbs the system. Due to this perturbation, the resulting SPPs deviate from the analytical dispersion relation and coupling condition above.

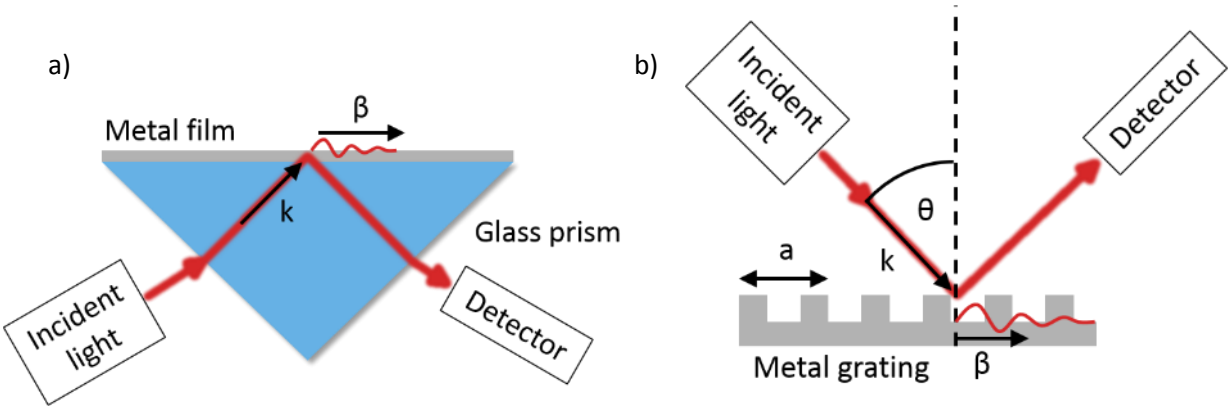

Figure 2.4. Techniques for coupling to SPPs by matching the k-vector of the indecent light. a) Prism coupling in the Kretschmann configuration using the refractive index of glass to match k-vectors. b) Grating coupling by using the period of features to match the k-vector of incident light to the k-vector of a SPP.

2.3.2 Two metal interfaces

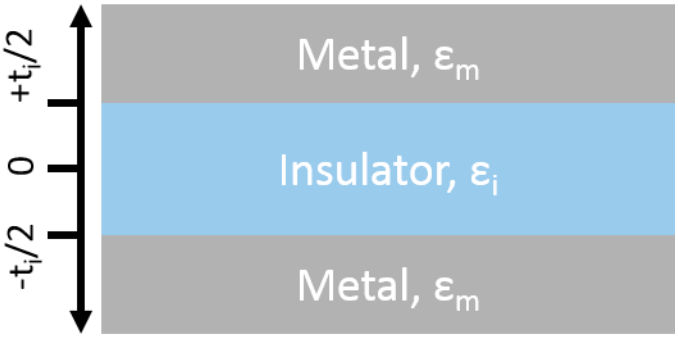

Figure 2.5.Schematic of MIM stack geometry wherein the metal slabs extend to infinity in the vertical direction either side of a finite insulator layer with thickness t_i. The stack is homogeneous in the horizontal directions.

The single-interface SPP model can be extended to two metal-insulator interfaces shown in figure 2.5. These two metal-insulator interfaces can be brought together so that the surface plasmons at one interface interact with and couple to the surface plasmons supported on the other interface. This two-interface geometry may be arranged in two ways: a metal-insulator-metal (MIM) stack or an insulator-metal-insulator (IMI) stack. Since my work explores the MIM geometry for sensing, I will describe this geometry in more detail below.

The field distribution and dispersion relation for the TM0 mode supported by MIM stack may be calculated in a similar way as for the single metal-insulator interface. These analytical results guide

experiments and computational models in the rest of this thesis. The MIM slab waveguide and its field distributions may be expressed analytically by summing the field contributions from surface plasmons at the two opposite metal interfaces. Enforcing continuity of E_x and H_y yields the exact dispersion relation [3], [10]–[12]:

$$\tanh(k_i t_i) = -\frac{k_m \epsilon_i}{k_i \epsilon_m} \tag{2.18}$$

Where t_i is the thickness of the insulator with permittivity ε_i in between semi-infinite metal slabs with permittivity ε_m. The wave vector components k_m, k_i, correspond to the metal and insulator respectively and are defined by equation (2.16) which includes the propagation constant β .

The MIM dispersion relation has a number of approximate expressions [10], [12], [13] which clarify the role of each parameter and are readily solved analytically. As I am primarily concerned with small gaps $t_i \lambda_0 \ll 1$, the small angle approximation can be applied to the tangent function to yield a simplified dispersion relation [12]:

$$n_{eff} = \frac{\beta}{k_0} = \sqrt{\epsilon_i}\left(1 + \frac{\lambda_0}{\pi t_i \sqrt{-\epsilon_m}} \sqrt{1 + \frac{\epsilon_i}{-\epsilon_m}}\right)^{\frac{1}{2}} \tag{2.19}$$

The key trends are now clear: the effective index of the MIM stack increases by either increasing the dielectric permittivity or by decreasing the width of the dielectric layer. MIM stacks can be realized experimentally using sputtering [14] with high accuracy, so the above dispersion relation can be verified experimentally [15].

The MIM dispersion relation for the TM0 mode is plotted in Figure 2.6a, along with the H field in the stack. Starting with 100 nm insulator thickness and refractive index 1.45, the MIM dispersion relation appears similar to the SPP dispersion. Decreasing the insulator thickness brings the SPPs at the two metal interfaces closer together, which increases their coupling [12]. The field plot in figure 2.6b also resembles two SPPs coupling across the gap as they propagate at either metal interface. As with the SPP calculation, in this calculation both metal slabs extend infinitely in the vertical direction. In contrast to the SPP case, the light is unable to extend arbitrarily into the insulator but is instead confined by the other metal layer. In fact, the dispersion relation indicates no “cutoff” thickness at which the resonance would no longer be supported, which enables light confinement even in Ångström-scale gaps [16].

Thin gaps cause the light to propagate more slowly, evidenced by the increasing effective index observed for thinner insulator layers in figure 2.6c. This reduced speed of propagation may be explained by considering power flow or by total internal reflection. The power flows in anti-parallel directions in the metal and the insulator [13] [17], resulting in a net slowing of the light propagation in the stack. When light totally internally reflects, it experiences a (small) displacement at the reflection interface, known as a Goos-Hänchen shift. This displacement is, in fact, negative at insulator-metal interfaces for p polarisation [18]. These negative displacements effectively slow the light down with each reflection.

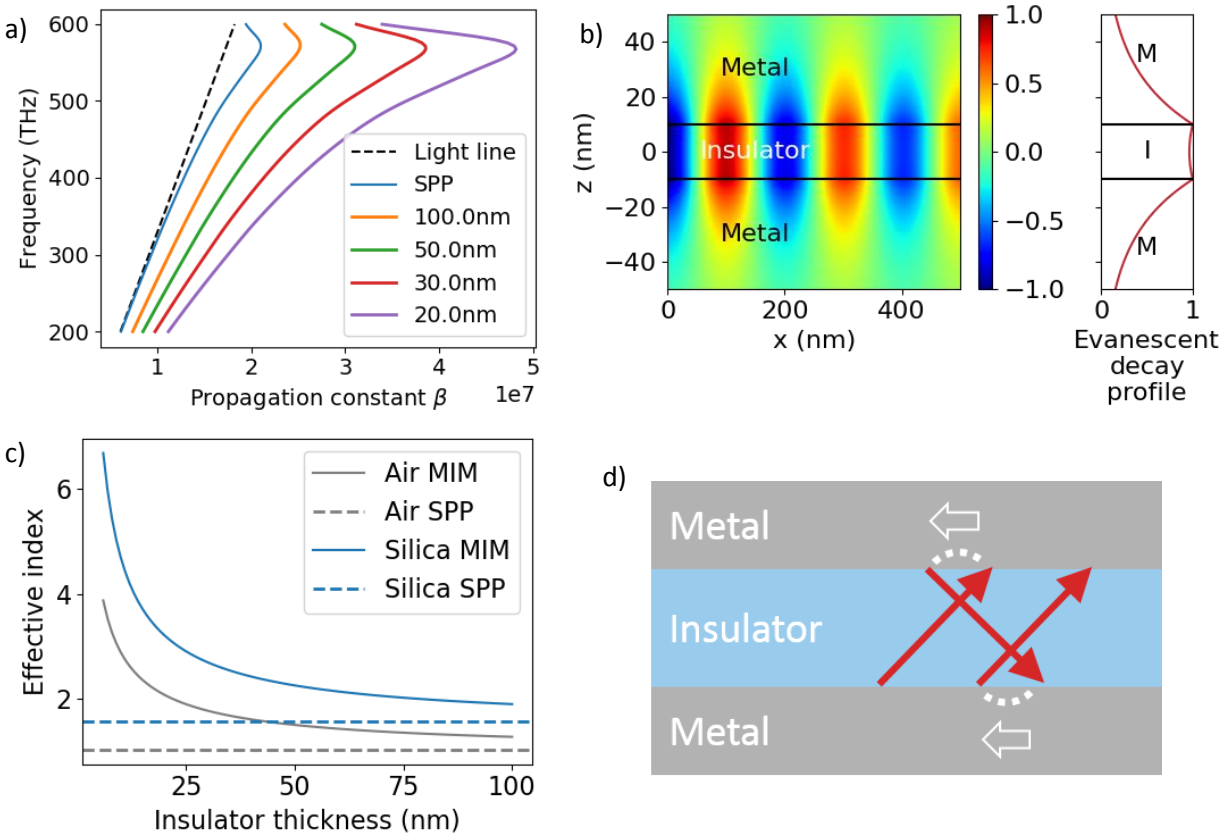

Figure 2.6. Properties of a gold-silica-gold MIM stack. a) dispersion relation for the MIM resonance with insulator thicknesses as the parameter. b) H field plot for a MIM stack with 20 nm insulator and decay profile into the metal cladding. c) Refractive index as a function of thickness for both air and silica MIM stacks. d) Schematic of light propagation in a MIM stack where the hollow white arrows indicate negative energy flow and negative Goos-Hänchen shifts for the red forward-propagating rays.

2.4 MIM cavities

The MIM waveguide confines light in sub-10nm gaps between the metal half-spaces. The spatial extent of these metal half-spaces can also be reduced to define small mode volumes where mode volume V_{eff} is a measure of the spatial confinement of the electric field and is defined mathematically as [19]

$$V_{eff} = \frac{\int \epsilon(\boldsymbol{r})|\boldsymbol{E}(\boldsymbol{r})|^2 d^3\boldsymbol{r}}{Max[\epsilon(\boldsymbol{r})|\boldsymbol{E}(\boldsymbol{r})|^2]} \tag{2.20}$$

Where ε(**r**) is the material permittivity and **E(r)** is the electric field at a point in space **r.** The integral is performed over the volume in and around the resonator to include the evanescent field. This section outlines strategies for such plasmonic confinement with an overview of techniques found in the literature and concludes with a number of areas in which these cavities have been applied.

Two metal nanoparticles are brought close (~10nm) together, forming a dimer system and a ~10nm gap in which the light is confined. A similar system involves a dipole and a mirror underneath that dipole. The metal mirror creates an image of the dipole because the plasmons on the top metal couple with the charges in the metal mirror below by the image charge method shown schematically in figure 2.7a, b [20]. The image charge method requires that the field lines of the total field crossing the metal-insulator interface must be normal to that interface. This boundary condition has consequences for the direction in which the dipoles are mirrored. A dipole perpendicular to the

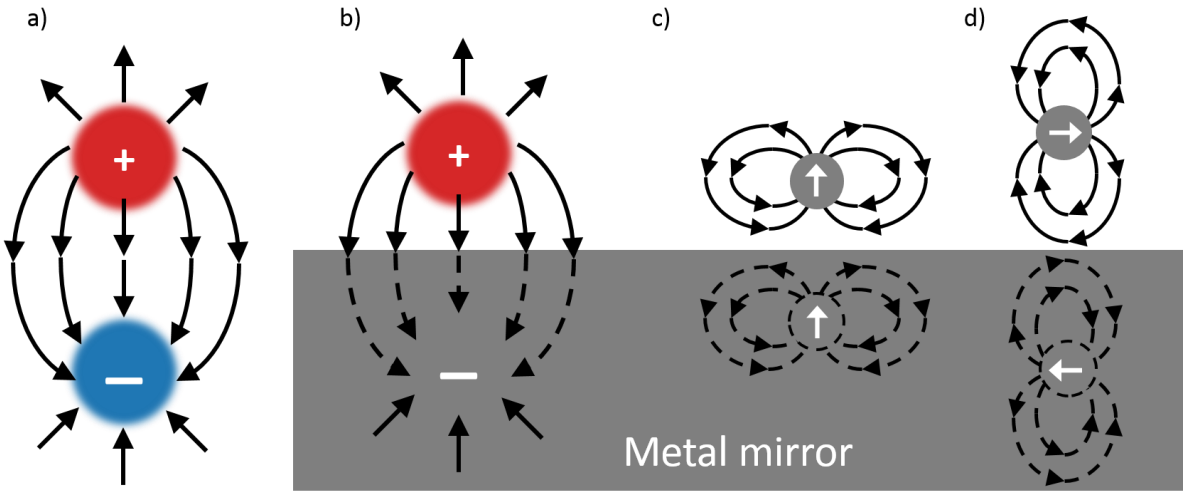

Figure 2.7. Schematic of electric fields for dipoles. a) Positive and negative charge forming a dipole. b) Positive charge creating the image of a negative charge in a metal mirror. c) A vertically aligned dipole creating an image of a dipole aligned parallel in a metal mirror and d) a dipole aligned horizontally with the metal mirror creating the image of an anti-parallel dipole in the metal mirror.

interface has its direction preserved, e.g. if the dipole is pointing from the metal to the insulator then the image of the dipole in the metal will be pointing in the same direction (figure 2.7c). However, dipoles pointing parallel to the gap is not preserved but inverted (figure 2.7d) [21].

2.4.1 Fabrication techniques

A number of top-down methods have been employed to bring two metal features close together to achieve high confinement. Fine control over position may be achieved by using an AFM and gold coated probes, forming a single cavity with a tunable gap thickness [22]. Multiple cavities may be fabricated on the same substrate with electron-beam lithography. Patterns of two closely-spaced metal features may be defined to form gaps as narrow as 3nm, for example “bow-tie” antennas [23], [24]. While these top-down methods have been used with success, the defects and surface roughness of the features are hard to control and are detrimental to the plasmonic resonance.

Bottom-up methods offer smoother metal surfaces due to finer control of defects and grain boundaries. Nanoparticles may be assembled into dimers, between which there is a thin insulator gap. The nanoparticles are tethered together by DNA [25], [26], a combination of hydrophobic and hydrophilic “brushes” [27] or alkane thiols [28]. Using chemical methods to determine the gap size offers much higher precision as the length of these linker molecules can be controlled at sub-nm level. Selecting the number of nanoparticles by purification typically involves encapsulating the nanoparticle clusters in a gel (gel electrophoresis) [29], [30] which makes the resonant mode spatially inaccessible for refractive index sensing.

Isolated MIM cavities with precisely controlled gap thickness and accessible evanescent fields may be realized by utilizing a metal mirror as the substrate. In other words, only one of the half-spaces in section 2.3.2 requires spatial truncation in order to realize a MIM cavity. The insulator creates a gap between the particle and its image and may be deposited by sputtering [11] (used for this work) or other methods such as DNA origami [31], polyelectrolytes [32] or alkane-thiol self-assembled monolayers down to a thickness of 0.5nm [33]. The discrete metal feature atop the layered substrate may also be realized in a number of ways, depending on the length scale. Micron-scale features can be defined with photo-lithography [34], nanoimprint lithography and electron beam lithography to make features on a ~100nm length scale [35], [36]; even smaller features may be realized by placing nanoparticles on the substrate [33]. Nanoparticles may even be arranged in regular arrays on the substrate [37].

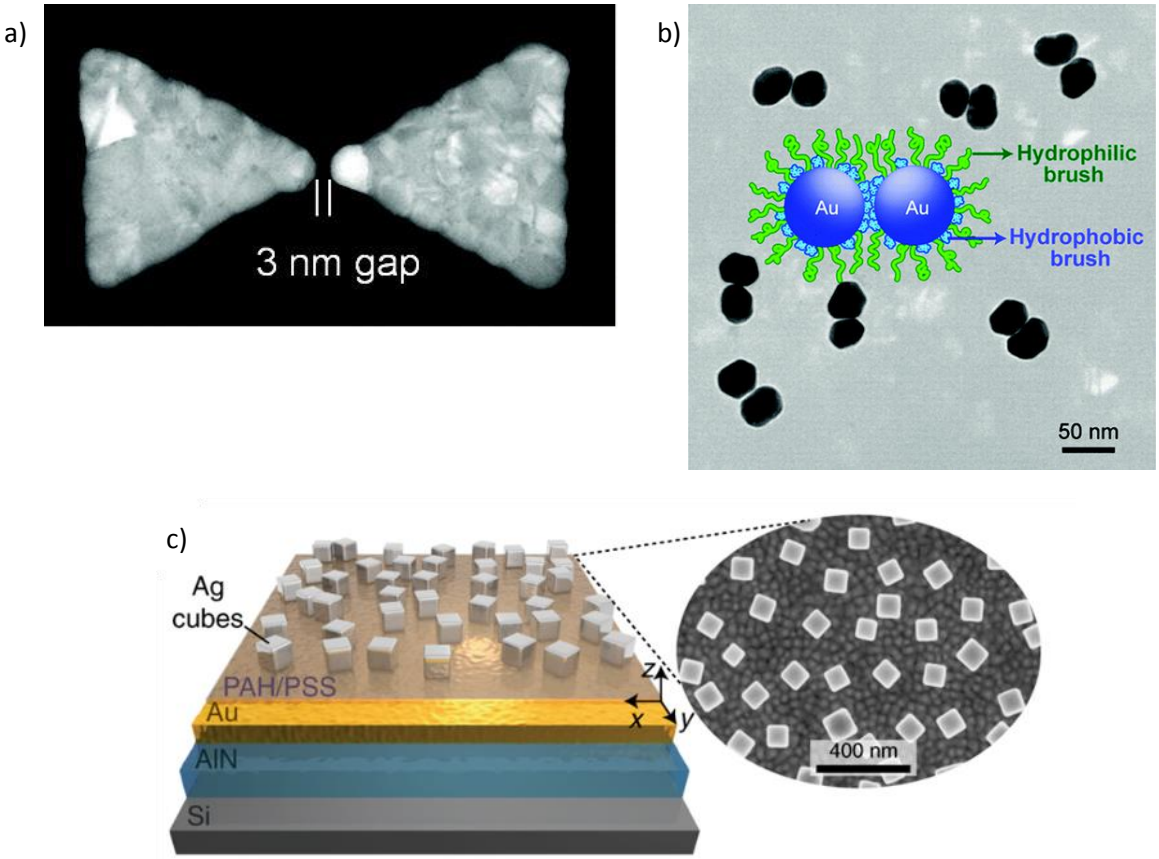

Figure 2.8. MIM cavity fabrication strategies in the literature. a) Defining two closely spaced features using electron-beam lithography reprinted from [23]*, b) Nanoparticle dumbbells by attaching two nanoparticles with linker molecules reprinted from ref* [27] *and c) depositing nanoparticles on a layered substrate reprinted from ref* [153]*.*

2.4.2 Applications

The resonances supported by this nanoparticle-on-mirror geometry have been investigated in the literature. A Fabry Perot model succeeds at describing the resonator wavelength as a function of the metal feature width and its effective refractive index [11], [38]:

$$2n_{eff}L_{cav} = \left(m - \frac{\phi_r}{\pi}\right)\lambda_{\mathrm{res}} \tag{2.21}$$

where λ_{res} is the resonance wavelength, n_{eff} is the effective index of the MIM stack, L_{cav} is the geometrical length of the discrete metal feature which forms the cavity, φ_r is the phase change upon reflection at the resonator edges and m is the mode order.

The nanoparticle-on-mirror geometry supports a plethora of resonant modes which are well understood in the literature. The 1-dimensional Fabry-Perot model has been extended to 2-dimensional circular nanopatches [39] and circular facets of spherical nanoparticles [16] by describing the radial symmetry with Bessel functions. Their radial symmetry allows the spherical nanoparticle-on-mirror resonant modes to be described with spherical harmonics [8]. The particles' edge rounding itself has been explored as a parameter to compare nanospheres and nanocubes [40] and affects the structures' sensing performance as I will show in chapters 4 and 6. The cube and sphere radiation profiles have also been compared [41], showing that the localised MIM resonances may be coupled to over a wide range of angles.

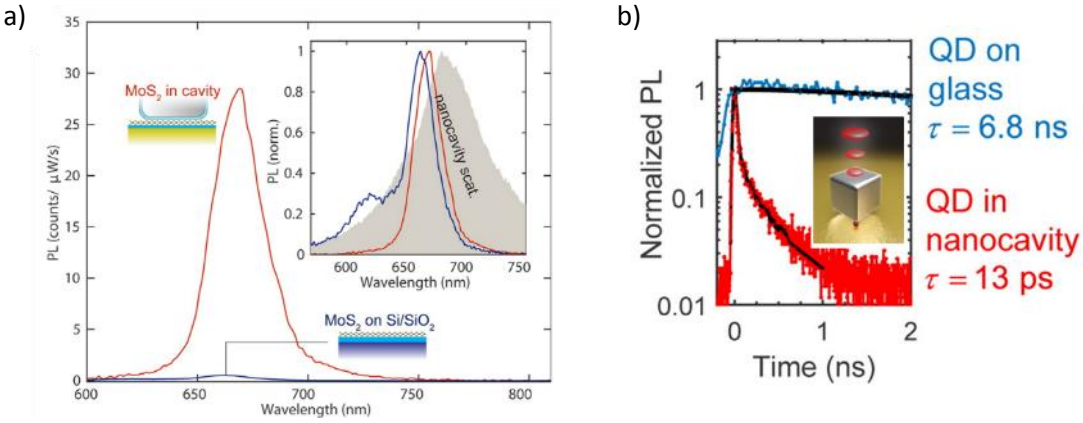

Figure 2.9. MIM cavities used to tailor emission processes. a) enhanced photoluminescence from 2D material in MIM cavity reprinted from ref [43]*. b) decreased photon lifetime for increasing emission rate of quantum dots in a MIM cavity reprinted from* [42]*.*

The electric field enhancement combined with the small mode volume makes the nanoparticle-on-mirror design particularly suited to enhancing light emission. Nanocubes on mirrors have been used to control radiative processes of fluorophores [41], to increase the emission rate of quantum dots

[42], to enhance photoluminescence [43] and to tune the emission and wavelength [44] of 2D materials. Spherical nanoparticles on metal-insulator substrates have suppressed plasmonic quenching [45] and enabled room-temperature strong-coupling to dye molecules [46].

Use cases for the MIM are not limited to coupling to emitters. The electric field confinement may also be used to enhance third harmonic generation in non-linear optical media [47] and probe molecule orientation via SERS [48], [49]. The MIM structures themselves may be used as thermal emitters in the mid-IR [34], [50]. As well as generating light, MIMs can change the quality of incident light by reshaping phase fronts [51],removing wavelengths from the incident spectrum by acting as (electrically tunable) colour filters [52], [53] and controlling Förster resonance energy transfer [54].

MIM structures have also been used for bulk refractive index sensing [35], [55]. The key to the MIM's performance as a refractive index sensor, its surface sensitivity, is hitherto unexplored. The following section describes existing refractive index sensing methods and concludes by comparing the MIM resonance to these established techniques.

2.5 Refractive index sensing

Label-free resonant refractive index sensing detects specific molecules on sensor surfaces. Each different use case requires detecting a different and specific (bio)molecule. Specificity is achieved by functionalizing the resonator surface with capture molecules by using surface chemistry protocols [56]. Developing and optimizing these protocols can be a very time consuming and remains a drawback to label-free resonant refractive index bio sensing [9]. The focus of this work is to develop a method for measuring refractive index changes on the length scale of these functionalised layers, in order to use them to detect ever smaller concentrations. The following section provides context for the research by describing previous strategies employed to probe these reactions on a resonator surface.

2.5.1 Refractive index sensing principles

The evanescent fields may be approximated by a decaying exponential profile [3], [57], [58] which overlaps with binding sites on the sensor surface. Molecular binding then contributes to the effective refractive index experienced by the resonant mode, which in turn changes its resonant frequency [59]. A high performance resonant refractive index sensor therefore probes changes in its surrounding environment below $1x10^{-4}$ refractive index units (RIU), ideally on the length scale of the molecules; a good quantification of a resonator's performance therefore includes a measure of its sensitivity on a molecular length scale, usually referred to as the surface sensitivity.

In contrast, the metric that is usually quoted is the response to refractive index changes in the bulk of the analyte, the sensor's "bulk" sensitivity [35], [60], [61]. The bulk sensitivity is easy to measure and serves as a starting point for further investigations [62]. However, many authors then implicitly assume that the bulk sensitivity is proportional to the surface sensitivity; for example, Homola et al. [63] state that "This suggests that the surface refractive index sensitivity is proportional to the bulk refractive index sensitivity…". This extrapolation does not generally hold and bulk sensitivity gives an incomplete description of a resonant refractive index sensor's performance [59].

A number of authors define detection zones close to the sensor to assess surface sensitivity with thicknesses of 25nm [59], 8 nm [64] or 5nm [65] which are in reasonable agreement with the ~10nm size of an antibody [56], [66]. Despite the thickness variety of these defined detection zones, the length scale is clear: binding events take place within nanometres of the resonator surface. Binding events within the detection zone V_d cause changes in permittivity $\Delta\varepsilon$. These changes in permittivity

perturb the normalised resonant electric field $\tilde{\mathbf{E}}$, where $\tilde{\mathbf{E}}_p$ is the perturbed electric field The resonant frequency changes $\Delta\tilde{\omega}$ for a permittivity change $\Delta\varepsilon$ is proportional to the resonant frequency $\tilde{\omega}$, the overlap between the normalised (denoted by the tilde) electric field $\tilde{\mathbf{E}}$, the perturbed electric field $\tilde{\mathbf{E}}_p$ in the detection zone V_d for photonic [59] and plasmonic [65] sensors and can be described as follows:

$$\frac{\Delta\tilde{\omega}}{\Delta\epsilon} = -\tilde{\omega}\iiint_{V_d} \tilde{\boldsymbol{E}}_p(\boldsymbol{r}) \cdot \tilde{\boldsymbol{E}}\,(\boldsymbol{r}) d^3\boldsymbol{r}. \tag{2.22}$$

The mode overlap with the detection zone may be estimated using the evanescent decay length from a generic resonant structure. The SPP evanescent decay lengths in section 2.3.1 encourage a back-of-the-envelope calculation with equation (2.22). The SPP resonance wavelength is 650nm and the decay lengths into the insulator and metal are 450nm and 23nm respectively. I coarsely approximate that 450/ (450+23) = 95% of the electric field overlaps with the bulk analyte above the metal film, where the detection zone extends from the metal-insulator interface to infinity. Therefore, the evaluated integral value may be approximated as 91%. This value of 91% corresponds to a change of 91% of the resonance frequency for one unit of permittivity.

This example may be extended by substituting refractive index values to get a feel for how sensitive we would expect an SPP to be to changes in its bulk surroundings in nm/RIU (nanometres per refractive index unit). I take 1.33 as an initial refractive index and 1.34 as increase to the bulk surroundings, corresponding to permittivity of 1.77 and 1.79, the difference between which is 0.02. The resonance frequency corresponding to a free space wavelength of 650nm is $4.6\text{x}10^{14}$ Hz. The new frequency is calculated by applying equation (2.22) and subtracting the calculated frequency difference: $4.6\text{x}10^{14}$ x (1-0.02 x 0.91) = $4.50\text{x}10^{14}$ Hz. This change in frequency corresponds to a change of 16nm in wavelength. Dividing the wavelength shift by the difference in refractive index units 0.01RIU yields a bulk sensitivity of $1.6\text{x}10^3$ nm/RIU. SPP experiments reported in the literature typically have ~10^3 bulk sensitivity [63], [67] which confirms the rough calculation described here.

A generic refractive index sensor may be modelled as a waveguide with decay length L_d which is the distance from the resonator at which the electric field has decayed to 1/e of its value at the resonator surface, where e is Euler's number (e=2.718) [3], [57]–[59]

$$\frac{1}{L_d} = \frac{1}{\lambda_{res}}\sqrt{n_{eff}^2 - n_c^2}, \tag{2.23}$$

determined by the resonance wavelength, λ_{res} effective index of the waveguide n_{eff} and refractive index of the cover medium n_c. Ideally, the decay length will be similar in size to the detection zone in order to suppress background effects in the detection volume [68].

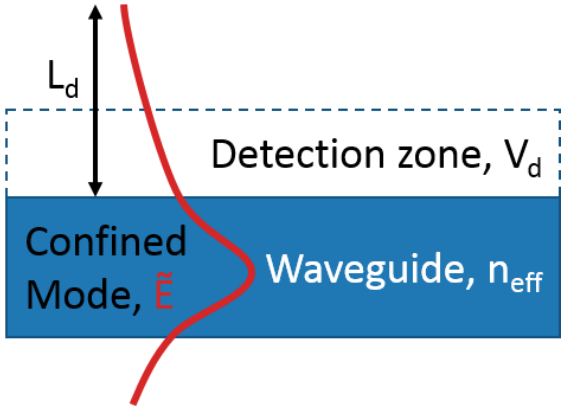

Figure 2.10. Schematic of mode overlap with a generic resonator indicating overlap with detection zone.

While the bulk and surface sensitivity of a resonator are important quantities for refractive index sensor performance, there are other quantities which need to be considered. The ideal refractive index sensing setup will make the most of its high sensitivity by also resolving very small (<0.1nm) changes in wavelength. These small changes in wavelength are more easily resolved when tracking sharper peaks with higher quality (Q) factors [58]. The Q factor describes the time for which light is confined. The definition of Q factor is given in the equation below:

$$Q = 2\pi \frac{Energy\ stored}{Energy\ dissipated\ per\ cycle} \approx \frac{\Delta\lambda}{\lambda} \tag{2.24}$$

This equation also shows that the Q factor may be calculated from the full-width at half-maximum of the cavity, where λ is the resonant wavelength of the cavity and Δλ is the full-width at half-maximum of the cavity. Thus Q factor is an important parameter to quantify cavity performance because it relates to both the time for which light is confined and the width of the resonance peak.

The Q factor and bulk sensitivity S_λ are therefore combined to calculate the figure of merit (FoM) for a particular structure [62], [69], [70]**:**

$$FoM = S_\lambda \times Q \tag{2.25}$$

This figure of merit above is independent of the readout method which allows resonators to be compared directly. The readout method does, however, profoundly affect the limit of detection (LoD) [71] defined as follows

$$LoD = \frac{3\sigma}{S}, \tag{2.26}$$

The readout method impacts on the noise floor, for example the resonance wavelength and associated fluctuations prior to any binding event [58], which determines the standard deviation σ used to calculate the limit of detection. I write a general sensitivity term S because it should be noted that limit of detection is not limited to peak wavelength-based readouts with wavelength sensitivity S_λ but may be applied to any readout e.g. a phase- or intensity-based readout method. The intrinsic properties of the resonant structure such as its sensitivity and Q factor will be discussed first, followed by a comparison of readout techniques and their effect on a system's limit of detection.

2.5.2 Plasmonic refractive index sensing structures

A large range of optical resonators has been discussed in the literature, many of which have been applied to refractive index sensing [9], [58], [72]. Here, I review the key differences between these sensors to illustrate the relative strengths and weaknesses of the different strategies.

An example of a sensor that supports a resonant mode with a particularly long evanescent tail is a surface plasmon polariton. Recall that the SPP described in the preceding plasmonics section extends 450nm into the analyte. Such a long evanescent tail leads to a large overlap with the analyte and causes relatively high 2500nm/RIU bulk sensitivity [63], [67] where RIU stands for refractive index unit. The SPP also demonstrates 150nm/RIU surface sensitivity for a 10nm layer in a COMSOL simulation. These high sensitivities, combined with the simple prism/Kretchmann coupling configuration led Biacore to commercialise SPR sensing [1]. Biacore systems have been applied to studying biomarkers [73], drug discovery [74], food quality and environmental monitoring [63].

Despite its high sensitivity and numerous applications, the SPR system has limitations from both its practical implementation and its resonant characteristics. The prism required to couple to the metal film is bulky and limits the Kretschmann configuration to a benchtop configuration. Furthermore, the SPPs themselves have a short propagation length due to their intrinsic loss: they only propagate 10-100µm, which limits the minimum sensing area of interest [9] and Q factor to ~20 [73]. Combining this relatively low Q factor with the relatively high bulk sensitivity leads to a ~10^4 SxQ figure of merit. This figure of merit will serve as a benchmark for the following resonant structures to be discussed.

SPR coupling requirements can be relaxed by localizing the resonant mode which creates a larger space of k-vectors at which incident light may couple to the mode. One strategy to define these into localized surface plasmon resonances (LSPR) is patterning a metallic layer. Localizing or more tightly

confining the resonant mode reduces bulk sensitivity, increases the Q factor and allows coupling to the mode directly without the use of a grating or prism. For example, a metal layer patterned with nanoholes has a 700nm/RIU bulk sensitivity and Q factor of 40 [75], [64] which results in a $2.6x10^4$ figure of merit, which is comparable to SPR. In light of this relatively high figure of merit, these patterned metal layers remain a competitive sensing strategy. Their surface sensitivity has been demonstrated as 31nm/RIU for an 8nm layer [64] with the ability to detect 3nm protein layers [76]. More complex structures with higher figures of merit ($\sim10^6$) do exist but at the expense of more stringent angular dependent coupling requirements [69]**.**

Another strategy to confine plasmon resonances is to use nanoparticles. Gold nanoparticles may either be purchased or synthesized in a variety of shapes; they typically have bulk sensitivity of 100-500nm/RIU and Q factors of the order 10 [61]. Gold nanoparticles have a $\sim2.5x10^3$ figure of merit, lower than the previous two plasmonic techniques but they compensate for this low figure of merit with their commercial availability and ease of use. Isolated gold nanodisks on a substrate have a surface sensitivity of approximately 50nm/RIU for a 10nm layer [77], comparable to the gold nanoholes mentioned above. LSPR in gold nanoparticles has been commercialised by LamdaGen for point-of-care testing devices [78] and wearable technology [79].

A natural extension of using these nanoparticles for sensing is to place them on a layered substrate forming a MIM resonator. MIM resonators fabricated by top-down methods [35],[55] and bottom-up methods [32] have indeed been demonstrated 400nm/RIU and 560nm/RIU bulk sensitivities respectively. However, the MIM surface sensitivity and its ability to detect the presence of molecules on its surface remains unexplored.

2.5.3 Dielectric resonant refractive index sensing

This overview of sensing strategies would be incomplete without mentioning dielectric resonant sensing structures. The advantage of dielectric sensing structures is that they allow smaller peak wavelength shifts to be resolved than plasmonic structures do because dielectric resonators have intrinsically sharper resonances due to the absence of absorbing media in the resonator. An example photonic sensing structure with a high Q factor is a photonic crystal cavity [80]. Photonic crystal cavities have a relatively low 60nm/RIU sensitivity due to most of the light being confined within the dielectric material and having less overlap with the analyte compared to plasmonic structures. However, high Q factor of ~10,000 [81] allows smaller peak wavelengths to be resolved which is

represented in the $6x10^5$ figure of merit. This figure of merit is, in fact, higher than the SPR benchmark.

1D [82] and 2D [83] guided mode resonance (GMR) gratings have also been used for sensing. Their comparison to SPR is similar to the photonic crystal cavity case: the higher Q factors compensate for the lower sensitivity values. A typical guided mode resonance grating has an evanescent tail length of 350nm, ~300nm/RIU bulk sensitivity [82], [84] and 20nm/RIU or 47nm/RIU surface sensitivity for 10nm [85] or 25nm [59] thick detection zones respectively. The reduced bulk sensitivity is compensated by their relatively high ~200 Q factors [82] [85] [83] resulting in typical $5x10^4$ figures of merit, remaining competitive with SPR performance.

2.5.4 Readout methods

So far, the readout method for these resonant refractive index sensors has been discussed in terms of their peak wavelength shifts. In order to measure the peak wavelength value and any peak wavelength shift, a spectrometer is required. In general, readout methods are not limited to using a spectrometer and there are a variety of other methods to extract a relative peak shift from these resonant sensors. Dispensing with the spectrometer for an intensity-based readout may therefore be advantageous for reducing the cost of the readout assembly. For example, probing the resonance condition of gold nanoholes with an LED and CCD has been demonstrated with a limit of detection as low as $4x10^{-3}$ RIU [76]. Similarly, monitoring the resonance position of a single dielectric structure with an LED and a photodiode has been shown to achieve a limits of detection as low as $2x10^{-4}$ [86]. The imaging capabilities of the CCD also may be used to measure multiple structures simultaneously, either as an experimental control or to detect for multiple molecules in parallel [68], [87]. While this technique measures competitive limits of detection, it is highly susceptible to noise from fluctuations in source intensity.

Intensity variations in the source can be negated by comparing the relative strengths of multiple points within a source's bandwidth, as the spectrometer does. A key innovation in this regard has been to create an "on-chip spectrometer" by placing multiple structures with different resonance conditions on the same chip and simultaneously measuring their reflected or transmitted intensities using a CCD. This strategy has been realised by using "pixels" of different resonance conditions [88], [89] or by continuously chirping a guided mode resonance grating resulting in a limit of detection as low as detection $2.4x10^{-4}$ RIU [90]. Probing multiple intensities simultaneously allows sophisticated post-processing to be used, achieving limits of detection as low as $7x10^{-5}$ RIU [91]. Designing multiple

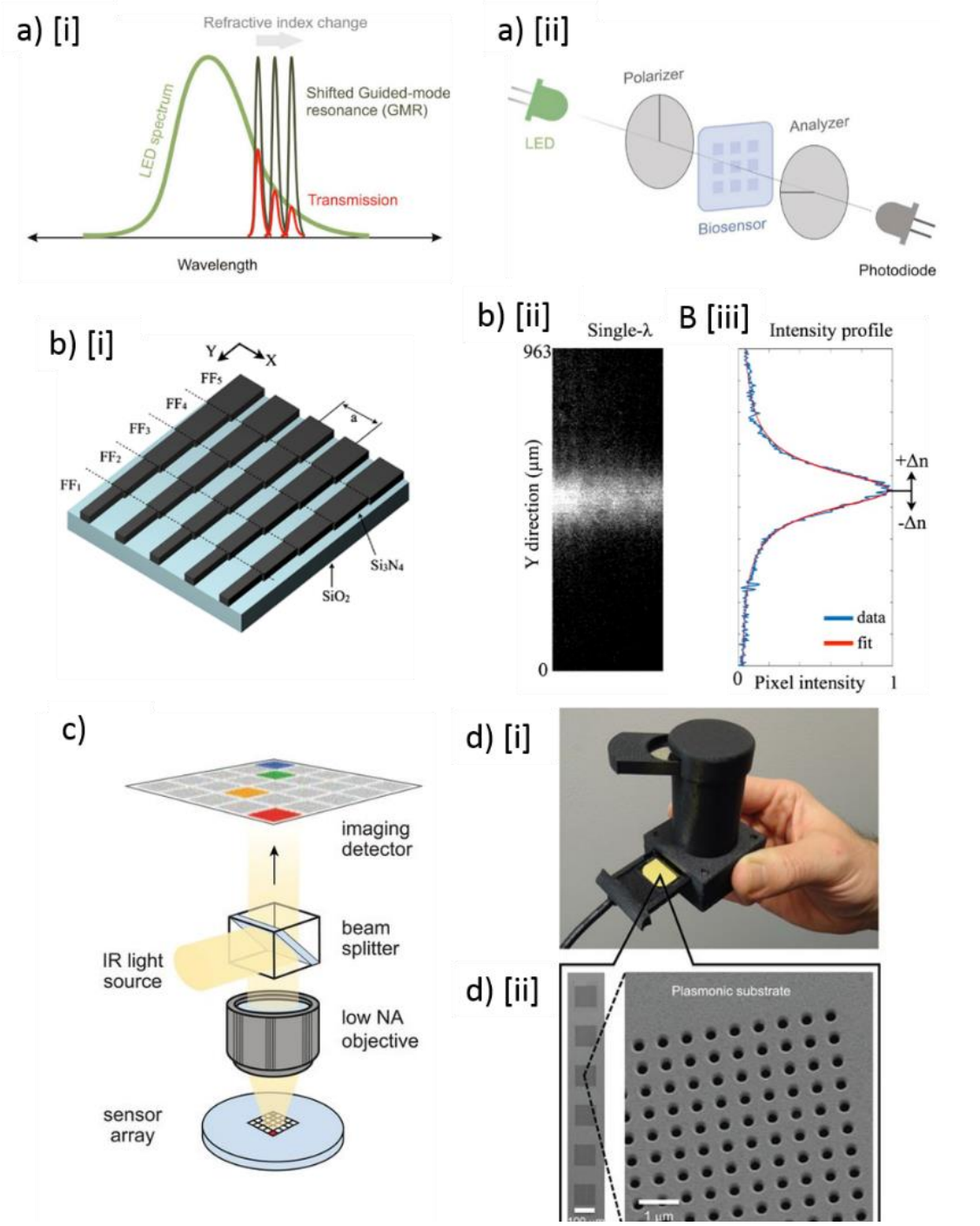

Figure 2.11. Resonant refractive index sensor readout methods. a) Intensity-based readout from a guided-mode-resonance (GMR) biosensor showing: i) the device spectra and peak wavelength shifts, and ii) the low cost equipment required for implementation. b) The chirped GMR biosensor: i) a schematic of the chirped grating structure and b) the device spectrum recorded as an intensity profile with a CCD. c) "Pixels" of dielectric structures with different resonance conditions to record a spectrum with a CCD. d) Realisation of a handheld assembly i) to monitor the peak wavelength shift of ii) a gold nanohole array. Figures a) reprinted from [86]*, b) reprinted from* [90]*, c) reprinted from* [88] *and d) reprinted from* [76]

resonance conditions on the same chip is better suited to the spatial control offered by top-down fabrication methods. Regardless, there are key insights offered by this technique, chiefly: probing more than one point of a source or a resonance results in a lower limit of detection.

2.6 MIM suitability as a sensing structure

This chapter has outlined the core principles of plasmonics, MIM resonators and refractive index sensing. The MIM structure has already been used for bulk refractive index sensing, but the description of its performance regarding surface sensitivity and sensitivity to molecule-scale interactions remains incomplete. In the context of these sensing principles and previous work on MIM resonators, should one expect a MIM resonator to be a competitive, high surface sensitivity refractive index sensing solution?

A competitive, high surface sensitivity refractive index sensor will have an evanescent field with high amplitude and tight confinement to the resonator surface. MIM waveguides are known to maximise the electric field at their entrance with a short (~10nm) evanescent tail [11]. These evanescent field characteristics provide the origin of the MIM's high surface sensitivity and will be described in more detail in chapters 4 and 6.

Elegant readout methods have the potential to reduce the cost and dimensions of refractive index sensing systems by using simple, low cost components such as LEDs, photodiodes and CCDs. These solutions are easier to implement when there are fewer constraints to couple to a resonance. The odd-numbered MIM resonant modes are not sensitive to angle (from ref [53] "the nanoparticles strongly confine light within their individual gaps to the underlying mirror and thus produce extremely localized cavity resonances, making them independent and insensitive to the angle and polarization of the incident light") however it should be noted that this is not true in general; even-numbered modes require coupling at an angle in order to be excited [35]. Furthermore, areas of MIM resonators may be fabricated on a cm^2 area scale [53]. The large area, angle-insensitive resonators allow for a simple, low cost readout method to be demonstrated, which is described in chapter 7.

Chapter 3

Methods

I used a number of methods to simulate, fabricate and characterise the two types of MIM structure presented in this work. A schematic of the targeted structure is shown in figure 3.1. The insulator thickness t_i is of the order 10nm, the feature width w is of the order 100nm and the metal thickness t_m is of the order 10nm. The exact dimensions of a particular MIM structure vary, and are stated in the relevant section.

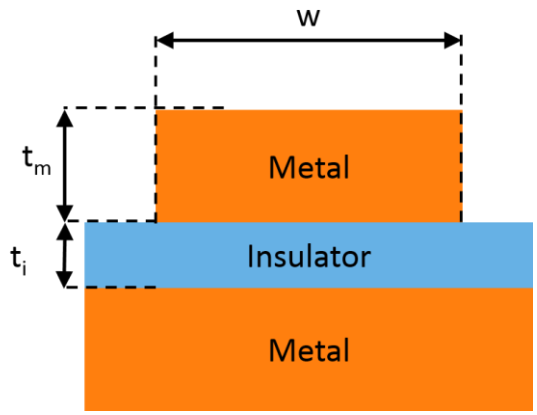

Figure 3.1 Schematic of MIM structure with key dimensions: Feature width w: ~100nm, feature thickness t_m: ~100nm and insulator thickness t_i: ~10nm

First of all, I outline, compare and contrast the two simulation techniques in section 3.1 that are used in chapters 4 and 6. I describe the deposition processes common to fabricating both types of device (sections 3.2 and 3.3), and conclude with characterisation techniques applied to both devices (3.4, 3.5). The patterning techniques specific to each device are presented in their separate chapters.

3.1 Simulation techniques

Simulation techniques offer a relatively fast way to narrow parameter sweeps compared to fabrication. These calculations also provide electromagnetic field information to model a structure's sensing performance. Two simulation tools were used to design and mode the sensing performance of MIM structures: rigorous coupled-wave analysis (RCWA) and COMSOL Multiphysics. Both simulation tools discretize Maxwell's equations but each tool applies a different method to perform this discretisation, discussed below.

3.1.1 Rigorous coupled-wave analysis

Maxwell's equations require discretisation in both space and time in order to be solved computationally. Time is discretised by defining the electric field at discrete frequencies, the same as for the analytical models in (ref theory section). Maxwell's equations are discretised in *space* by applying a similar strategy: a periodic permittivity distribution is decomposed into its constituent *spatial* frequencies. This time-harmonic spatial-frequency form of Maxwell's equations is implemented in rigorous coupled-wave analysis (RCWA) [92] and is available in a number of computer programs [93], [94].

For example, a simple permittivity distribution ε(x) of a layer periodic in x and homogeneous in y, z can be expressed as a Fourier series:

$$\epsilon(x) = \sum_{n=-N}^{N} \epsilon_n \mathrm{e}^{iGnx} \tag{3.1}$$

where ε_n are the Fourier expansion coefficients, $G = \frac{2\pi}{a}$ is the Bloch wavenumber and a is the period of the structure. The Fourier series discretisation in equation (3.1) defines a unit cell with periodic boundary conditions. The expression in equation (3.1) also includes the finite number of terms N to which the Fourier series is truncated and which determines the accuracy of the RCWA method.

More complex structures are defined by stacking layers with the same period on top of each other (z direction). Each layer is represented by its own Fourier series, which is invariant along the z axis. These individual layers are connected to one another by defining boundary conditions between them. The condition between layers is to enforce continuity of the tangential E and H field components. The top and bottom layers of the stack are defined as semi-infinite half-spaces into which the reflected and transmitted waves propagate.

RCWA calculates reflection and transmission coefficients from electric field coefficients. These electric field coefficients describe a periodic electric field as a result of Bloch's theorem: Periodic permittivity distributions support periodic electric field distributions [95].

$$E = \sum_{n=-N}^{N} E_n \mathrm{e}^{i(k_x - nG)x} \tag{3.2}$$

Fundamentally, the electric field mode coefficients E_n are calculated by inserting the electric field expression (3.2) and permittivity distribution (3.1) into Maxwell's equations. In practice, inserting expressions (3.1), (3.2) into Maxwell's equations and solving the structure requires algebra beyond the scope of this description and may be found in peer-reviewed implementations of RCWA [93], [94].

I chose an RCWA method to run preliminary simulations of the MIM structure in 3 dimensions. The periodic boundary conditions model MIM resonators in a regular array, analogous to arranging them with a constant spacing on a substrate. RCWA methods have also been used to investigate MIM resonators in the literature [38]. I ran these simulations with the software package S^4 which is particularly attractive because it's easy-to-use, peer reviewed [94], and open source software.

Metals have high permittivity so require a high number of harmonics to resolve, even for 1D-periodic structures (specified in 2D geometry). 2D-periodic (specified in 3D geometry) RCWA simulations would require an even higher number of harmonics to converge, where the convergence parameter is the peak wavelength calculated by fitting a curve.. While 1D periodic RCWA simulations with metals converge at ~150 harmonics, 2D periodic RCWA simulations don't show convergence up to 300 harmonics, at which point there are more time-efficient 2D periodic simulation techniques available. Furthermore, RCWA offers a poor control of rounded corners in z due to the way it splits the structure in a layer-by-layer or "staircase" fashion. Alternative techniques offer a finer control over the corner geometry. RCWA was used to simulate 1D periodic gold/silica/gold MIM structures in sections 4.1-4.7

3.1.2 COMSOL software

COMSOL Multiphysics [96] offers a finer control over corners and a more scalable extension from 2D to 3D geometry than RCWA. COMSOL, like RCWA, solves Maxwell's equations in the frequency domain. The key difference between the RCWA and COMSOL models is how the refractive index distribution is discretized. COMSOL discretizes the refractive index distribution in space, in contrast to the Fourier- or k-space discretization used by S^4.

Comsol discretizes the geometry and permittivity by imposing a grid or “mesh” over the user-defined distribution. This mesh defines finite elements in space, for which the governing equations are evaluated. Defining this mesh requires careful attention; it’s important to define sufficient mesh elements to describe the physics over discrete points in space. The COMSOL documentation states that there should be at least 5 mesh elements along a wavelength in the medium in order to properly describe the electric and magnetic fields inside the geometry. Using fewer elements risks poor accuracy in calculated electromagnetic fields. Absorbing media such as metals have 5 elements per extinction coefficient [97]. These two meshing criterions would lead one to define mesh of the order of 20nm in and around metal features which is likely insufficient for plasmonic nanogap structures.

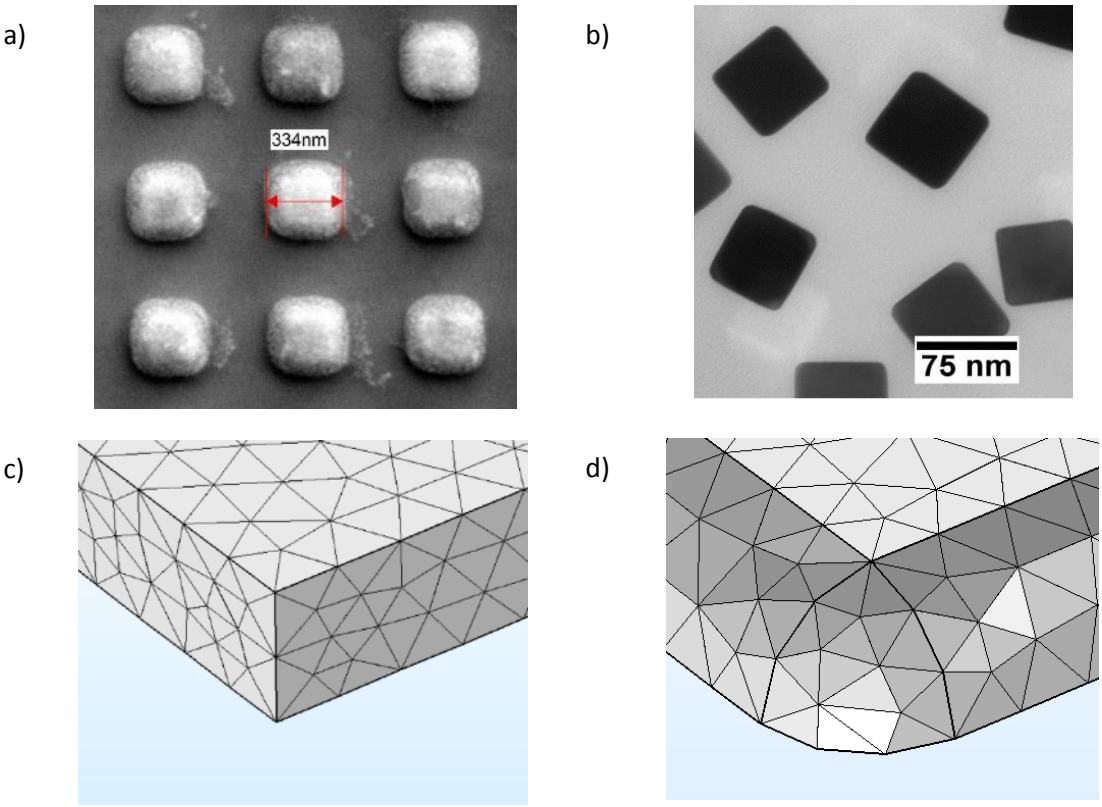

Figure 3.2. Example rounded corners in metal structures. a) SEM of lithographically fabricated gold squares b) TEM of silver nancubes. Example a) default and b) rounded corner geometries generated in COMSOL Multiphysics.

One may extract a third meshing criterion for plasmonic nanogap structures from previous works. R. Chikkarady states that a 1nm gap required a 0.3nm discretisation for convergence [98], and P. Lalanne provides an example of an 8nm gap requiring a 2nm mesh at the metal feature corners [7]. These previous works indicate that a plasmonic nanogap model should have at least 4 mesh elements per nanogap thickness. I defined mesh within this criterion for the lithographic and nanocube MIM

structures. I tested the mesh convergence by increasing the mesh resolution from 10nm to 5nm in the "gold only" model presented in section 4.9 and observed less than 0.3% variation in peak wavelength (1.9nm variation in 772.2nm) and less than 2% variation in surface sensitivity (1nm variation in 48.0nm/RIU, final result shown in figure 4.11) as a result.

Discretizing the structure in space provides the ability to "round" corners and edges, which more accurately represents real metal structures. Both structures in this work have rounded corners, particularly those fabricated by the lift-off process in chapter 5 and the nanocubes in chapter 7, both shown in figure 3.2. In COMSOL, the sharp corners are removed by applying a "fillet" function to round a corner. These rounded corners offer a closer match to the example real structures. In S^4, rounding corners is impossible; one would have to define a staircase of many steps instead of a corner, with each step having a sharp points at its corners- the very feature we're trying to avoid!

Despite its strengths, COMSOL has a number of limitations which are common to many simulation techniques. It is impossible to recreate all the fine details in fabricated structures, such as the topography which gives a surface "roughness". Furthermore, the large E field hotspots occurring in these MIM structures vary over a small (20nm) length scale, making them difficult to create in a discretised model without somewhat compromising accuracy. Therefore, the simulations presented in this work form a part, but not the entire description of a device's performance. They serve to guide fabrication and provide a context in which to discuss experimental results.

The calculations were typically performed on 16 dual-threaded central processing unit (CPU) cores with 64 GB of random access memory (RAM). The time taken to calculate one resonance peak consisting of 25 points took approximately 3 hours. The eigenmode approach in chapter 6, in which the resonance peak is calculated directly without a spectrum took less time to run. The software took approximately 30 minutes to determine a eigenmodes of a single resonant condition and calculate its electric and magnetic fields on resonance.

3.2 Deposition techniques

A MIM structure consists of three distinct layers, i.e. the bottom metal layer, the thin film insulator and the top metal layer. The construction of this sandwich requires additional adhesion layers and all layer thicknesses need to be precisely controlled since they affect the optical properties and operational features of the resulting devices. While these effects will be discussed in other chapters, I here outline the two deposition techniques used to realize MIM layers: sputtering and evaporation.

Sputtering was used to deposit silica layers and electron-beam evaporation was used to deposit gold layers. Titanium adhesion layers preceding sputtered silica were sputtered and titanium adhesion layers preceding evaporated gold were evaporated.

3.2.1 Pulsed DC magnetron sputtering

A well-established method of depositing thin metal and dielectric layers is sputter deposition. This section will explain what this technique entails and how it is performed on the bespoke sputterer available in the group, shown in figure 3.3a. I describe the deposition process and considerations for reactive sputtering and illustrate these with order-of-magnitude calculations. These sputter sections will conclude with a brief discussion of adhesion layers required to reliably fabricate these MIM structures.

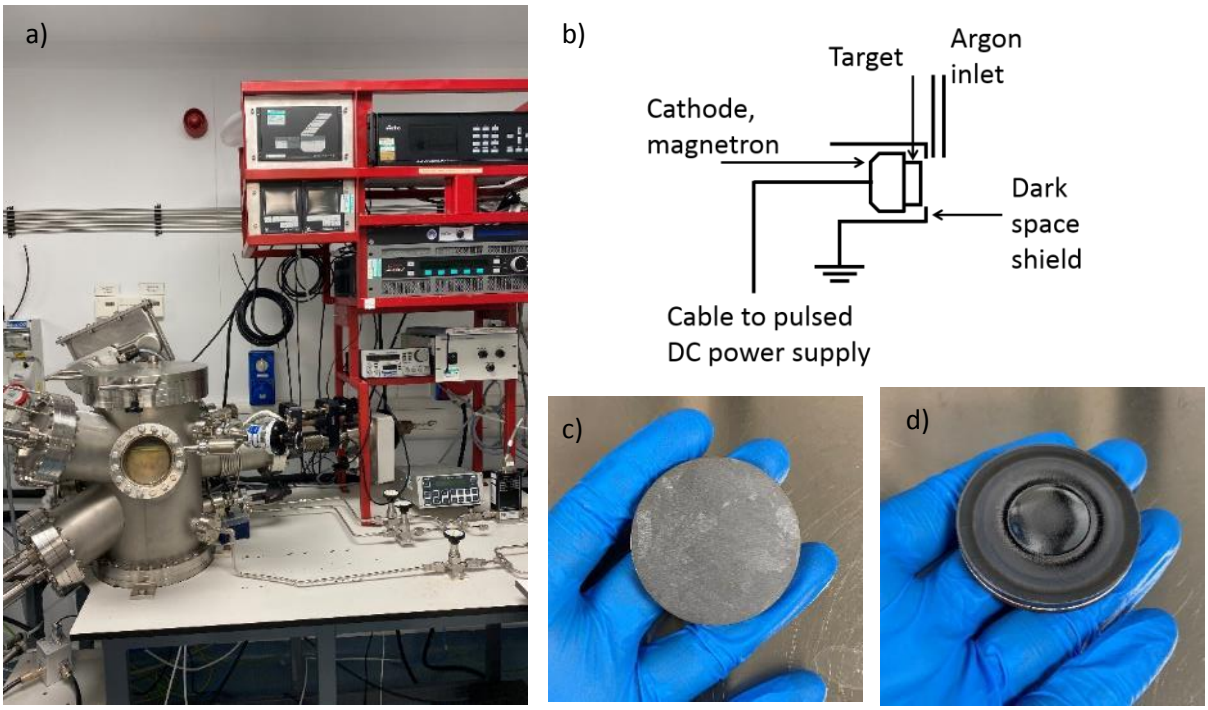

Figure 3.3. Bespoke pulsed DC magnetron sputterer available in the cleanroom at York a) Photograph and b) schematic of the sputterer showing one gun and its key components, c) and d) are examples of a silicon target before and after magnetron sputtering, showing the distinct "racetrack" erosion pattern.

Sputter deposition is a process whereby a plasma is generated and used to remove material from a target. The removed target material is projected across the chamber and lands on a substrate where it forms the desired thin film. The plasma is generated by injecting an inert gas such as argon, which is ionized by a high voltage and accelerated towards the target. The acceleration is due to the potential

difference between the sputterer target (connected to the pulsed DC power supply) and the grounded dark space shield. When these argon ions bombard the target, atoms from the target are removed and are projected across the chamber. These atoms land on the substrate, thereby depositing the target material.

3.2.2 Sputter deposition rate estimation

Calculating the removal rate of the target material by this process from first principles is non-trivial due the complexity of the energy-yield relationship between incident argon ions and removed target atoms. There are a number of semi-empirical models [99]–[101] which allow the rate to be calculated. Here, a rough calculation inspired by ref [102] is presented in order to illustrate and obtain order-of-magnitude numbers for the sputtering process. For example, the sputter power supply uses 0.31A and 322V, when sputtering titanium. Assuming, for simplicity, that the current is entirely due to argon ions impacting on the target, and that these argon ions are accelerated by the 322V potential difference allows us to produce the estimation. Dividing the 0.31A current by the $1.6\text{x}10^{-19}$ charge on an Ar^+ ion gives $1.9\text{x}10^{18}$ ions impacting the target per second. Tabulated values [101], [102] state the sputter removal yield of argon ions with 300eV energy impacting a titanium target is 0.3 titanium atoms per argon ion. Therefore, the $1.9\text{x}10^{18}$ argon ions impacting the target correspond to $5.7\text{x}10^{17}$ atoms removed from the target per second.

A rate of atoms removed, R_{atoms}, can be converted to a deposition rate onto a sample with the equation (3.3) below. The first term of the equation approximates the sputter target as a point source and models the ejection of material as following the inverse square law with which the atoms travel across the chamber over a distance d_c. Material emitted by the sputter gun has a weak directionality which is described by Knudsen's cosine law: the number of atoms emitted is proportional to the cosine of their emission angle normal to the surface [103]. Including Knuden's cosine law when integrating over the half-sphere into which the target emits material yields a factor π: $\int_0^{2\pi} d\phi \int_0^{\frac{\pi}{2}} cos\theta sin\theta d\theta = \pi$. Note that the cosine arises from Knuden's cosine law and the sine is included because it is part of the differential solid angle element.

The second term converts the rate of atoms per second to a deposition rate of thickness per second, $R_{thickness}$, using the substance density ρ, molar mass m, and Avogadro's number N_A.

$$R_{thickness} = \frac{R_{atoms}}{\pi d_c^2} \frac{m}{N_A \rho} \tag{3.3}$$

A typical target-to-substrate distance of 30cm yields a rate of 0.3Å/s for the titanium deposition parameters stated above. Comparing this calculated value with the actual 0.1 Å/s rate observed shows that even relatively simple assumptions provide a reasonable estimate for the deposition rate.

3.2.3 Reactive sputtering

Sputtering silica provides the crucial insulator layer for the MIM structure and a "test" layer with which the surface sensitivity is demonstrated. Silicon readily reacts with oxygen in atmospheric conditions, evidenced by the growth of a native oxide layer on silicon substrates [104]. However, in a vacuum there are considerably fewer oxygen molecules available for such a reaction and in order to create silicon dioxide, external oxygen is supplied. Oxygen enters the chamber through the reactive gasses inlet in figure 3.3b. It is instructive to show that collisions with these oxygen atoms are indeed likely to occur. The mean distance between these collisions is given by the mean free path L_{mfp}:

$$L_{mfp} = \frac{1}{n\pi d_m^2} \tag{3.4}$$

where *n* is the number density of background gas molecules and d_m is the diameter of these sputtered particles emitted from the target [105]. The number density of molecules n can be estimated from the ideal gas equation $P = nk_BT$ by using pressure *P*, temperature *T* and Boltzmann's constant k_B. For typical values of $7x10^{-3}$mbar background pressure, 300K temperature and 300pm as the approximate diameter of a silicon atom, the subsequent mean-free path is 2cm, less than 10% the 30cm target-to-substrate distance. The actual mean free path will be lower than the number quoted here because the sputtering process produces small clusters of silicon atoms rather than individual atoms which increases the d_m^2 term. A larger d_m^2 means a particle has a larger cross sectional area with which another particle may collide with it, increasing the probability of collisions and thus decreasing the mean free path. Therefore it is highly likely that these clusters of silicon atoms do indeed collide with oxygen molecules to form silica during the deposition process.

3.2.4 Pulsed DC Magnetron sputtering

Sputtering can be used to deposit both metals and dielectric materials. When dielectric materials are deposited, the inside of the sputterer chamber is coated with insulating material on which free charges from the plasma may build up. Such regions of high charge could create arcs- short, fast avalanches of charge onto the target. These arcs cause material to be unevenly removed from the target and particles to form in deposited films as a result. These non-uniformities cause films to be

unsuitable for nanoscale photonics applications. To mitigate this arcing, the DC voltage applied to the gun is periodically switched off, or "pulsed," to allow dielectric-coated surfaces inside the chamber to discharge [106], hence the sputtering used in this work is performed with a "pulsed DC" voltage.

The deposition rate estimate above assumes every ion contributes to ablation of material from the target. This assumption is an over-estimate and in practice we want to increase the deposition rate by increasing the number of ions contributing to ablation. The number of ions that contribute to ablation is increased by confining the plasma closer to the sputter target. This confinement is achieved with a magnetron: an arrangement of magnets inside the sputter gun, behind the target [102]. Magnets exert a force on moving charged particles proportional to their velocity and in a low-temperature sputtering plasma the electrons move faster than the argon ions so the dominant force they experience is due to their motion in the magnetic field. The force is perpendicular to the electron velocity and confines them in a circular path above the target surface. These confined electrons ionize argon atoms in their circular path [107]. The argon ions move slower so experience a smaller force from the magnet, instead the dominant force on the argon ions is the electric field of the sputter gun, which accelerates them towards the sputter target. The circular drift path of the electrons and subsequently ionized argon atoms is evidenced by the characteristic "racetrack" pattern in a used sputter target shown in figure 3.3d.

3.2.5 Adhesion layers between gold and silica

Not all materials readily adhere to one another and good adhesion between gold and silica layers is essential for realizing the MIM structure. Gold, as a noble metal, does not readily react with another material, so also does not adhere very well to silica. An adhesion layer was required between the bottom layer planar gold and the silica insulator layer, and between the silica insulator layer and the top metal feature. Gold was attached to the silica substrate by Norland optical adhesive during the template stripping procedure so an additional adhesion layer between the substrate and the gold was not required. Gold adhesion to silica can be promoted by depositing a thin intermediate layer which itself adheres both to the gold and the silica layers either side. Two common adhesion materials are chromium and titanium. Ref [108] compares these two metals and, while both metals show optical absorption, titanium is a superior choice for nano-optics applications due to its low diffusion into the gold layer. I therefore chose to use titanium as the adhesion layer. This titanium adhesion layer was sputtered onto the gold immediately before sputtering the silica. Being able to sputter two different materials without having to break vacuum was made possible by the fact that two separate sputter

guns are available, indicated by the two separate ports on the left hand side of the vacuum chamber in figure 3.3a.

Using such a metal adhesion layer works very well, but it brings the disadvantage of optical absorption, hence the layer should be kept very thin; I found that a layer as thin as (nominally) 1nm is sufficient to ensure successful adhesion, thus also minimizing optical absorption. Nevertheless, 1nm of titanium reduced the depth of the absorption dip by approximately 30% in a computer model discussed in section 4.4, which is why I have also considered alternatives. For example, optical absorption is negligible for organosilane-based adhesion layers such as (3-mercaptopropyl)trimethoxysilane (MPTMS) [109], [110]. While these layers are not compatible with vacuum-based processes such as sputtering, I have used them successfully with nanoparticles as described in chapter 7 [46]. Sputtering proved successful for depositing insulator layers with thickness of order 10nm and insulator layers with (nominally) 1nm thickness. Sputtering was used to deposit silica layers and electron beam evaporation was used to deposit gold layers. Electron-beam evaporation is discussed in the next section.

3.2.6 Electron-beam evaporation

The second method for depositing thin layers of metal I considered was thermal evaporation. The metal to be deposited is heated in a crucible to the point where the material evaporates from the source and condenses on the sample surface to form a thin film [102]. There are, broadly speaking, two methods of heating a metal to this point: resistive heating and electron-beam heating. The

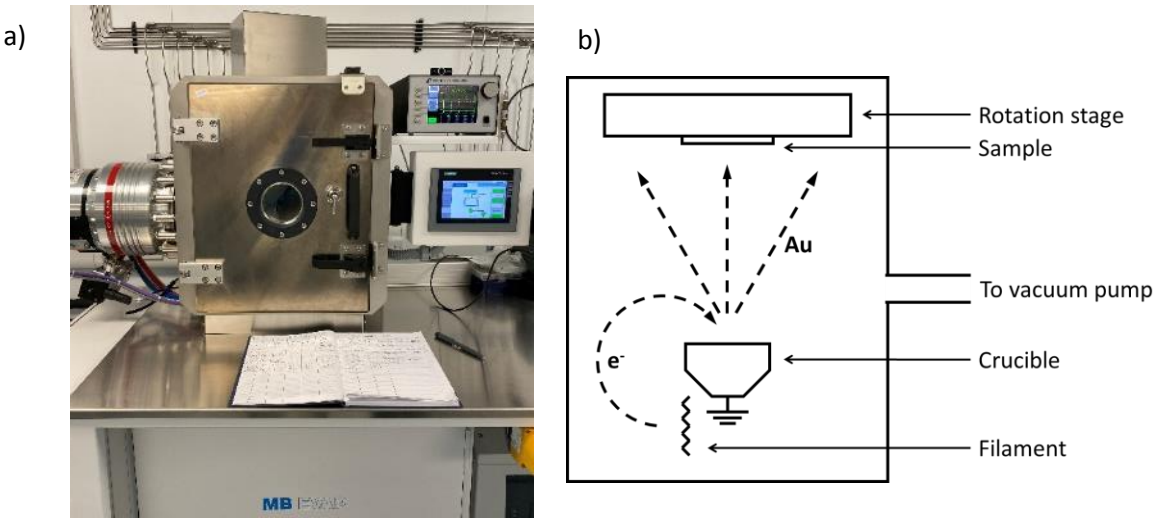

Figure 3.4. Electron-beam evaporator available in the cleanroom at York. a) Photograph and b) schematic showing key components.

evaporator available in the cleanroom and used for this work uses electron-beam heating and is shown in figure 3.4a.

The metal to be evaporated is heated by a 10kV beam of electrons. These electrons are emitted from a tungsten filament held at a negative potential. The beam of electrons is coarsely directed from the filament to the crucible containing the metal shown in figure 3.4b, with additional magnetic confinement provided by a set of electromagnets situated close to the filament. The current in these electromagnets is varied periodically in order to sweep the beam of electrons over the surface of the metal in Lissajous figures, ensuring even heat distribution across the metal.

Similar to the sputtering process, I wanted to obtain a better understanding of the electron-beam evaporation process so considered the basic principles. As a starting point, atoms leave the surface of a material proportional to the vapour pressure of that material at a given temperature. The vapour pressure must overcome the ambient pressure in order to achieve an appreciable removal rate Z_a. The removal rate Z_a. is calculated from the vapour pressure P_{vap} using the Hertz-Knudsen equation [102]:

$$Z_a = \frac{P_{vap}(T)}{\sqrt{2\,\pi m k_B T}} \tag{3.5}$$

where m is the mass of the metal atom , k_B is the Boltzmann constant and T is the temperature in kelvin. The Hertz-Knudsen equation is derived from considering the total number of atoms with a Gaussian distribution of velocities passing through a given area per unit time [111]. The vapour pressure of the metal P_{vap} increases with exponentially with temperature according to the empirical expression provided by Alcock et al [112], indicating that once sufficient temperature for evaporation is reached, only a small temperature increase is required to increase the evaporation rate.

The heated metal in the crucible can be approximated as a point source so the same square-law dependence as in equation 1 can be used. If we assume a similar distance of 30cm above the metal source and an area of 0.1cm^2 which is heated to 1000°C, 1500°C and 1750°C then, according to the formula, we achieve deposition rates of 2x10^{-5}Å/s, 0.1Å/s and 2 Å/s. The evaporation rate in my experiments was typically set to between 0.5 Å/s and 3 Å/s. Therefore, I can deduce that the gold was heated to 1700-1800°C during the evaporation process.

It should be noted that there is a weak directionality to atoms emitted from the heated gold surface. This directionality is captured by Knudsen's cosine law, which states that the number of atoms

emitted during evaporation is proportional to the cosine of their emission angle [103]. Simply put: more metal vapour rises upwards to the substrate than drift sideways to the chamber walls. This directionality is beneficial; it increases the deposition yield during evaporation, which means that the temperature in the above estimation errs on the high side. Furthermore, the cosine law allows us to estimate the deposition rate variation across the size of the sample. For a 15 cm size stage, 30 cm away from the source, the angle subtended from the centre to the edge of the stage is 15°. By Knudsen's cosine law, the maximum variation in rate across this stage is 3%. Such a small variation is not a concern for thin films deposited in this work, especially as the samples I used are much smaller than the stage.

3.2.7 Gold evaporation considerations specific to lift-off

As described above, the metal is heated to temperatures >1500°C; which acts as a black body and places a thermal load on the substrate. Since the sample is made on a glass substrate, it conducts the heat poorly; also recall that there is no convection in a vacuum system. The sample is approximately 30cm from the source. Therefore, the surface of the glass sample gets sufficiently hot to damage the resist layers, which are designed for process temperatures <200°C during the lithography process. Figure 3.5 shows an example of such damage, which is evidenced by the apparent roughness and cracks (figure 3.5a). Figure 3.5b is an SEM micrograph of a gold-coated resist layer which failed to dissolve after over-heating in the e-beam evaporator. One would expect to observe light-coloured rough metal islands against a smooth, dark background, but the sample in figure 3.5b appears as the opposite: dark voids surrounded by a light-coloured rough metal background.

a) b)

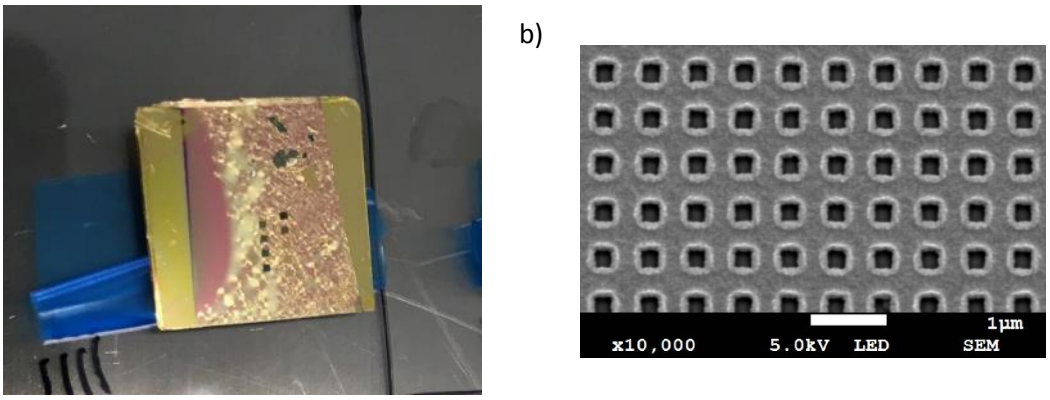

Figure 3.5. Heat damage to the PMMA resist layer from electron-beam evaporation a) Photograph of cracks from over-heating and b) SEM micrograph of features for which the resist layer failed to dissolve.

I initially used an evaporation rate of 0.5Å/s and samples were left at vacuum for 2h after the evaporation process to cool before they were removed from the chamber and avoid thermal shock. Nevertheless, the resist clearly shows cracks from over-heating and it was not possible to remove the heat-damaged resist in stripper solution, as shown in figure 3.5b.

I solved this problem with two alterations that were not entirely intuitive. Firstly, the evaporation rate was increased from 0.5Å/s to 3Å/s to decrease the total evaporation time, and the vacuum chamber was vented immediately after the evaporation process completed so the sample could cool faster. While increasing the evaporation rate does indeed add more heat to the system, the exponential dependence of evaporation rate on temperature discussed above means that a large increase in rate only requires a small increase in temperature; this small increase in temperature is more than offset by the reduced time for which the sample is exposed to the high temperature. These two factors reduced the time the sample spent in the chamber from 2 hours to 45 minutes, reduced heat damage to the resist and enabled successful lift-off of the resist layer.

3.2.8 Surface Roughness comparison between deposition techniques

Surface roughness at metal-insulator interfaces impacts plasmonic resonances. Rough metal surfaces have many spikes which form plasmonic hotspots that act as antennas and radiate. Surface roughness particularly increases attenuation in MIM structures because the spikes on the surfaces of deposited metal films may be ~20% the size of the desired nanogap [113].

Roughness between different surfaces is compared by taking the standard deviation of heights from the mean surface height, denoted the root mean square deviation R_q. I selected the root mean square deviations because it places more emphasis on the "overall" deviations from the mean surface as

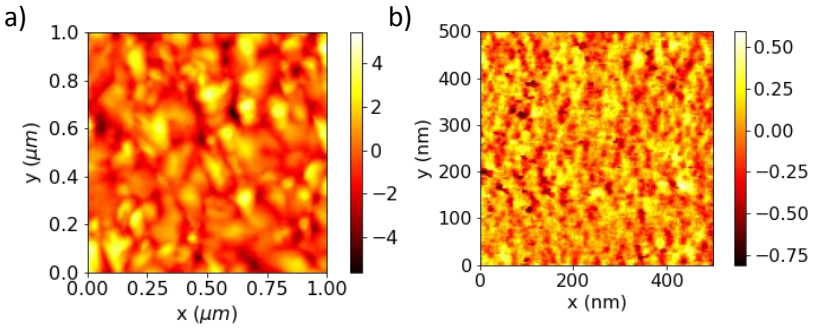

Figure 3.6. AFM traces showing surface roughness of different deposition techniques. a) evaporated gold R_a = 1.4nm and b) sputtered silica, R_a = 0.2nm. Note z range given by the scale bar to the right of each image.

opposed to the absolute deviations which place more emphasis on individual spikes. While an individual spike is problematic for an individual resonator, resonators were fabricated in arrays and the overall array roughness and performance was more important metrics emphasising relatively small numbers of defects or resonators. This roughness value is experimentally obtained by recording surface topography with an atomic force microscope (AFM). Example AFM data from sputtered and evaporated films is shown in figure 3.6.

Evaporating produces a surface with roughness R_q = 1.4nm. Sputtering 10nm or 20nm thick silica produces a smoother film with R_q = 0.2nm so does not limit the smoothness of the resulting MIM stack. Optimising roughness by varying deposition rate resulted in only ~10% improvements to surface roughness R_q. In order to realise metal surfaces with roughness comparable to the silica surface in figure 3.6, a markedly different fabrication process is required.

3.3 Template-stripping

Template stripping is an alternative technique to fabricate smooth metal films. It offers a factor two improvement in surface roughness with a template-stripped film having R_q = 0.6nm, less than half the roughness of the R_q = 1.4nm evaporated gold film. The metal films acquire this low surface roughness

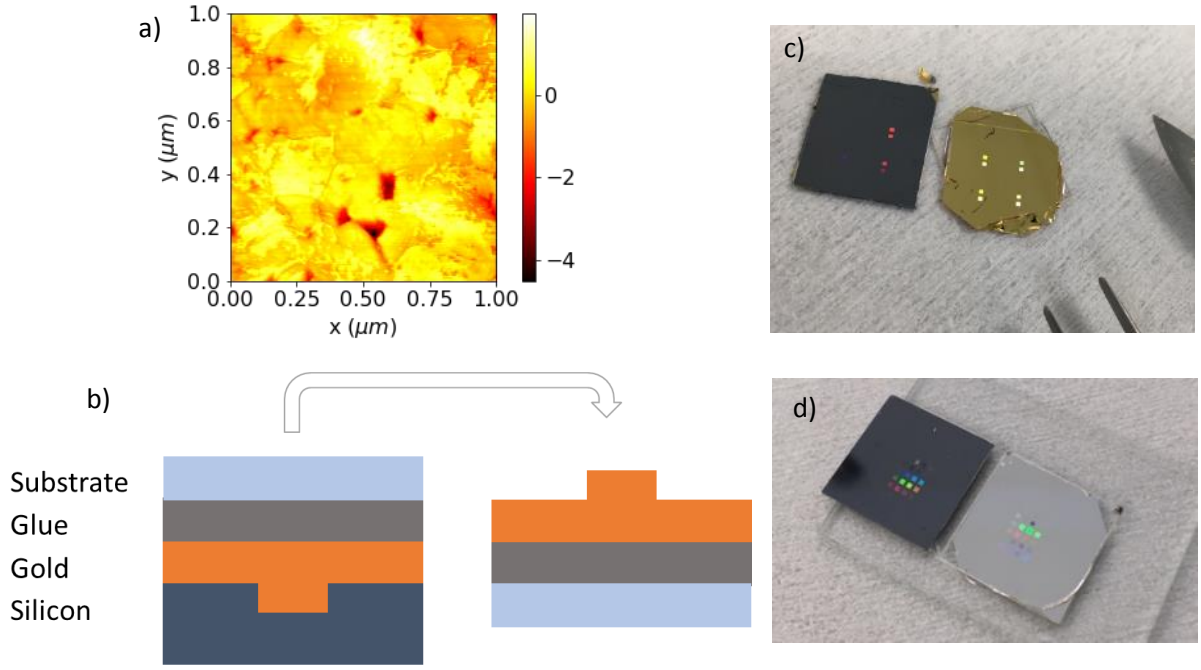

Figure 3.7. Template stripping a) AFM trace of smooth gold film. b) Schematic of template stripping process. Silicon template with diffraction gratings and template stripped c) gold and d) silver films also showing diffractive features.

from a smooth “template,” onto which the metal is deposited [114]. The metal must poorly adhere to the template so that it can be peeled, or “stripped” off. Additionally, the deposited metal conforms to etched or raised features on the template, allowing pattern transfer onto a range of metals including copper and aluminium [115]. Figure 3.7 shows an AFM image of the resulting smooth film, a schematic of this process, and successfully template stripped gold (c) and silver (d) metal films with diffraction gratings.

I had the choice of sputtering silver or evaporating gold to realise the metal substrate for the MIM, both shown in figure 3.7. These options differ in two ways: the deposition method and the metal chemical properties. Firstly, evaporation is a better choice than sputtering because evaporation takes place at a lower base pressure ($5x10^{-6}$ mbar vs $7x10^{-3}$ mbar) so there are less contaminants present during the evaporation process [115]. Secondly, gold is unreactive with any contaminants in the chamber, unlike silver which readily tarnishes. For these two reasons, I chose thermally evaporated template-stripped gold as the MIM substrate in this work.

Template stripped films proved sufficiently smooth to realise MIM resonances by patterning the top surface with either lithography or nanocubes. Both these configurations have insulator thickness of the order ~10nm, an order of magnitude greater than a template stripped film’s roughness R_q. Even smoother surfaces are required for thinner (sub-2nm) insulator gaps in other works and may be achieved by chemically synthesizing crystalline metal films [116].

3.4 Optical measurement setup

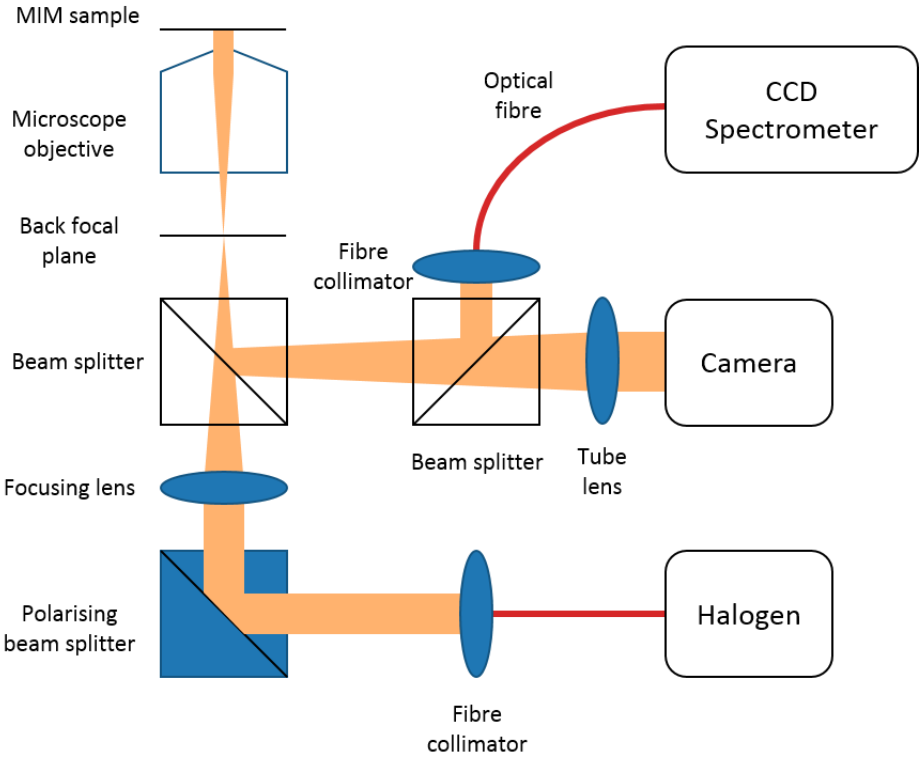

Figure 3.8. Optical setup schematic showing key components and beam path through optical elements.

The MIM resonators were characterised, and their sensing performance assessed, by taking their reflection spectra. Taking spectra of different lithographic MIM designs on the same chip is enabled by simultaneously imaging an area of the chip while recording its reflection spectrum. The above optical setup enabled simultaneously recording the spectra and imaging areas on the device by splitting the beam between a camera and a spectrometer. The polarising beam splitter was used to polarise the light incident on the sample, for example so that TM or p-polarisaiton could be selected to illuminate the 1 dimensional grating structures in section 5.1.2.

The details of required optical components are:

- Olympus NeoSPlan 5x magnification, numerical aperture=0.13, focal length 180mm
- Fibre patch cables: 200 µm core diameter 0.22 numerical aperture, Thorlabs M14L01
- Fibre collimation package: Thorlabs F240SMA-780
- Non-polarizing 50:50 beam splitter: Thorlabs BS013
- Polarising beam splitter: Thorlabs PBS252

- Focussing lens plano-convex focal length 75mm Thorlabs LA1608
- Tube lens: plano-convex focal length 25mm: Thorlabs LA1951
- Camera: photometrics myo coolsnap

The MIM resonance has a ~ 50nm full width at half maximum (FWHM) so recording spectra of different MIM structures with a range of peak wavelengths was enabled by a bandwidth ~10x this FWHM. This bandwidth is provided by a halogen light source operating in the vis-NIR (Ocean Optics HL2000 halogen source) together with a spectrometer (Thorlabs CCS175 spectrometer, resolution 6px/nm) which records between 500-1000nm. The resulting 500nm wavelength range is sufficient to characterise a variety of resonance peaks from different MIM structures and quantify their sensing performance.

The lithographic MIM structures in chapters 4 and 5 are periodic and their grating coupled SPP resonance peak position depends on angle of incidence. The angular distribution of incident light was minimised by illuminating the structures with a collimated beam. The collimated beam was formed by focussing the light source in the back focal plane of the microscope objective.

3.5 Microfluidics

Experiments in this work required exposing MIM resonators to different fluids while simultaneously measuring their optical response. The change in optical response caused by fluids covering the resonators was isolated from changes in resonance between different areas on the same chip by keeping the chip position constant throughout the measurement. Keeping the MIM chip in the same position while flowing different fluids over it was enabled by microfluidic assemblies described below.

There were two methods available for fabricating a microfluidic channels during the project: polydimethoxysilane (PDMS) or stereo lithography (Form 2 and Form 3 3D printers). 3D printing has some advantages over PDMS. There are industry-standard fluidic interconnects (Luer locks) which may downloaded from the internet and included in 3D printed designs [117]. The 3D printed plastic is more mechanically stable for optical measurements because it is stiffer than PDMS. 3D printing is a batch process with higher throughput than PDMS, making it more transferrable to industry production [118]. For these three reasons, I selected 3D printing for making microfluidic parts.

The MIM substrate has 150nm thick metal so MIM structures cannot be measured from the bottom of the substrate and they must be measured from the top, through the analyte. In order to measure through the analyte, a transparent glass window was included in fluidic designs above the MIM. The

potential for leaks was minimized by closely matching the size of the glass window and MIM chip to their designated holes in the 3D printed components. The close match was achieved by dicing the MIM substrate and glass window to 15x15 mm^2 with a dicing saw (Disco DAD 300) and defining a 15.10 x 15.10 mm^2 recess in the 3D printed components to match. The 0.1mm was included as tolerance since 3D printed parts may contract during the curing procure.

Stereolithography lifts 3D printed components from liquid resin as they are defined. Excess resin may block fluidic channels so it must be thoroughly washed off freshly printed parts. The resin is rinsed off by agitating the components in isopropyl alcohol. The rinsing procedure had three steps: a manual coarse wash for 30 seconds, a manual fine wash for 30 seconds and an automated wash (Form Wash bath) for 1 hour. After the automated washing step, the components were blown dry with compressed air, paying particular attention to the channels and Luer locks. The 3D printed components were finished and stiffened by drying them in a UV curing oven at 50°C for 1 hour (Form Cure oven).

3.5.1 Two-part assembly

I defined fluidic channels on one plate and sealed them with a second base plate, illustrated in figure 3.9. Defining “open” channels allows them to be inspected and cleared of excess resin before sealing the two plates together with double sided fluidic tape.

The MIM resonator chip and borofloat glass window were sealed in place to the bottom and top plates respectively with two part epoxy. The two-part epoxy was mixed in equal parts for 45 seconds and applied to the base plate and edges of the window in the top plate to form a watertight seal before gluing the two plates together.

The two components were secured together by placing 3M double-sided tape onto the top plate. The tape was cut into the shape of the channels and around the alignment squares using a scalpel, shown in figure 3.9c. The two components were pressed together using stationery clamps overnight to remove bubbles and ensure a watertight seal. The edges of the taped components were sealed using epoxy to further mitigate possible leaks. The tape and epoxy were left to set and dry overnight.

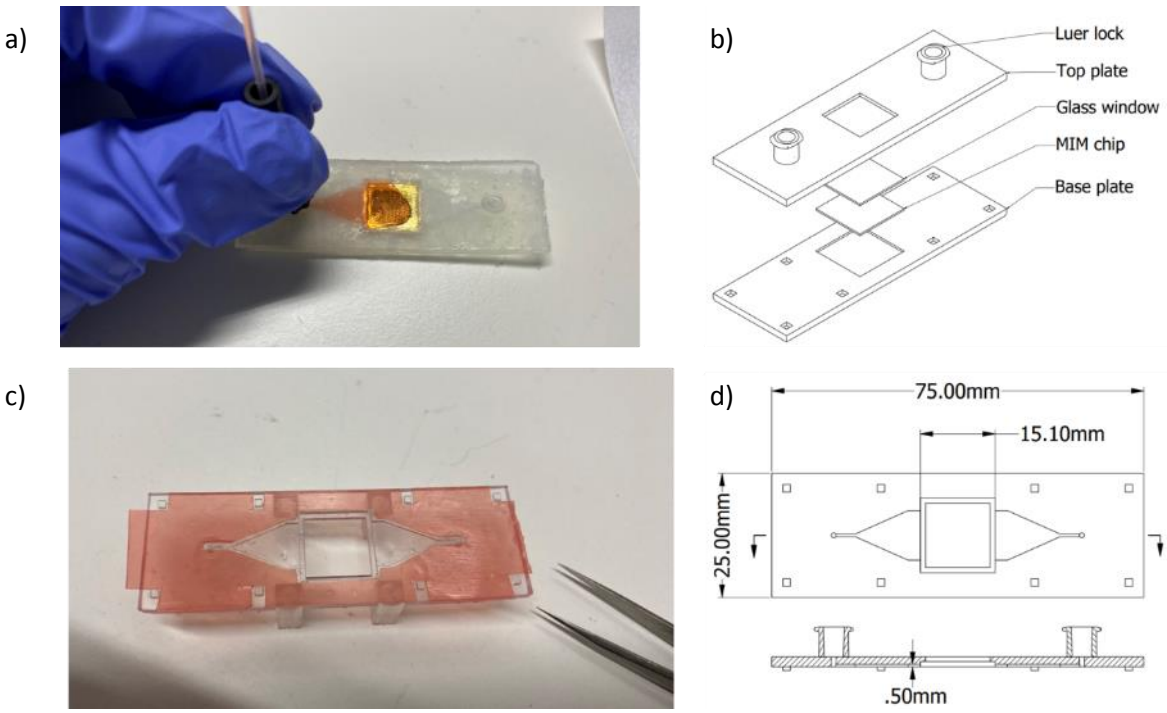

Figure 3.9. Two-part microfluidic assembly. a) Red food dye flowing through the fluidic assembly. b) Assembly constituent parts in an expanded view. c) Double-sided tape applied to glue the two 3D printed components together and d) details of the top plate showing channels, device width, length and minimum channel dimension.

The above design and process has two main limitations. The first limitation is that the channels are realized by the tape so they have a join along the length of the channel. The join along the length of the channel made this assembly susceptible to leaks. Secondly, the clamping required an overnight step which slowed the prototyping and measurement cycle.

3.5.2 Encapsulated channels

I designed, printed and tested an alternative fluidic assembly which was less susceptible to leaks and did not require an overnight step to prepare. These improvements were a result of using encapsulated channels. The encapsulated channels were enabled by a high resolution 3D printer (Form 3) and attentive washing steps.

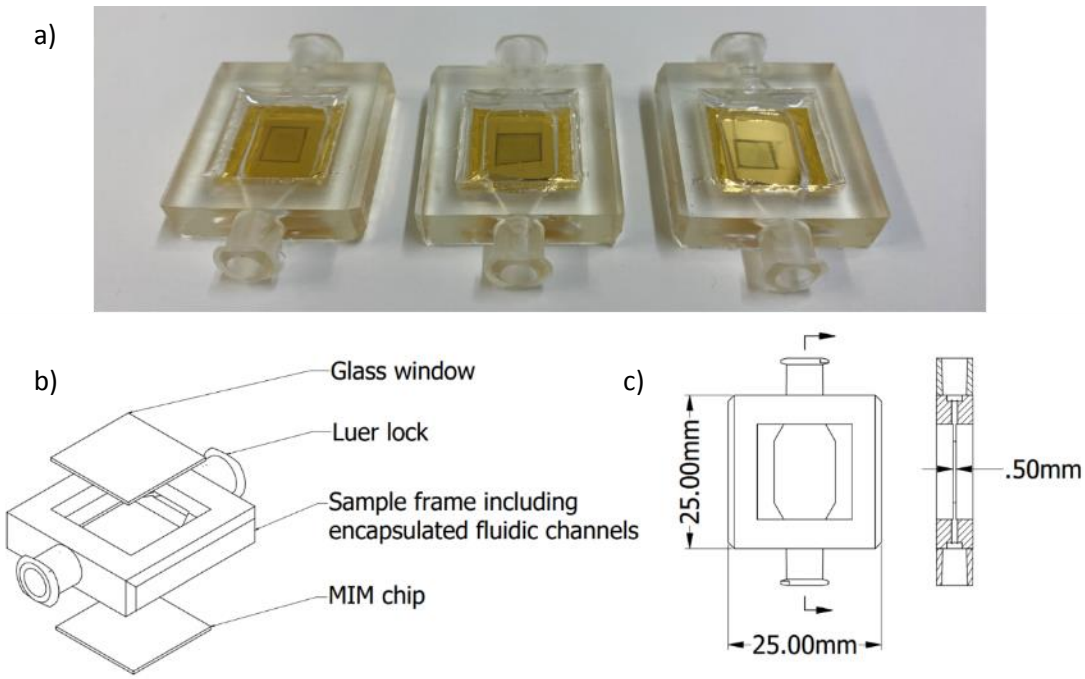

Figure 3.10. Encapsulated channel microfluidic assembly. a) Photograph of three assembled encapsulated fluidic channels. b) Expanded view of encapsulated channel components and c) details of sample frame showing device width, length and minimum channel dimension.

The encapsulated channel fluidic assembly was prepared by 3D printing the sample frame component in figure 3.10. I cleared the encapsulated channels of excess resin by filling a syringe with isopropyl alcohol, inserting it into each Luer lock and gently pushing fluid through the sealed channels before the standard washing steps above. After the standard washing steps, the sample frames were blown dry with compressed air, paying particular attention to the sealed channels. The MIM chip and borofloat glass were secured in place with a watertight seal using Araldite Rapid Epoxy Adhesive and left to set for 30 minutes.

This sealed channel design had fewer leaks than the previous design and did not require an overnight step, enabling rapid prototyping and a faster measurement cycle. This fluidic assembly was used for the bulk LED measurements in section 7.3 and the alkane thiol measurements in section 8.1.2.

Chapter 4

Simulations of Lithographically made MIM resonators

It is important to understand how the MIM's geometrical parameters defined in figure 4.1 affect the structure's optical response. An idealized model is important for guiding the fabrication effort by narrowing parameter sweeps and providing numerical results to which experimental results can be compared.

The starting point is an analytical solution of the MIM system, which is obtained by combining the analytical dispersion relation with the Fabry-Perot model, both given in chapter 2, to approximate the MIM's resonant wavelength [16]. This approach will only provide an approximation of the resonance wavelength and it lacks the electromagnetic field distribution in the structure, but serves as a useful "reality check". More details can be obtained from a computational tool, which solves a discretized form of Maxwell's equations for arbitrary arrangements of permittivity and permeability. One such computational tool is the rigorous coupled wave analysis (RCWA) described in chapter 3.

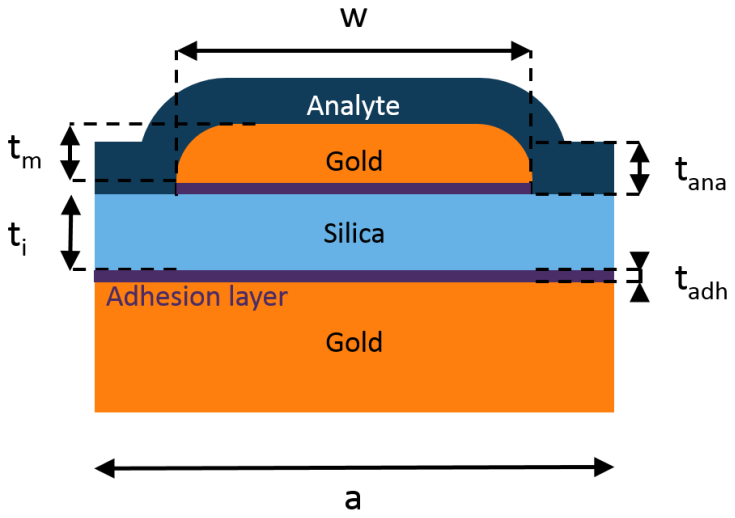

Figure 4.1. Schematic of a MIM resonator fabricated using electron-beam lithography with width w, top metal thickness t_m, insulator thickness t_i, adhesion layer thickness t_{adh}, analyte thickness t_{ana} and period a. Gold is marked in orange, silica in light blue, analyte in dark blue and adhesion layer in purple.

The typical parameters of a MIM resonator are width w=300nm, period a=600nm, dielectric thickness t_i=20nm and top metal thickness t_m = 20nm. These parameters are used for every simulation in this chapter unless explicitely stated otherwise.These parameters are representative of the experimental resonators described in chapter 5. The sub- and superstrates consist of semi-infinite layers of gold and water, respectively. Two titanium adhesion layers, each 1nm thick, are shown as thick purple lines in figure 4.1. 1D periodic arrangements of MIM resonators in 2D geometry are simulated in sections 4.1 to 4.7 and 2D periodic arrangements of MIM resonators in 3D geometry are simulated in sections 4.8 and 4.9. All structures in this chapter are illuminated at normal incidence with p- or TM polarisation unless explicitly stated otherwise. The dispersion of gold is incorporated by interpolating the generally accepted material parameters provided by Johnson & Christy [4].

4.1 RCWA convergence

A typical RCWA simulated spectrum of the structure in figure 4.1 is shown in figure 4.2a. The structure is periodic in 1D and geometry is defined in 2D, and has the typical geometry and illumination parameters listed in the preceding paragraph. Recall from chapter 3 that the finite number of Fourier series harmonics limits the accuracy of the calculation. I ensure sufficient accuracy by increasing the number of harmonics until the resonance peak position shows negligible variation; until the resonance peak position converges.

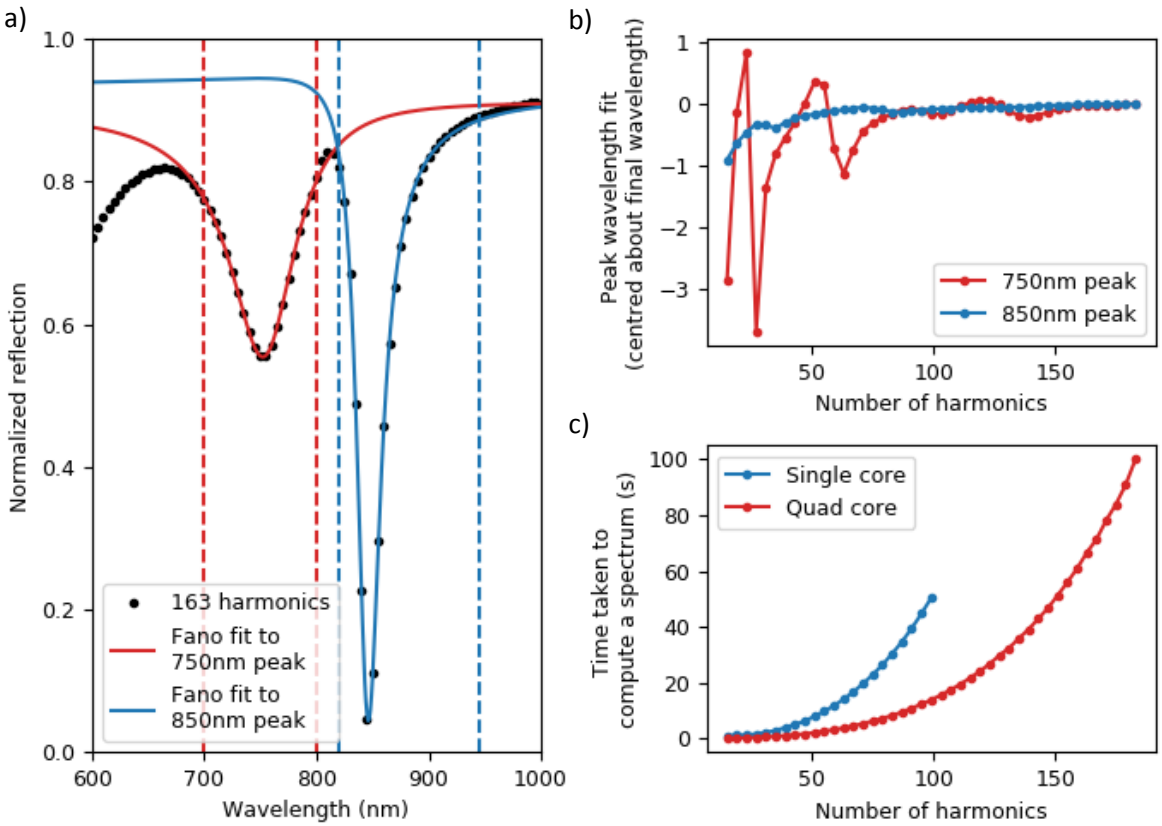

Figure 4.2. Convergence of RCWA simulations. a) Spectrum of a MIM structure calculated using 163 harmonics showing two distinct peaks at 750nm and 850nm. Fano profiles are fitted to both peaks. The wavelength range used to fit the peaks is shown with dashed lines. b) The convergence of both peaks as a function of number of harmonics used. c) Time taken to calculate a spectrum using a single or quad core microprocessor, as a function of the number of harmonics used.

Both resonance dips show asymmetry and they affect one another by their anti-crossing behaviour discussed in section 4.3. In order to account for this asymmetry, I fit an asymmetric Fano profile to both peaks. The Fano profile is given by equation EQN. Note that if no asymmetry is present (q=0) the Fano profile reduces to a Lorentzian profile but when data shows asymmetrical features the Fano profile provides a more accurate curve fit by accounting for this asymmetry exhibited by both peaks. The Fano profile is given by equation (4.1)

$$\mathrm{f}(\lambda) = 1 - \mathrm{a}\frac{\left(q + \Omega\left(\lambda\right)\right)^2}{\left(1 + \Omega\left(\lambda\right)^2\right)} - b \tag{4.1}$$

$$\Omega(\lambda) = \frac{2(\lambda - \lambda_0)}{\Gamma} \tag{4.2}$$

Where λ is wavelength, λ_0 is resonance wavelength, Γ is the linewidth parameter, a is the amplitude (peak depth), b is the vertical offset parameter, and q is the asymmetry parameter. Note how if q=0

then the Fano profile reduces to a Lorentz profile [119]. The $\Omega(\lambda)$ was included to make the functional form more clear maintain consistency with ref [119].

Figure 4.2b provides example convergence data, measured as the difference between the wavelengths of the two resonance peaks calculated with 163 harmonics and wavelengths of the resonance peaks calculated with fewer harmonics, expressed as a function of the number of harmonics used in the calculation. When more than ~100 harmonics are used, the deviations in peak wavelengths are smaller than 0.3nm and above 150 harmonics, the deviations are smaller than 0.1nm. Deviations of 0.1nm are an order of magnitude smaller than the simulated wavelength shifts of order 1-3 nm used to calculate bulk and surface sensitivity below. I therefore used 163 harmonics in all subsequent simulations.

Recall from section 3.1.1 that RCWA requires a sufficient number of spatial harmonics to resolve the geometry which supports resonant modes. The slower convergence of the 750nm feature is expected because the resonant mode is localised underneath the top metal feature (Figure 4.3a, b), which requires a high (>100) number of harmonics to resolve in reciprocal space. Conversely, the 850nm feature is due to the periodicity of the structures (section 4.3) which is present when at least one spatial harmonic is is used. Therefore, one would expect the ~850nm dip wavelength value to converge faster than the ~750nm dip wavelength value which is evidenced in Figure 4.2b.

The dispersive nature of gold is incorporated by running separate simulations with the complex permittivity for gold specified for each wavelength. Each spectrum included a data point at 80 regularly spaced (5nm) wavelengths between 600nm and 1000nm. These wavelength-separated calculations offer themselves for parallel execution. Figure 4.2c shows an example; while computation time increases with the cube of the number of harmonics [94], the time can be significantly reduced by taking advantage of a quad core processor found in many modern desktop and even some laptop computers.

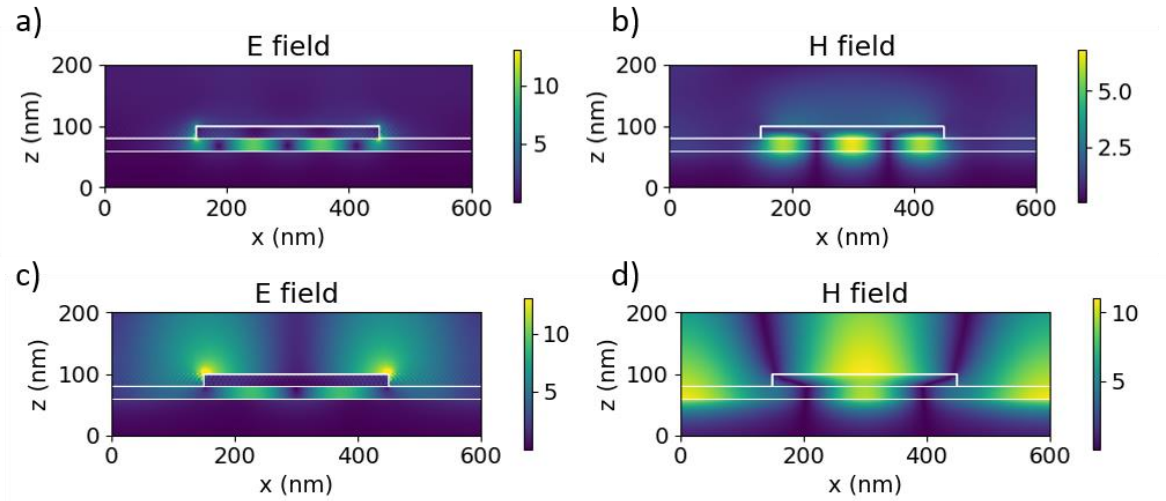

Figure 4.3. RCWA field plots. a) |E| field at 750nm, b) |H| field at 750nm. c) |E| field at 850nm and d) |H| field at 850nm. The field amplitude shown by the colour bar is normalised to the incident electric field amplitude.

We can further improve the identification of the various resonances in figure 4.2a by calculating and plotting their electric and magnetic fields, shown in figure 4.3. For example, the |E| and |H| fields of the resonances studied in figure 4.3a,b qualitatively agree with previously published work on MIM resonances [35], [38], [40]. The H field (figure 4.3b) shows three distinct lobes, indicating that the 750nm peak is the 3rd order MIM mode. The E field (figure 4.3a) shows two distinct lobes in the middle of the resonator and one can interpret the lobes in figure 4.3a and b as standing waves in the MIM nanogap. Figure 4.3a also has tightly confined E field hotspots at the corners on either side, where the resonant mode extends into the medium above the sensor surface. Figure 4.3c shows how the E field hotspots at the corners of the MIM rectangle extend comparatively further from the resonator surface than those of the MIM mode in figure 4.3a. Figure 4.3d shows distinct lobes on the metal surfaces outside of the MIM nanogap, implying that this resonant mode is more weakly localized and extends across the whole array, thereby also occupying the space between the MIM islands. Tightly confined E field hotspots at the corners of the MIM rectangle in figure 4.3a suggest that this MIM mode may be highly sensitive to changes in refractive index on its surface, potentially more sensitive than the distributed E field in figure 4.3c This dilemma will be investigated in sections 4.6 and 4.9.

4.2 MIM array geometry

The MIM array geometrical parameters change its optical response, can be used to tune the dip positions and identify the physical nature of each resonance dip. Figure 4.4 shows how both width (a) and period (b) of a 1D periodic MIM array defined in 2D geometry may be used to change the resonance dip position respectively of each peak in the spectrum. In figure 4.4a, the period is held constant at 600nm while the resonator width is varied in 10nm steps. The resonator width has a much greater effect on the 750nm dip than on the 850nm dip, which strongly suggests that the 750nm dip is the localized MIM resonance. In contrast, in figure 4.4b, the resonator width is held at 300nm and the period is varied. These changes now have a comparatively greater effect on the 850nm peak than on the 750nm peak, implying that this dip arises from periodicity and that this resonant mode is distributed over the entire MIM array.

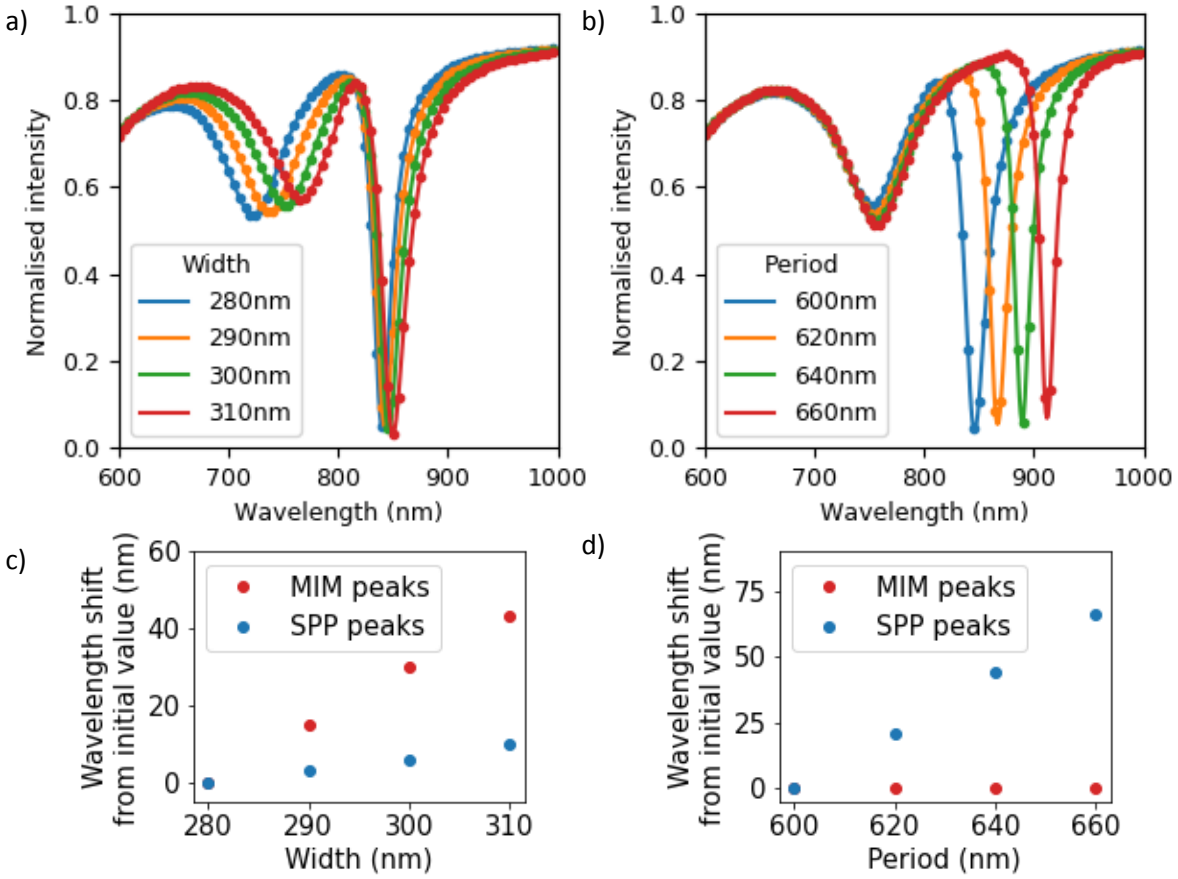

Figure 4.4. Parameter sweeps of 1D MIM array a) width and b) period. C) peak wavelength shifts due to changing c) width and d) period of the 1D MIM array.

It is therefore clear that the MIM and grating resonance wavelengths can be tuned independently. The MIM mode is confined within the square MIM islands and its resonance wavelength is a function of the resonator width, consistent with the Fabry-Perot model of MIM resonators [16], [38].

4.3 Grating peak physical origin

The 750nm dip has now been identified as a MIM peak, but the physical origin of the 850nm dip still requires explanation. The 850nm dip period dependence implies coupling via the periodicity of the 1D periodic MIM array and its H field plot shows qualitative similarities to the H field of an SPP in chapter 2. The physical origin of this periodic peak can be interrogated by treating it as a grating peak and examining its band structure. There are two ways to infer the band structure of this peak: sweep the angle of incidence, and vary the period of the structure.

First, I study the polar angle of incidence, ϕ, in order to further characterize the modes. The simulated structure was illuminated with p-polarised light and the 1D periodic array had a period of 600nm and feature width of 300nm. One would expect a highly localized mode to be angle-tolerant, while the resonance position of a distributed grating-like mode should exhibit a strong dependence on angle. This study of angular dependence is shown in figure 4.5a. It is clear that the 750nm MIM peak position does not change with angle but that it exhibits an anti-crossing behaviour with other resonant modes. This anti-crossing behaviour shows that the MIM and SPP modes have similar symmetry and can couple to one another. Conversely, only a few degrees are sufficient to show that

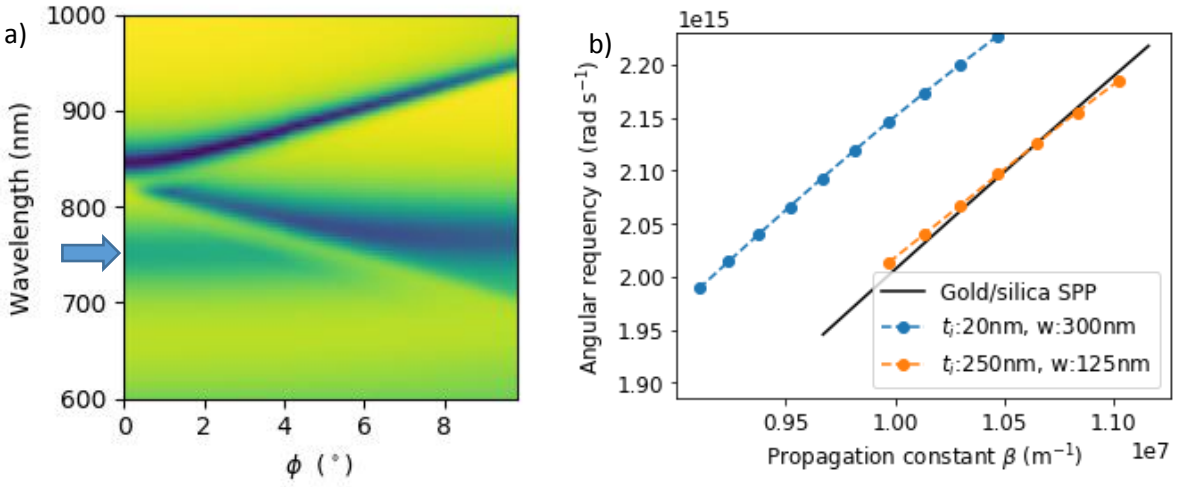

Figure 4.5. MIM array dispersion relation a) Polar angle of incidence sweep with the MIM trend line marked by a blue arrow. b) MIM array dispersion relation for two different insulator thicknesses t_i and resonator widths w showing that thicker silica and smaller metal features more closely approximates the gold/silica SPP dispersion relation.

the 850nm peak changes with angle of incidence which further supports that it is a grating-type resonance.

This study can be furthered by comparing the ~850nm resonance dispersion relation with the analytical SPP dispersion relation given in chapter 2, as in figure 4.5b. One would expect that the MIM periodic resonance wavelength will be $\propto \sin(\phi)$ (equation (2.17), section 2.3.1). In more exact terms, the periodic feature resonant frequency will approximate a gold/silica SPP dispersion relation, with some perturbation for the finite silica thickness and the presence of the metal features. I decrease these perturbations by making two adjustments to the original MIM structure in figure 4.1: increase the silica thickness to 250nm and decrease the resonator width to 125nm. When these adjustments are made, the grating dispersion (orange circles) closely approximates the gold/silica SPP dispersion (black line). The remaining deviations can be explained by recognizing that the structure still includes a finite silica layer and gold features on top of this silica layer which still perturb the SPP, albeit to a lesser extent than when the resonator width is 300nm and the silica thickness is 20nm. I therefore conclude that the resonance observed at 850nm in figure 4.2 is a surface plasmon polariton perturbed by the resonator.

4.4 Adhesion layer thickness

Another effect worth studying is the impact of the adhesion layer on the optical properties of the structure. The structure simulated in this section is a 1D periodic arrangement of MIM resonators defined in 2 spatial dimensions. As explained in chapter 3 a thin film of titanium is deposited before the layer of gold to increase adhesion, but its optical properties are inferior to those of gold; so the Ti layer will reduce the quality of the resonance. There are two titanium adhesion layers in the structure: one below and one above the silica layer as shown in Figure 4.1. The impact of these layers on a 1D periodic MIM array is shown in figure 4.6: a dramatic reduction of the resonance depth for the 750 nm MIM mode, even for titanium films with as little as 1 nm thickness. These observations highlight the strong localization of the mode to the MIM resonator and the correspondingly strong interaction with the adhesion layer. In contrast, the 850 nm extended SPP mode, which exists mostly outside the MIM nanogap and overlaps less with the adhesion layer is broadened and red-shifted. One could interpret the red shift as the optical path between the discrete metal features increasing due to the presence of the titanium layer. Increasing the thickness of the titanium layer increases the SPP mode effective index n_{eff}, thereby increasing the optical path between discrete metal features: n_{eff} x a where a is the period of the periodic structure.

The titanium adhesion layer thickness is therefore an important experimental consideration. If the adhesion layer is too thin, the various layers will not adhere and the structure easily disintegrates; if the adhesion layer is too thick then the MIM resonance suffers. The simulations suggests to use an adhesion layer no thicker than 1nm of titanium.

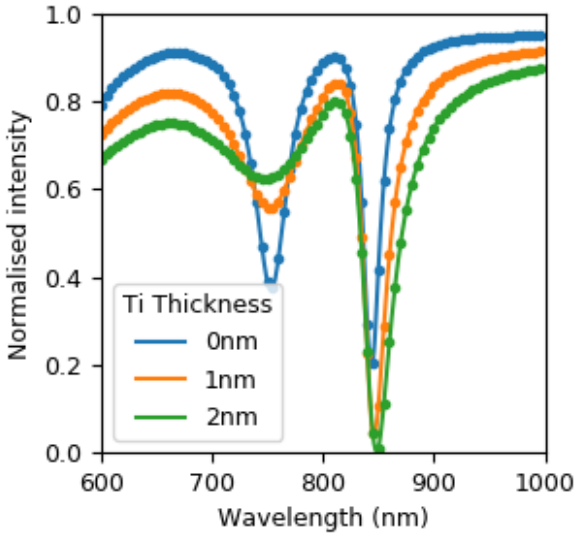

Figure 4.6. Impact of different adhesion layer thicknesses on both resonance peaks.

4.5 RCWA bulk sensitivity

The aim of developing the MIM geometry described above is to use it as a resonant refractive index sensor, similar to those described in chapter 2. A resonant refractive index sensor will change its response when exposed to media of different refractive index. Since RCWA allows permittivity values and spatial distributions to be defined and varied within its computational domain, it provides an opportunity not only to investigate how geometry affects the resonant modes, but also how these modes respond to changes in their surroundings. A 1nm titanium adhesion layer is included in this model of 1D periodic MIM resonators in order to better represent a how a fabricated array of MIM resonators would perform. The structure simulated in this section is a 1D periodic arrangement of MIM resonators defined in 2 spatial dimensions

A common sensing metric is a refractive index sensor's bulk sensitivity. The bulk sensitivity is a measure of how the sensor responds to changes in its bulk surroundings. In the context of RCWA, this bulk region is the semi-infinite space above the MIM geometry. The device's bulk sensitivity is simulated by changing the refractive index of the cover media in this semi-infinite space above the sensor surface and calculating the spectrum at each cover refractive index. The cover refractive is varied between 1.33 and 1.45 to match the refractive index of aqueous salt solutions used to experimentally measure the bulk sensitivity in chapter 5.

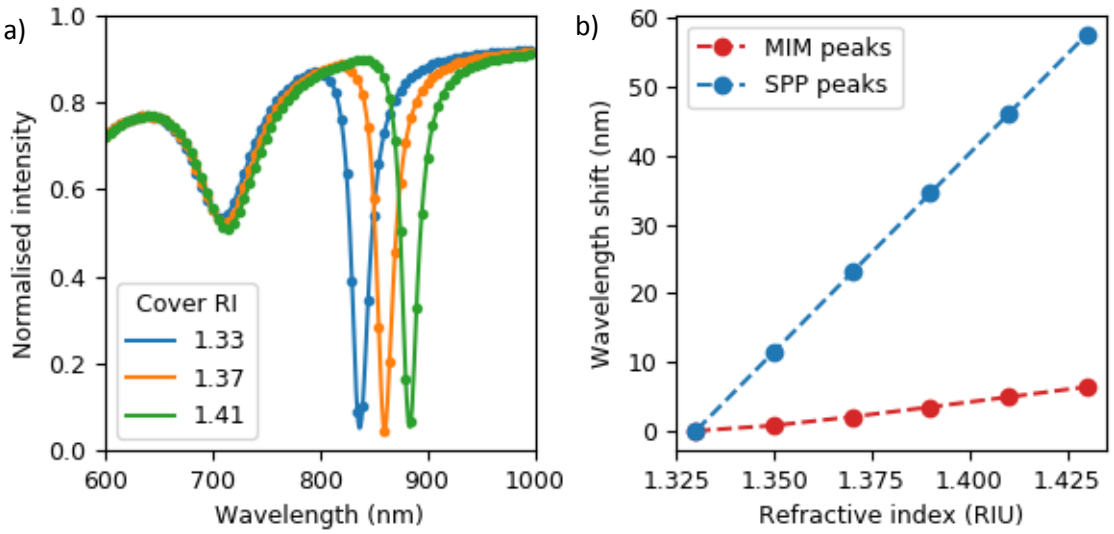

Figure 4.7.Bulk sensitivity modelled in RCWA. a) Example bulk sensitivity spectra and b) peak wavelength shifts for MIM and SPP peaks with refractive index of the cover media. MIM top metal thickness: 20nm

The MIM and SPP modes extend outside the MIM geometry and penetrate into the bulk cover media. This overlap between the resonant mode and bulk analyte increases the effective refractive index of the resonant mode. Increases in the effective index increase the optical path defined by the resonator and shift the resonance wavelength to higher values. Figure 4.7 demonstrates this red shift in resonance peak wavelength for both the MIM and SPP modes. I calculate the bulk sensitivity by fitting Fano lineshapes to each dip as in figure 4.1, then fitting a straight line to the resonance wavelength shifts against the cover media refractive index.

The MIM mode has a relatively low response to changes in bulk media, with a relatively low bulk sensitivity of ~80nm/RIU. This low value qualitatively corresponds to the minimal extension of the MIM mode into the cover media in figure 4.3 c. The SPP mode, in contrast, responds much more strongly to changes in the surrounding medium and exhibits a bulk sensitivity of 564nm/RIU. This

higher bulk sensitivity can be explained with the SPP E field's further extent into the cover medium, both upwards from, and into the space between top metal features which is apparent from figure 4.3c and d. Both resonant modes are sensitive to changes in *some* of the space between structures and the SPP electric field extends more into this space than the MIM mode, which is more localised to the discrete metal features.

4.6 Surface sensitivity

The main use of resonant refractive index sensors is to detect the presence of biomolecules such as antibodies by their binding to the sensor surface [58], [59], [90], [120]. Compared to the determination of the bulk sensitivity, there is a key difference: the biomolecules are only of order ~10nm in length [56], [66]. Therefore, if the resonant mode extends far beyond the detection zone in which biomolecules are located, then the bulk sensitivity can easily over-estimate the biosensing performance of the resonant mode.

A more accurate model of biosensing performance is therefore to define a 10nm thick analyte layer above the sensor surface in order to describe the presence of bound biomolecules. It should be noted that defining such a homogeneous layer above the sensor surface only provides an approximation to the binding of biological molecules. Biological molecules do not cover the surface homogeneously, especially at low concentrations [121]. Nevertheless, modelling the response to refractive index changes in this 10nm layer provides a more accurate description of biomolecule binding than changing the refractive index of the entire medium above the sensor.

The refractive index of this 10nm layer is varied from 1.35 to 1.55 in steps of 0.05 since 1.55 is the upper limit of refractive index of an adsorbed protein layer [121]. The cover refractive index is that of water, 1.33, to approximate the aqueous conditions in which protein binding would occur. I calculate the resonance wavelength shift for both the MIM and SPP mode in the same way as for bulk sensitivity. I expect the surface sensitivity to be lower than the bulk sensitivity as the thickness of the analyte layer is typically lower than the mode size; as shown by the plots in figure 4.3a, c. Figures 4.3a, c show that the fields extend further than 10nm away from the sensor surface so the modes will extend through the analyte layer and overlap with the cover media above.

Finally, the thickness of the top metal feature, t_m, is varied to investigate its effect on the surface sensitivity. The hypothesis is that a thinner top metal layer provides more exposure of the MIM mode to its surroundings, thereby increasing surface sensitivity. Figure 4.8a indeed shows that when the top metal thickness is reduced, the resonant wavelength shifts to larger values. The Fabry-Perot model explains these red-shifted resonant wavelengths as a decrease in effective index of the MIM mode. The decrease in effective index, in turn, increases the evanescent tail which overlaps more strongly with the analyte. Decreasing the top metal thickness increases the surface sensitivity of the MIM mode from 40nm/RIU to 59nm/RIU, confirming the hypothesis. I note that a thinner top metal also reduces the depth of the MIM resonance dip. Therefore, while a thinner top metal results in greater surface sensitivity, this decrease of the resonance dip highlights the practical limitation to maximizing the surface sensitivity by this method.

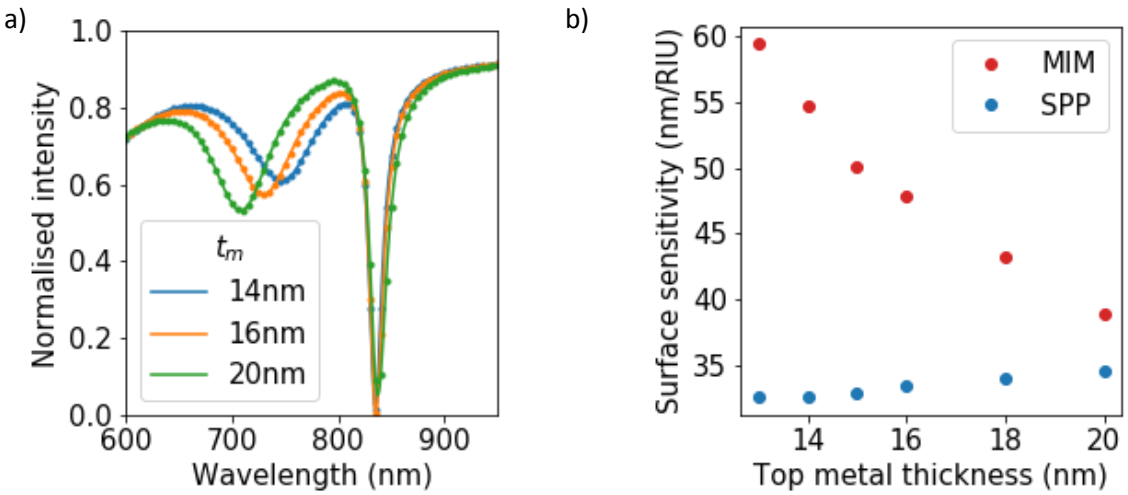

Figure 4.8. Surface sensitivity modelled in RCWA. a) Spectra with different top metal thicknesses, no surface analyte, n_{cov} = 1.33. b) Surface sensitivity with dfferent top metal thicknesses.

4.7 COMSOL-RCWA comparison

COMSOL and RWCA/S[4] use different methods to discretize the MIM structure in space. Therefore, comparing the output from both techniques and finding their results agree builds confidence in these findings. Figure 4.9 is such a comparison of the same 1D MIM array structure defined in 2D geometry (period: 600nm, width: 300nm, insulator thickness: 20nm) between S[4] and COMSOL, both using periodic boundary conditions. The data from both models show two clear dips: the MIM resonance at 750nm and the SPP resonance at 840nm. Both peaks show slight asymmetry in both models. The reflected values are a particularly close match for 710nm MIM dip, and show slightly greater deviations for the SPP dip.

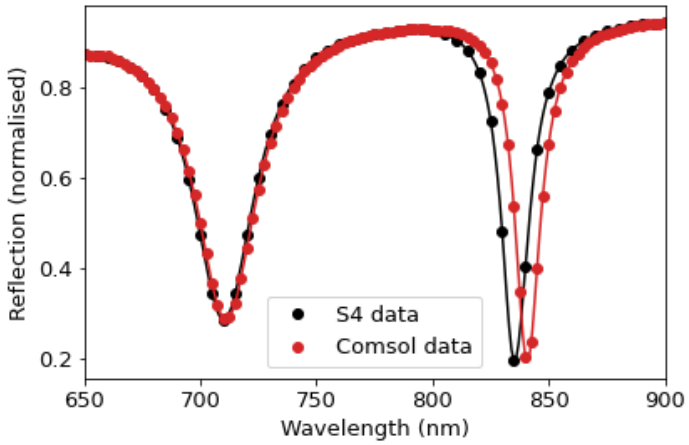

Figure 4.9. Comparison between S4 and COMSOL simulation data of the periodic gold MIM structure.

One possible reason for the larger SPP discrepancy may be due to the resonance's physical origin. The SPP peak arises from the periodicity of the metal features and these two numerical models implement periodicity slightly differently. Recall from chapter 3 that periodicity is a fundamental part of RCWA: it is the foundation for discretizing the structure and electric field. However, COMSOL adds periodic boundary conditions after discretizing the structure with a mesh. Recall also from chapter 3 that S[4] does not scale well to 3D geometries, whereas COMSOL's finite element approach does scale well to 3D and allows the performance of a 3D MIM structure to be assessed in the next sections.

4.8 Bulk and surface sensitivity

The bulk sensitivity results are extended to include a 2D array of of square MIM structures, in 3D geometry realized in COMSOL and the 750nm MIM mode is investigated.. The bulk sensitivity of the MIM structure is simulated by calculating the spectrum reflected by the MIM structure while changing the refractive index of the background medium, much the same as in S[4]. The surface

sensitivity is also calculated by defining a 10nm layer coating the structure in the same fashion as the preceding S^4 discussion.

The structural parameters for this simulated structure are * a 600 nm period, 320nm metal squares which are 20nm thick, on 20 nm thick insulator Rounded corners are rounded with the maximum 20nm radius of curvature using the “fillet” function in COMSOL. Sharp corners have zero radius of curvature.I also compare the effect of rounding the corners on bulk and surface sensitivity. Recall from chapter 3 that perfectly sharp corners are unnatural features and fabricated structures examined under electron microscopes show rounded corners. Rounded corners will decrease the E field hotspot amplitudes at the corners and edges of the resonator. Since sensitivity is proportional to the overlap between the electric field and the analyte, I expect structures with rounded corners to yield lower sensitivity than structures with sharp corners.

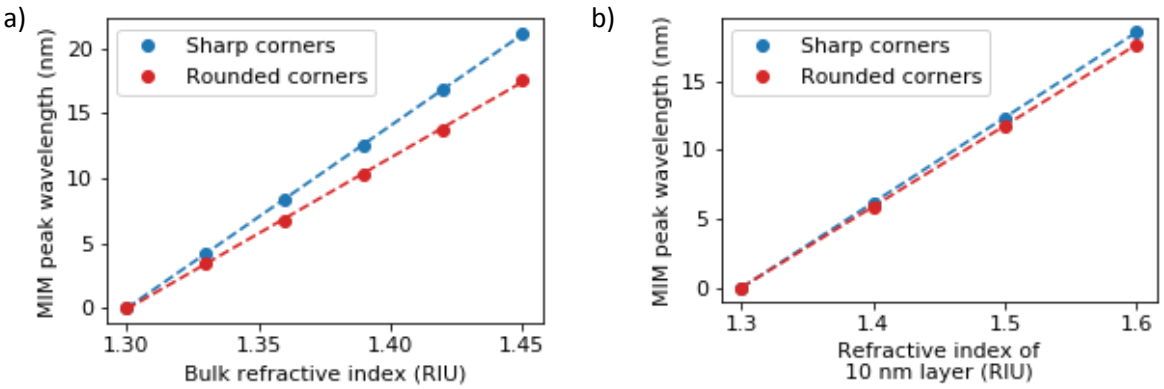

Figure 4.10. Comsol a) bulk and b) surface sensitivity with sharp corners and rounded corners.

The sensitivity results in figure 4.10 support the hypothesis that structures with rounded corners are less sensitive than structures with sharp corners. The bulk sensitivity for a structure with sharp corners is 140nm/RIU, ~15% larger than its rounded corner counterpart which has 116nm/RIU bulk sensitivity. This difference is less pronounced for surface sensitivity, where structures with sharp corners have 62nm/RIU, only 5% more sensitive than structures with rounded corners which have 59nm/RIU surface sensitivity.

Rounding corners reduces bulk sensitivity more than it reduces surface sensitivity. The reduction in bulk sensitivity implies that rounding the corners reduces electric field overlap with the bulk analyte. Mode overlap is reduced by reducing the penetration depth of the electric field from the metal corner into the analyte. Reducing the penetration depth into the analyte will affect surface sensitivity less than bulk sensitivity because the electric field need not penetrate deep into the analyte to probe

the surface; surface refractive changes only take place close (within 10nm) to the resonator, which is confirmed by the data in figure 4.10.These bulk and surface sensitivity values are higher than the S^4 bulk and surface sensitivity values respectively. This increase in sensitivity values is due to increasing electric field overlap with the analyte. The 2D array of squares exposes more metal surface area to the analyte, than the 1D array of metal strips and therefore more detection volume around the metal in which the evanescent electric field and analyte may overlap.

4.9 Origin of high surface sensitivity

The COMSOL finite element model allows placing blocks of analyte into various positions to better understand the origin of high surface sensitivity. The geometrical parameters in this section are the

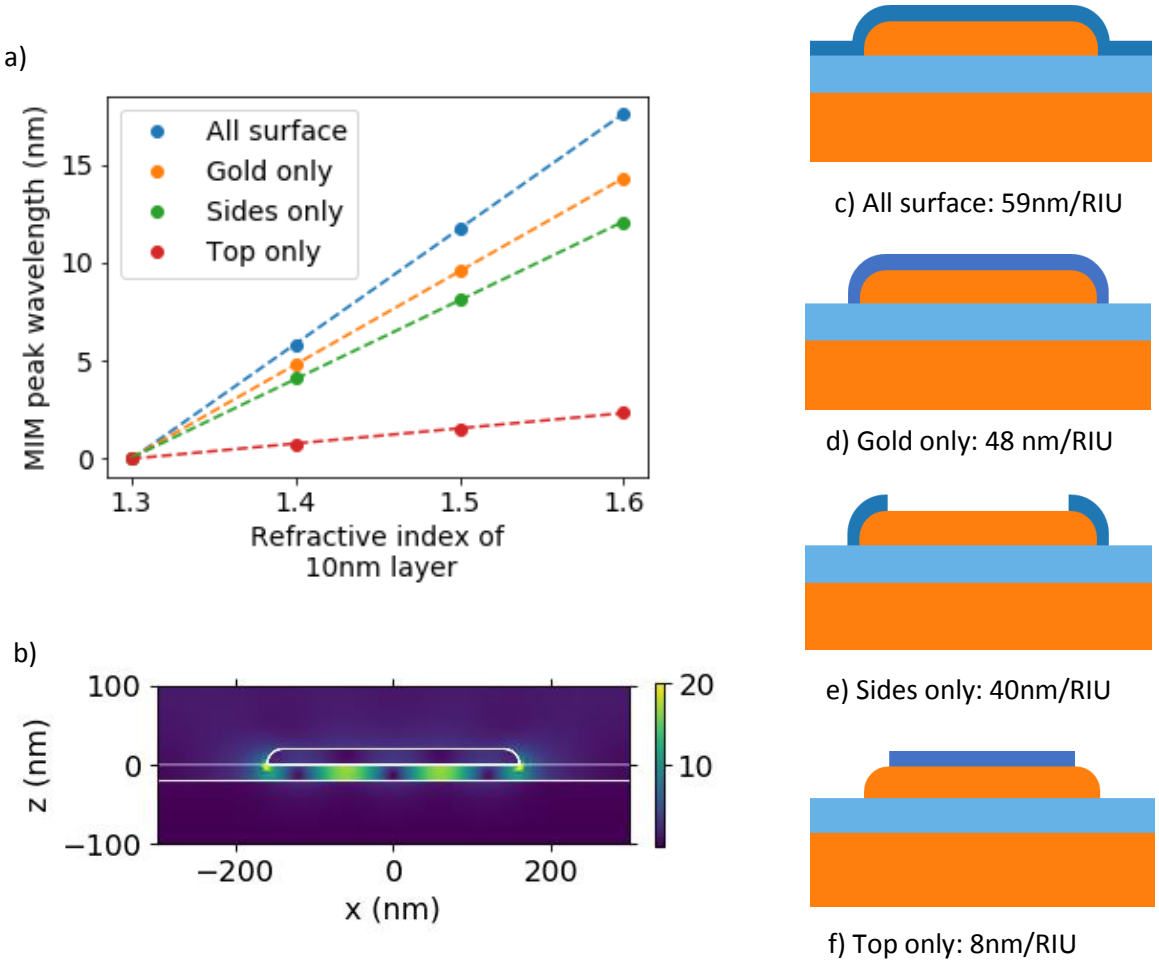

Figure 4.11. Comsol modelling highlighting the most surface sensitive MIM regions. a) Wavelength shifts from coating different areas of the sensor surface b) Electric field plot calculated in COMSOL where the resonant electric field amplitude shown in the plot is normalised to the incident field amplitude. (c–f). Covering only the edges of the resonator as in d) results in much larger wavelength shifts than only covering the top surface as in e).

same as those stated in section Bulk and surface sensitivity4.8. I placed blocks of silica onto the top of the entire surface, covering the gold feature, only onto the side of the gold feature and only onto the top of the gold feature. The sensitivity due to varying the index of these analyte blocks is shown in figure 4.11. The MIM retains its high surface sensitivity when only the gold surface is coated with silica mimicking the case where the gold surface would be functionalized using standard procedures [56].

The fact that the surface sensitivity stays high in figure 4.11d highlights the fact that the majority of the sensitivity derives from the field overlap at the edges of the resonator. This observation that the sensitivity is due to changes at the sides of the MIM resonator is congruent with the electric field plot in figure 4.3, recalling that sensitivity is proportional to electric field overlap with the analyte. The electric field plot shows E field hotspots at the corners of the resonator, which overlap more with refractive index changes over the curved sides of the resonator than changes on the top of the resonator. This qualitative observation of electric field overlap between hotspots at the metal corners with refractive index changes on the sides is consistent with the comparison of sensitivities for figure 4.11d and figure 4.11e.

4.10 Conclusions

The simulations presented in this chapter narrow the fabrication parameters and form expectations for the bulk and surface sensitivity presented in the following experimental chapter. The MIM array geometry sweeps calculated in S^4 provide a method to independently tune the MIM and SPP resonance positions.

The COMSOL and S^4 models show the same spectrum strongly indicating which features one should expect from fabricated MIM resonators. Furthermore, both models show common trends which encourage conclusions to be drawn. Both models show relatively high surface sensitivity compared to their bulk sensitivity, indicating that these MIM modes have tightly confined E field hotspots which effectively probe refractive index changes close to the resonator surface. The S^4 model predicts 80nm/RIU bulk and 40nm/RIU surface sensitivity for a 1D array of MIM strips. The COMSOL model predicts up to 116nm/RIU bulk sensitivity and 59nm/RIU surface sensitivity for a 2D array of MIM squares with rounded corners.

These computer models are not without limitation. S^4 models have unreasonably sharp corners, which are a poor representation of the corners realised in fabricated structures. While both the

Fourier and real space discretised models show internal consistency and convergence to within 0.1% for resonance wavelength values, the exact electric field amplitudes at the sharp bottom corners may not be accurate. Such sharp corners are known to cause numerical instabilities and even numerical singularities [122]. More emphasis should be placed on the calculated trends: the E field is tightly confined to the corners of resonator so the resonant mode retains its high sensitivity, even for a thin layer of analyte on the surface.

Chapter 5

Lithographically fabricated MIM resonators

While the MIM schematic appears simple, realizing such small metal features with sharp edges is non-trivial, as was creating a sufficiently smooth metal surface. Such optimization steps appear obvious in hindsight, and much was learned. The fabrication process went though many iterations. Here, I present the lithography methods I used, their limiting factors and the optimization steps that ultimately resulted in a 2D periodic array of MIM resonators. The process development also included fabricating a 1D periodic array of MIM resonators.

5.1 Electron-beam lithography patterning

Metal-insulator-metal resonators have previously been fabricated by nanoimprint lithography [35] and the relationship between resonator width and resonance wavelength is understood by the community [10], [16], [38], [39], with literature [35], [38] and the simulations in chapter 3 indicating a resonator width of order 300nm for third order modes. This scale falls within the feature size readily accessible by electron-beam lithography (EBL). The EBL process for realizing a pattern in a positive resist is described below, including considerations which proved highly relevant for the MIM fabrication process. Patterning considerations are discussed in this section and pattern transfer is described thereafter.

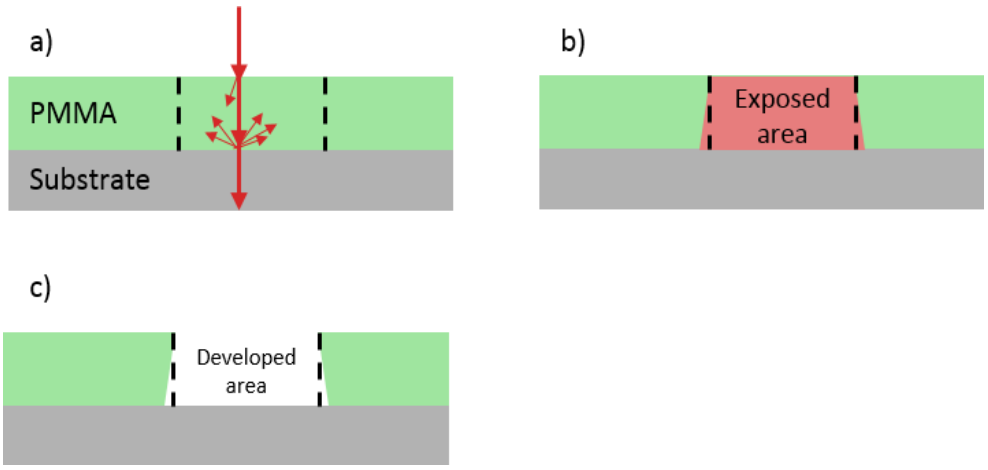

Figure 5.1. Electron-beam exposure schematic a) Forward scattering through small angles, backscattering through large angles, with dashed lines indicating intended feature size. b) Exposed area before development, showing that electron scattering increases feature size and c) exposed areas after development with exaggerated undercut from backscattering at the substrate.

EBL allows realizing small feature sizes with a focused beam of electrons. The EBL patterns were all realized on a 50keV Raith Voyager dedicated EBL system [123], so used accelerated electrons to expose the resist. The de Broglie wavelength λ_{elec} of such high energy electrons is typically less than 10pm [124], and is ~5pm for a 50keV beam. The electrons pass through a uniform circular aperture and waves that pass through such a uniform circular aperture form an Airy diffraction pattern. The first minimum of this Airy pattern occurs at $1.22\lambda_{elec}/NA$ where NA is the numerical aperture in vacuum, $NA = \sin(\theta)$. Therefore, resolution is given by $1.22\lambda_{elec}/NA$ where NA is $2.3\text{x}10^{-3}$ for this system which yields a 2.5nm spot size [125]. Electrons would form a spot of this size on a bare substrate but electrons scatter when they pass through a resist layer on the substrate which limits the actual achievable feature size. The Raith Voyager system is capable of writing ~7nm features [123], the size of which is not limited by the electron spot size but by the scattering in the resist. Making the resist layer thinner increases the smallest achievable feature size for a given resist because it limits the electron dispersion after scattering at vacuum/resist and resist/substrate interfaces.

The electrons are emitted from a field-emission gun, focused through a series of magnetic lenses and are then incident on a resist layer. The resist to define the pattern is poly(methyl-methacrylate), (495 PMMA A6, Microchem). The incident electrons scatter through the PMMA resist and cause the polymer chain to break; the shorter polymer chains are then more soluble in a developer [124]. The exposed areas that dissolve in developer class PMMA as a positive resist; negative resists are also available, for which exposed areas become insoluble while the un-exposed areas dissolve.

Electrons incident on the sample break the polymer chains, but they also scatter within the resist layer(s) and at material interfaces. As shown in figure 5.1, electrons scatter through both small and large angles, which creates an effective spot size in the resist layer which is larger than the spot size in vacuum. These scattering considerations combine to enlarge features and limit the resolution of the pattern [126].

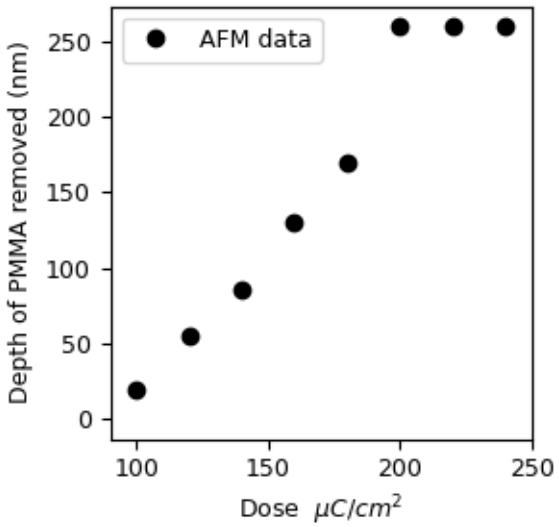

Figure 5.2. Depth of PMMA removed plotted against charge dose.

The charge per unit area of the exposure, or exposure dose, is a crucial parameter in EBL. While over-dosing can result in larger features than designed, under-dosing can result in insufficient resist removed during development, leaving resist on the substrate and thereby preventing successful lift-off, as described in more detail below. Therefore, it is important to check that all resist has been removed in the patterned areas. I verified this by exposing a series of 1µm lines in 250nm thick PMMA spin-coated on silicon at 5,000 rpm for 60s. These patterns, and all further patterns were developed for 120 seconds with a developer solution of 3 parts DI water to 7 parts isopropanol, so that the fabricated feature size is tuned with charge dose and scaling the intended feature size in the design. Figure 5.2 shows the depth of these lines post-development. A 200µC/cm^2 dose is typically sufficient to remove all PMMA. To allow for variation in resist quality, thickness and substrate charge dissipation between samples, a more conservative value of 300 µC/cm^2 was selected as the standard exposure dose. This dose guarantees removal of all of the exposed resist at the cost of approximately 5% larger features.

5.1.1 Bi-layer lift-off process for 1D periodic MIM array

Having established a method for creating sub-wavelength patterns in a PMMA resist layer, the patterns are transferred to metal features on the substrate by a process called lift-off. In the lift-off process, the PMMA layer acts as a mask during metal deposition. Post-deposition, the resist is dissolved, lifting-off the unwanted metal around the desired features. For the resist layer to be accessible by the developer, there must be a discontinuity between the metal deposited on the resist and the metal deposited on the substrate. One way to achieve this discontinuity is with a bi-layer lift-off process, described in this section.

The two layers in the bi-layer lift-off process serve separate purposes. The top-most layer, PMMA, provides the pattern and resolution for the desired metal features. The second resist layer (Lift Off Resist, or LOR) provides an undercut relative to the top layer to ensure the discontinuity between metal excess on the resist and metal features on the substrate, shown schematically in figure 5.3. The lift-off steps used here were inspired by previous work [127] in which the top-most layer is developed first, leaving the second layer unmodified. The LOR layer is not sensitive to electrons at all and is dissolved with a separate developer (1:1 MF319:DI water) once the PMMA development has finished. The undercut length is tuned independently of the PMMA development by the length of time for which the sample is in LOR developer.

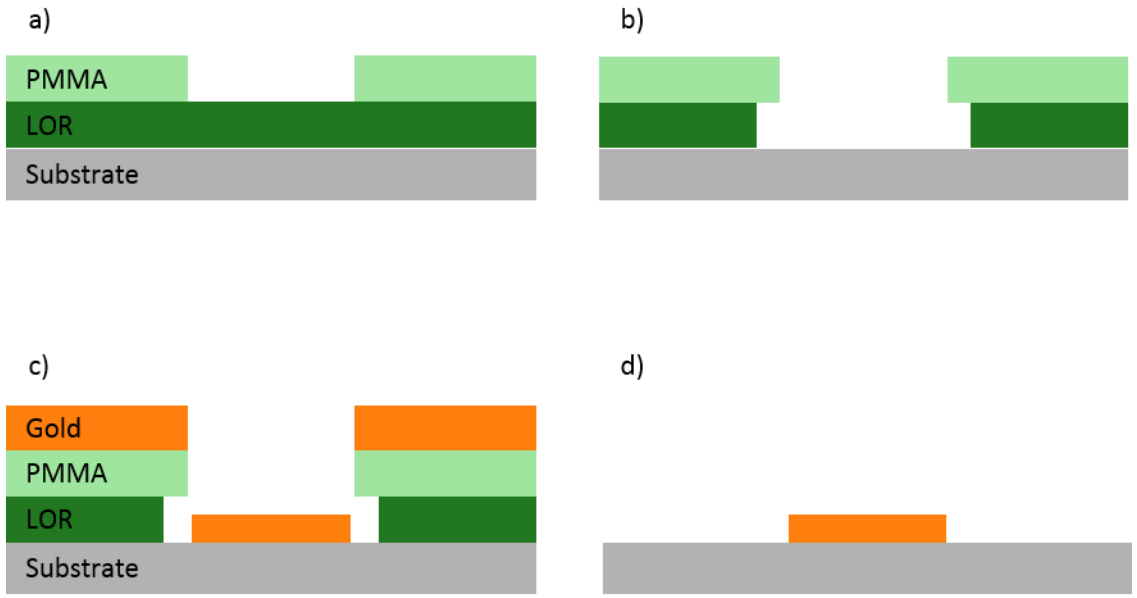

Figure 5.3. Schematic of a bi-layer lift off process showing each key step: a) resist layers with PMMA exposed and developed, b) undercut LOR, c) Gold evaporation onto the bilayer resist stack then d) the final fabricated metal feature.

The undercut layer first used was a dilute solution containing Lift Off Resist (LOR) 7B (MichroChem). The LOR was diluted with cyclopentanone in a 2:1 ratio so that it would spin-coat to form a 200-300 nm thin layer on the substrate; as explained above, the thinner the resist, the higher the resolution of the EBL process, while a thicker layer facilitates lift-off of the metal, and a few 100 nm total thickness of resist layers are seen as a good trade-off [127].

The LOR solution was then spin-coated onto the substrate to form a flat, homogeneous layer. The sample was spun at 5,000 rpm for 60 seconds. Spinning at a relatively high speed aids consistency between samples, since the resist thickness/spin speed curve gradient is lower for higher spin speeds than for lower (eg 1,000 rpm) spin speeds, so variation in spin speed causes a smaller change in resist thickness. Following spin-coating, the sample is baked for 5 minutes at 180°C in air on a hotplate to evaporate excess solvent and harden the spin-coated resist layer. The LOR layer thickness was measured to be 250nm by ellipsometry.

Undiluted 495 PMMA A6 was spin-coated onto the substrate at 5,000 rpm and baked for 5 minutes at 180°C in air which resulted in a thickness of 260nm measured via ellipsometry and AFM (figure 5.2). The design was written onto the PMMA layer system using the mid mid-current 30µm column mode and a charge dose of 300 $\mu C/cm^2$.

The undercut length is the distance from the edge of the PMMA feature to the remaining LOR underneath the PMMA. MF319 developer solution dissolves the LOR resist layer over time. The time the sample spends in developer solution controls the undercut length. The undercut length in LOR is inferred by placing PMMA squares on top of the LOR layer. The squares of PMMA are only attached to the substrate by the LOR underneath them. If the LOR underneath a PMMA square dissolves then the PMMA square detaches from the substrate and floats away in the developer solution. In other words, when the PMMA square has been fully undercut then the PMMA square is removed from the sample.

The PMMA square is removed when the undercut length is half the length of the PMMA square side because the LOR is dissolved from both sides underneath the square. A PMMA square with longer sides requires more time to fully undercut from the substrate because the longer-sided PMMA square has more LOR underneath it, which takes more time to dissolve.

Removing a grid of PMMA squares causes an observable difference under an optical microscope, as is evident between the left three squares in figure 5.4a where the left three squares are present, and figure 5.4 b where the squares are absent.

I designed, exposed and developed a pattern of different sized PMMA squares (250nm thick) on LOR (300nm thick). This sample was placed in LOR developer (1:1 MF319:DI water) for 30 seconds, then examined under the optical microscope. The before and after images are shown in figure 5.4 a and b respectively. After 30 seconds in LOR developer, the 600nm squares (middle in in figure 5.4 a and b) have been removed and the 800nm squares are still present, indicating that the undercut length is between 300nm and 400nm as labelled in the photograph.

a)

b)

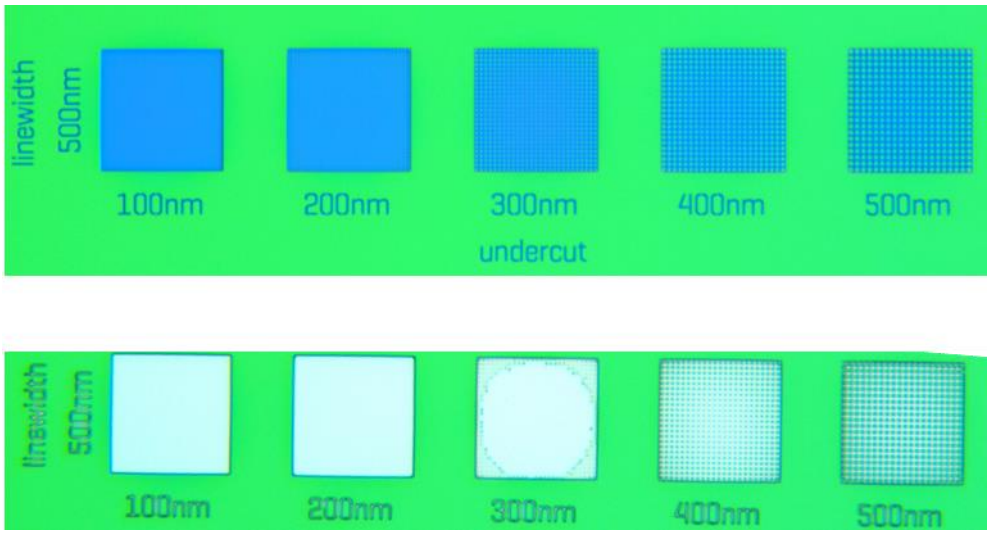

Figure 5.4. Example undercut test pattern a) before and b) after 30 seconds undercut in 1:1 DI water: MF319.

Using an undercut layer introduced some complications and limitations. Firstly, the undercut step would not remove all of the LOR between the exposed PMMA feature and the substrate if the undercut layer is too thick. This remaining LOR blocks the metal from being deposited onto the substrate, so is completely removed in the lift-off step when all of the LOR is dissolved.

Secondly, the undercut length limits the density of exposed features. If features are too close together, then the LOR between them is too thin and will be completely removed in the undercut step. This LOR supports the PMMA layer so removing it also removes the PMMA on top of it. The PMMA layer provides the distinct patterned features so removing it also removes the pattern. The result is that individual features lose their separation and form one larger metal strip, shown in figure 5.5a.

a) b)

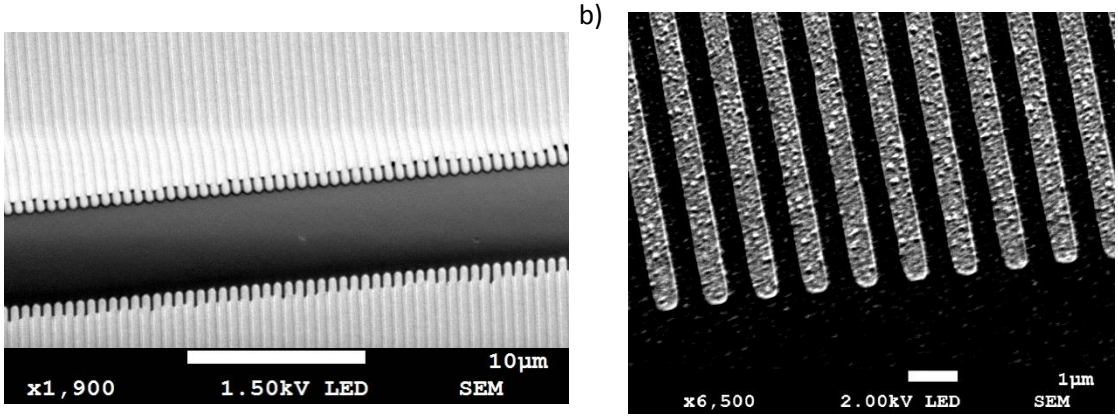

Figure 5.5. Example SEM micrograph of a) failed and b) successful lift-off features. a) Metal features lose separation because the undercut layer between PMMA (250nm thick) dissolved so PMMA detaches from the sample. b) Distinct lift-off features from successful lift-off by using 150nm thick LOR

I then decided to use a thinner layer of LOR to avoid these undercut issues. The LOR was diluted with equal parts cyclopentanone by mass, spun at 5,000 rpm and baked at 180°C for 5 minutes. The thinner LOR layer was 150nm thick. The undercut developer was also diluted to 1 part MF319 and 3 parts DI water to slow down removal and afford greater control over the undercut rate. The undercut time was increased to two minutes to achieve a 100nm undercut.

A series of 1D periodic arrays of metal features was fabricated by following the above process on a substrate of 20nm sputtered silica on 150nm template stripped gold. Further detail of these deposition processes is given in chapter 3. The metal features were realized by first depositing 1nm of titanium for adhesion, then 20nm of gold by e-beam evaporation onto the developed and undercut resist layers.

Following the metal deposition, the resist layers were dissolved in a glass beaker of 1165 (Microposit® Remover), with regular stirring. The resist layers dissolved after approximately 20 minutes and flakes of metal could be seen floating in the beaker. Lifting the sample out of the beaker risks dragging it through these metal lakes, which would stick to the sample surface and obscure the designed MIM

fingers. Instead, I fill the beaker with DI water, pour out the excess liquid and repeat these steps three to four times. The overflowing liquid carried most of the metal flakes away, reducing the risk of destroying the sample by dragging it through these metal flakes. The safely extracted MIM sample was then rinsed in acetone and IPA to remove any residue left by the 1165 stripper solution.

The steps which resulted in successfully fabricated bi-layer lift-off features are summarised here:

- Spin-coat 1:1 LOR:cyclopentanone at 5,000rpm for 60s and bake at 180°C on a hotplate in air;
- Spin-coat 495 PMMA A6 at 5,000rpm and bake at 180°C on a hotplate in air for 5 minutes;
- Expose pattern using the mid mid-current 30µm column mode on the Raith Voyager system with a charge dose of 300 µC/cm^2;
- Develop the sample in a solution of 3 parts DI water to 7 parts isopropanol for 120 seconds to develop the PMMA pattern;
- Develop the sample in a solution of 1 part MF319 and 3 parts DI for 120 seconds to achieve a 100nm undercut in the LOR layer.

5.1.2 Bi-layer process characterization

The MIM fingers were examined with an SEM to determine the relationship between their designed feature size and measured feature size. Figure 5.6 shows an example micrograph of these MIM fingers and the difference between their designed and measured width. The measured finger width is

a) b)

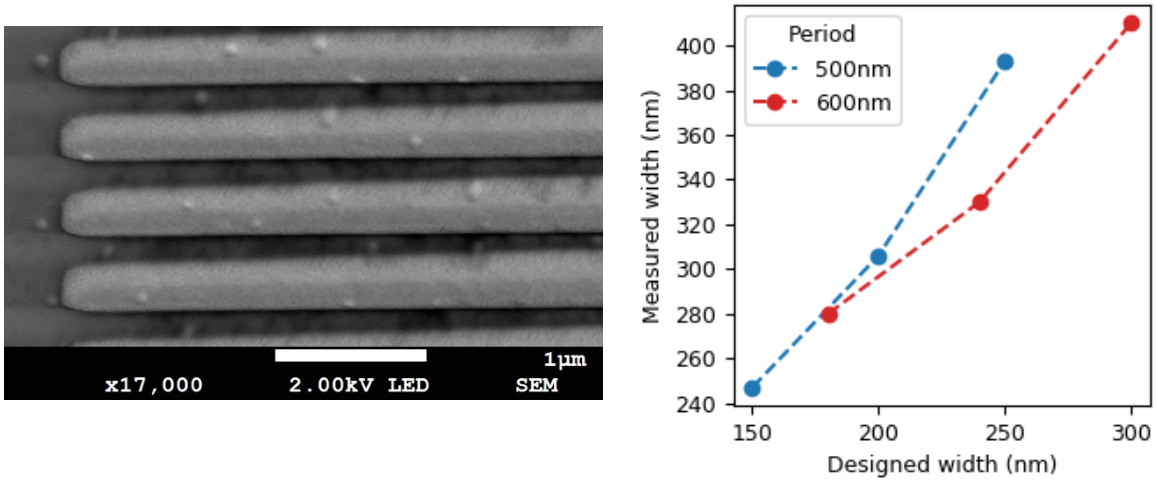

Figure 5.6. SEM micrograph of 1D periodic MIM structures. a) Example micrograph of 400nm wide MIM structures b) Measured width against designed width for 500nm and 600nm periodic arrays, showing slight overexposure.

larger than the design width, which is expected due to the higher dose than necessary having been selected for the PMMA exposure (figure 5.2). The fingers fabricated with a 500nm period show a proportionally larger increase than their 600nm periodic counterparts. This greater increase is due to the proximity effect; the 500nm periodic features are more closely spaced, so receive a higher proportion of their neighbours' charge dose than the 600nm periodic features [128]. This long-range (~100nm) feature broadening is not due to the primary incident electrons, but secondary electrons which are knocked out of atoms by primary electrons which have back-scattered at the resist-substrate interface [129]. This effectively higher charge dose results in the larger features shown in figure 5.6.

The bi-layer lift-off process described above, combined with the template-stripping and sputtering described in chapter 3 realize MIM "fingers" that are periodic in one dimension and 12 µm long in the other dimension, as shown in figure 5.5b. In the lithography step, arrays of resonators with both different periods and different fill factors were exposed so that the effect of these parameters on the optical response could be compared.

Figure 5.7 shows the optical data for two different periods and three different fill factors measured in air. In figure 5.7 a, there are two distinct dips particularly for fill factors of 40% and 50%. When the fill factor is varied, the dip at 700nm-800nm shifts more than the peak at approximately 600nm. This greater shift in wavelength indicates that these peaks correspond to the MIM resonance, because they depend on feature size. Conversely, when the period is increased from 500nm in figure 5.7a to

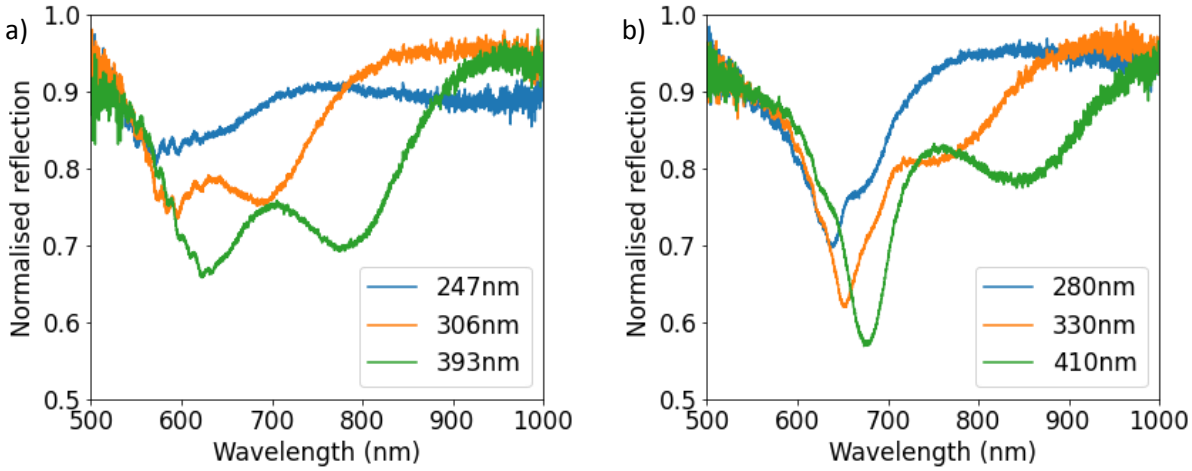

Figure 5.7 Resonant response of fabricated 1D MIM structures measured in air with periods a) 500nm and b) 600nm and different metal feature widths, given in the figure legend.

600nm in figure 5.7b, the lower wavelength resonance dip shifts from approximately 600nm to approximately 700nm, indicating that this dip depends on the period of the array. So we can clearly distinguish two separate types of resonances, i.e. the localized MIM resonance and the distributed surface plasmon resonance, the former depending more strongly on resonator width and the latter more strongly on period.

These wavelength and period dependencies are in qualitative agreement with the simulation results in chapter 4 and make it possible to determine the physical origin of each dip in the spectrum. It should be noted that these structures were measured in air (background index = 1), while all simulations took place in water (background index=1.33). The effect of reducing the background index from 1.33 to 1 is to blue-shift the SPP peak (to 600nm-700nm) because it is highly sensitive to changes in its bulk surroundings and the surrounding index decreased by 0.33 so the optical path between metal features decreased, so the SPP resonance wavelength decreased. Correspondingly, the width sweep of the metal feature includes values up to ~400nm, larger than any simulated value, which red-shifts the MIM peak to the 700nm-900nm region of the spectrum. Therefore, the SPP peak in figure 5.7 appears at shorter wavelengths than the MIM peak, which is the opposite of the simulated spectra.

5.1.3 Single layer lift-off process for 2D periodic MIM array

Now that the MIM resonance has been successfully observed, I shift focus onto fabricating MIM resonators with high surface sensitivity. The simulation results in chapter 4 suggest that resonators with sharp corners will have higher surface sensitivity than resonators with rounded corners as in figure 5.6; rounded corners being an inevitable consequence of the fabrication process. The undercut layer discussed in section 5.1.1 was used at first to ensure discontinuity between metal features on the substrate and excess metal on top of the resist layer. In the next fabrication design iteration, this caution was abandoned and a single-layer resist stack was used instead to achieve sharper features.

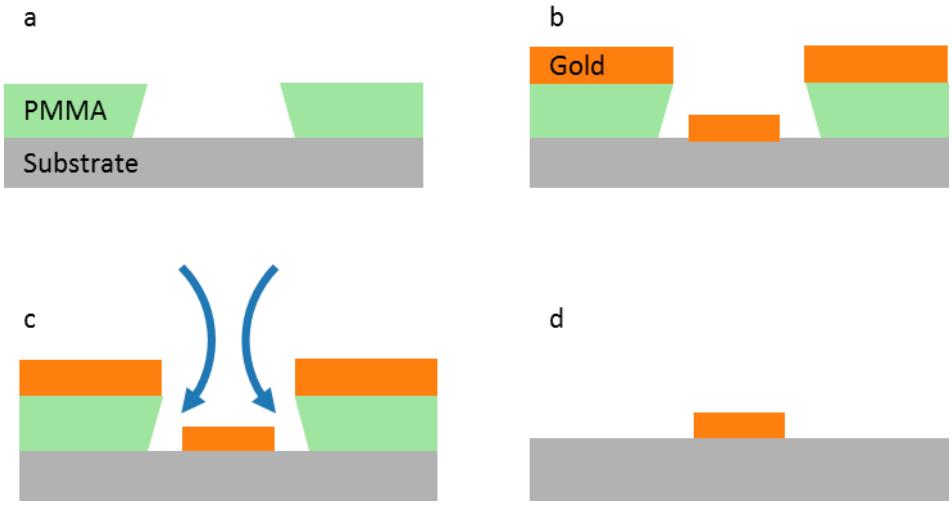

Figure 5.8. Schematic of a single layer lift-off process in order a), b) c) d). a) Exposed and developed PMMA showing exaggerated undercut. b) Evaporated gold layer on the exposed PMMA layer with discontinuity between gold on PMMA and gold on substrate. c) the acess that a developer has to the PMMA layer and d) the final gold feature.

Figure 5.8 is a schematic of the single layer lift-off process. In contrast to figure 5.3, only one resist layer (PMMA) is used. As in figure 5.1, the slight undercut which results from scattered electrons is exaggerated for clarity. It is this undercut which provides the discontinuity to ensure lift-off in a single-layer lift-off process. Even though this undercut is small, the metal layer which will be deposited is also relatively thin (≈20 nm); the rule of thumb is that the resist should be at least three times thicker than the metal layer, which condition is met here.

Once the features are exposed and developed in PMMA, the next stage of the process is the metal deposition; we use electron-beam evaporation, discussed in chapter 3. A consideration is the time that the sample spends in the 1165 stripper solution. Ideally, the sample would be left for hours in the stripper solution so that all the PMMA can be dissolved. However, the Norland optical adhesive used in template stripping is also dissolved by the stripper solution, albeit slower than the PMMA. When a sample is left in the solution for too long, the Norland optical adhesive dissolves and completely destroys the nanostructures (figure 5.9a). There is, however, a compromise. By carefully watching and gently agitating the sample, the lift-off process can be accelerated and the sample can be lifted out of the stripper solution before the damage to the Norland layer destroys the nanostructures. This compromise is shown in figure 5.9b, where the sample includes arrays of MIM nanostructures and some damage to the Norland layer at the edges.

a) b)

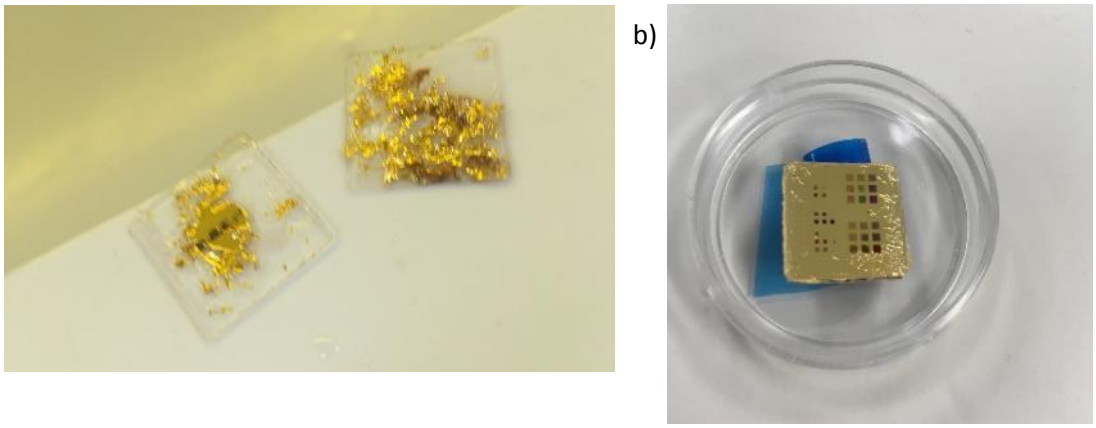

Figure 5.9. Damage to Norland optical adhesive layer from 1165 stripper solution. a) A sample left in stripper solution for too long and b) a sample left in stripper solution for a shorter time, resulting successful lift-off but still showing some damage at the substrate edges.

5.1.4 Fabricated single layer lift-off 2D periodic MIM resonators

Finally, arrays of 2D periodic MIM resonators were successfully fabricated using the single layer process. The successfully fabricated 2D MIM structures are shown in figure 5.10. When compared with the structures fabricated by a bilayer lift-off process (figure 5.6), these structures show sharper edges and corners.

The SEM micrograph taken with the sample tilted at 45° shows a potential limitation of the lift-off process, however. Some excess metal remains attached to the sides of the metal features. While the MIM resonance dip is still evident (figure 5.12), the excess metal that remains attached to the top metal features may soften the MIM response. In particular, such fine features may act as scattering centres and broaden the resonance, or they may change the size of individual resonators and heterogeneously broaden the response of the array.

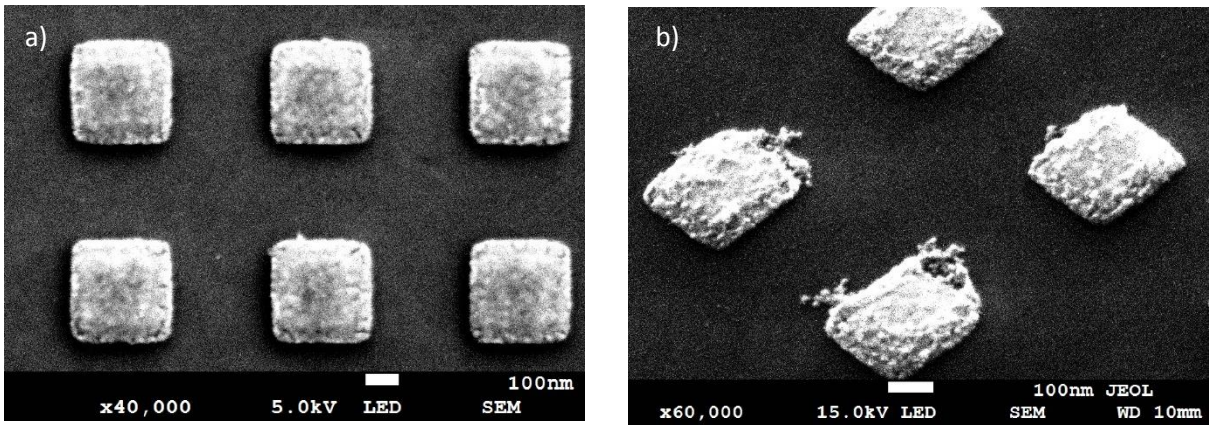

Figure 5.10. SEM micrograph of fabricated 2D structures with viewing angles of a) 0° and b) 45°. The little wires in b) are thin excess metal from the lift-off process and only show up when viewing the sample at an angle in the SEM due to electron penetration depth.

Another observation is the surface roughness. Again, this roughness is more evident when the sample is examined at an angle relative to the incident beam of electrons in the SEM. The individual metal squares in figure 5.10b show small bumps on the top face and the sides. This surface roughness is better examined using AFM in figure 5.11 which confirms that the top side of the MIM square is rougher than the sputtered silica surface upon which it rests. The AFM image also shows the sides of the square are slightly sloped, which affects the E field distribution at the edges.

As previously discussed for the 1D lift-off features, the 2D lift-off features also show a discrepancy between their designed and fabricated width. This comparison is shown in figure 5.11b. Here, the different periods of the MIM arrays cause little effect in feature size, unlike in the 1D case of figure 5.6b. The reduced period dependence in figure 5.11b is due to the lower surface coverage of the squares compared to the fingers of figure 5.6b. The reduced surface coverage reduces the amount of secondary electrons produced per unit area within an array of features. Fewer secondary electrons per unit area which overlap with adjacent designed features means 2D features ultimately receive a lower charge dose than 1D features.

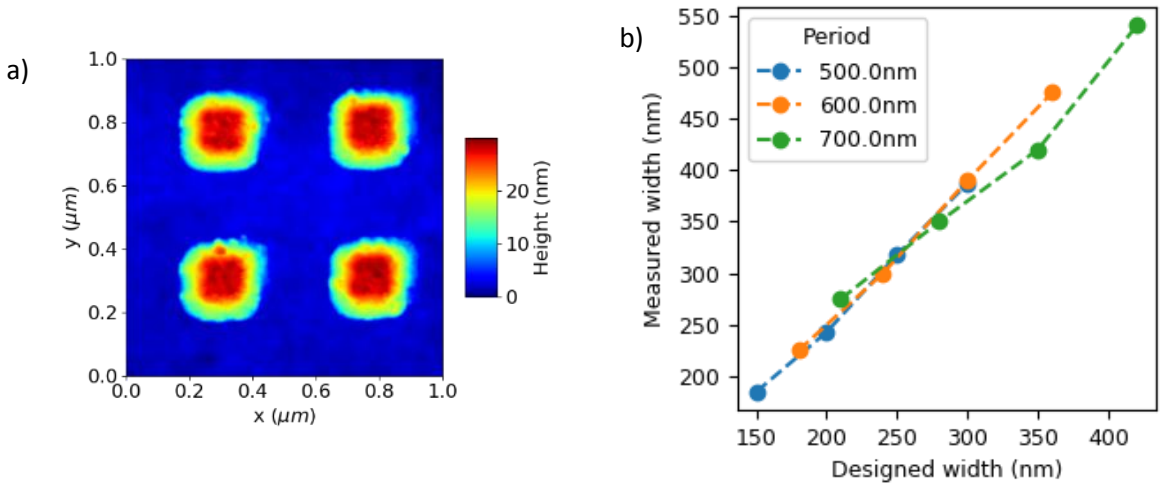

Figure 5.11. Width and roughness characterisation of 2D metal features. a) AFM image of individual MIM resonators. b) Measured width vs intended width for 2D resonators fabricated with the single-layer lift-off process.

For completeness, the full fabrication process for the 2D resonators that were used to obtain sensing results is stated here, and is the same as in ref [36]:

- The base plane is fabricated by template stripping [130] using 150nm of gold deposited by electron beam evaporation onto an atomically flat silicon wafer;
- The 20 nm thick SiO_2 insulator layer is deposited using a bespoke pulsed-DC magnetron sputterer (100 W, 2.9 µS, 120 kHz, gas flow 17.5 SCCM Ar, 10 SCCM O_2);
- A single 250nm thick PMMA layer is spun at 5,000 rpm and baked at 180°C on a hotplate in air;
- The PMMA is patterned with the 50 keV Raith Voyager, using a dose 300 µC/cm^2;
- The exposed pattern is developed in 3:7 DI water : isopropanol for 120 seconds;

- 20nm of gold is evaporated (MBraun electron-beam evaporator); then
- PMMA is lifted off in 1165 stripper solution for approximately 15 minutes.

Structures fabricated by the above process are shown in figure 5.10 and figure 5.11b.

As a result, I was able to observe nice MIM resonances shown in figure 5.12 where two different types of dips are observed. The dip at shorter wavelength shifts when the fill factor (resonator width) is varied while the other stays approximately constant. Both figures show a constant dip at 850nm for a period of 600nm and dips that shift in the wavelength region of 650nm to 750nm when the resonator width is varied. The shoulder to the 850nm dip is likely due to off-angle illumination, causing another dip to emerge at 825nm. This new peak emerging is consistent with the 850nm dip splitting into two dips at approximately 0.5° angle in figure 4.5a.

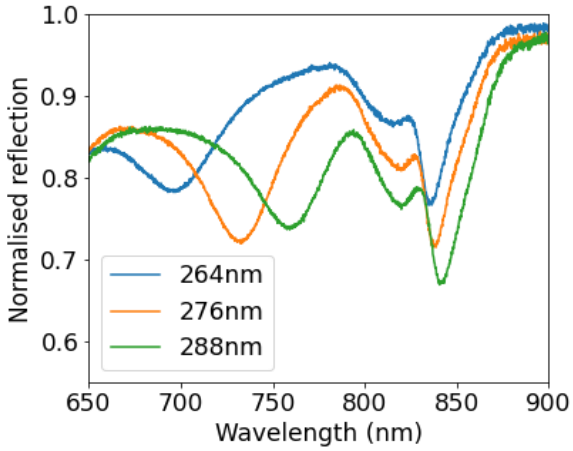

Figure 5.12. Resonance characterization data for 2D periodic MIM squares fabricated using the single-layer lift-off process. The dips around ~700nm show a strong dependence on width/fill factor but the dips at 850nm remain in approximately the same position.

5.2 Sensing

Measuring the resonance wavelength shift requires accurately tracking the resonance dip wavelength position. One method of tracking these dip positions is to fit curves to features in the spectrum. Figure 5.13 shows example curve fits used to track the two peaks in the spectrum and obtain the sensing results which follow. The MIM peak can be identified at 750nm and the SPP peak at 850nm form their dependence on width and period, respectively. Both resonance dips show asymmetry and they affect one another by their anti-crossing behaviour discussed in chapter 4. In order to account for this asymmetry, I fit an asymmetric Fano profile to both peaks which appears similar to the Lorentzian line shape but also provides a more accurate curve fit by accounting for the asymmetry exhibited by both peaks. The fits here are shown with solid curves and the data range used to generate the fit is shown with dashed lines.

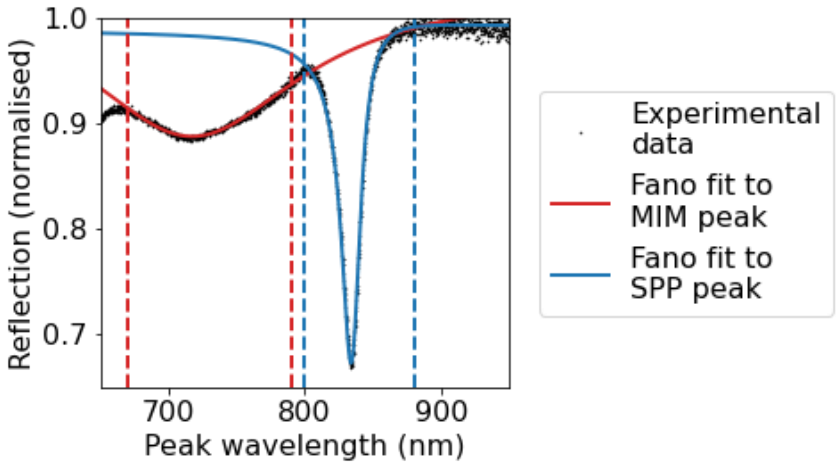

Figure 5.13. Reflectance response measured from an array of MIM resonators. Curve fits to the MIM and SPP peak are shown. Dashed lines indicate the data range used for each curve fit.

5.2.1 MIM mode, bulk sensitivity and limit of detection

Bulk sensitivity is a widely-used parameter to characterize refractive index sensor performance; it describes the system response to the change in refractive index in the bulk space above the sensor [9], [58], [62], [72]. Here, I measure the peak wavelength shift in nanometers so bulk sensitivity is quantified in units of nm/RIU where nm denotes nanometres and RIU stands for refractive index unit.

The bulk refractive index above the sensor chip is varied by flowing aqueous solutions of salt (sodium chloride) over the sensor surface, encased in the microfluidic flow cell detailed in chapter 3. Salt concentrations of approximately 50mg/ml, 100mg/ml and 150mg/ml sodium chloride were prepared and pumped through the fluidic channel which provide refractive index shifts of approximately 0.01

RIU between concentrations. The refractive index of the different solutions was measured using a Brix RI-Check digital refractometer.

DI water was used as buffer and pumped through the flow cell using a syringe pump. Different salt solutions were introduced into the flow system using a sample loop, which is a valve mechanism that allows fluid to be introduced without changing syringes in the pump, it avoids bubbles and keeps a constant flow of buffer over the sensor. The pump flow rate was set to 50µl/min. Salt solutions were loaded into approximately 1ml of tubing in the sample loop then injected into the flow cell by turning the sample loop valve. Approximately 40 minutes was left between introducing a new sample solution to the flow cell to allow 20 minutes for the 1ml sample to flow over the channel and 20 minutes for the peak wavelength to return to 0, confirming that the sensor is clean.

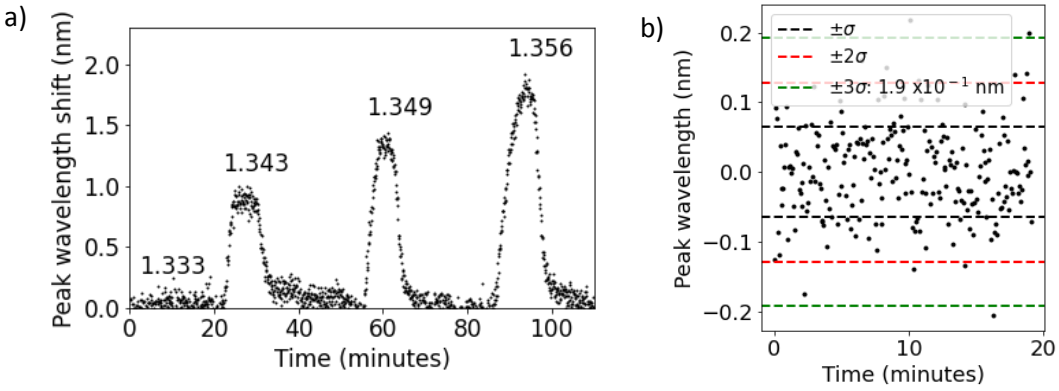

Figure 5.14. Lithography MIM bulk sensitivity results. a) Peak wavelength shift over time and b) Variation of the resonance wavelength as a function of time, measured in the first 20 minutes of the experiment. This measurement is used to determine the noise floor.

While flowing the different concentrations of sodium chloride solution over the surface of the sensor, the reflectance spectrum is recorded at 5 second intervals to monitor changes in the resonance wavelength. The reflection spectrum at a blank area of the chip was taken for reference to allow normalization.

Figure 5.14a shows the peak wavelength shift for different salt concentrations; the bulk sensitivity is calculated as 78±3nm/RIU. The noise limit is determined from data taken for constant refractive index over 20 mins as shown in figure 5.14b. The dashed black, red and green lines indicate ±σ, ±2σ and ±3σ respectively and 3σ is measured to be 0.19nm. The limit of detection (LOD)is the minimum amount of analyte that the sensor can detect and is calculated by dividing the 3 sigma value by the sensitivity [62]. Using this method, I determine the LOD as 2.4×10^{-3} RIU. The MIM mode's high limit of detection

is in part due to its relatively low 78nm/RIU bulk sensitivity. Other limiting factors are the dip features: the relatively large FWHM (~50nm) and low extinction ratio (5%) which contribute to the 3σ noise value. I assess these limiting factors by comparing MIM dip noise floor to the sharper SPP dip noise floor in the following section.

The 78±3nm/RIU bulk sensitivity is similar to the bulk refractive index of cuboid-shaped nanoparticles [61] and below other plasmonic methods such as gold nanohole arrays (~700nm/RIU) [64] and SPR (2500nm/RIU) [63], [67]. The 2.4x10^{-3} RIU LOD achieved here with a spectrometer is comparable to the 4x10^{-3} RIU achieved by probing the resonance condition of gold nanoholes with an LED and CCD [76]. On bulk sensitivity alone, these MIM structures are not competitive with other techniques found in the literature. In order to make a more thorough comparison, surface sensitivity Is measured below in section 5.2.3.

5.2.2 Surface Plasmon mode, bulk sensitivity and limit of detection

It is interesting to compare the two modes shown in Figure 5.13, i.e. the MIM mode and the surface plasmon mode. The latter is discussed next, again, both in terms of sensitivity and in terms of LOD. Figure 5.15 shows the peak wavelength when flowing different salt concentration solutions over the sensor surface. These measurements were taken at the same time as the MIM measurements in figure 5.14 and obtained by fitting Fano curves to the SPP peak as explained above.

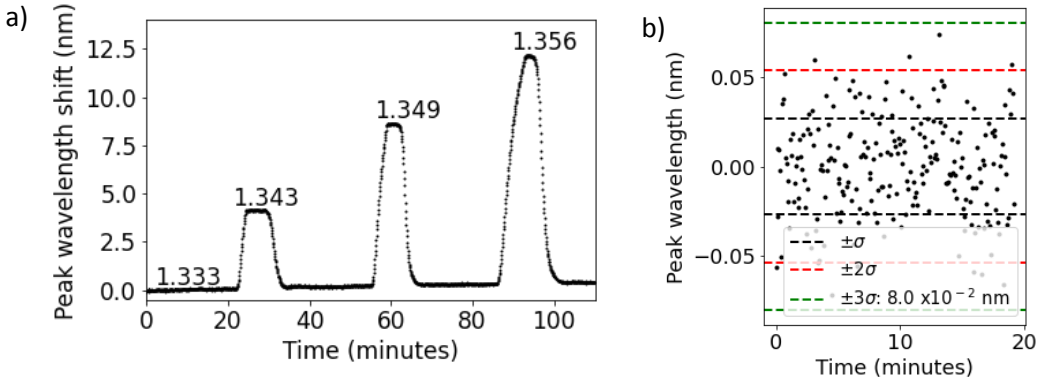

Figure 5.15. SPP bulk sensitivity results a) Changing solution concentration over time. b) Resonance wavelength (centred about the mean) over time, measured in the first 20 minutes of the experiment while flowing DI water for the SPP system

The SPP peak shows differences to the MIM peak. Even by eye, the SPP peak wavelength shifts are larger for the same salt concentration. Correspondingly, the limit of detection for the SPP mode is 1.5x10^{-4} RIU due to both its higher bulk sensitivity (540±40nm/RIU) and lower 3σ noise value

(0.08nm). This 3σ value is less than half that of the MIM mode due to the SPP dip's larger extinction ratio (40%) and smaller FWHM (10nm). This comparison supports the above hypothesis that the extinction ratio and FWHM are parameters worth of attention in order to decrease a mode's limit of detection. This bulk sensitivity (540±40nm/RIU) value surpasses the bulk sensitivity of gold nanoparticles [61] and is similar to gold nanohole arrays (~700nm/RIU) [64]. It does not break into the 10^3nm/RIU bulk sensitivity regime unlike some more complex 2D periodic gold/insulator patterned structures found in the literature [69].

5.2.3 Surface sensitivity

While bulk sensitivity provides some indication of a sensor's performance and is relatively easy to measure, it does not represent protein binding events occurring at the sensor surface very well. Recall that the purpose of such sensors is to detect protein binding, not to determine bulk refractive index changes. These binding events can be modelled by changing the refractive index in a 10nm layer above the sensor surface since the biomolecules are only of order ~10nm in length [56], [66]. In order to achieve a quantifiable and reproducible comparison, I sputter a 10nm layer of silica onto the surface of the sensor and measure the resulting peak wavelength shift, immersing the surface in water to best represent the real scenario of protein binding.

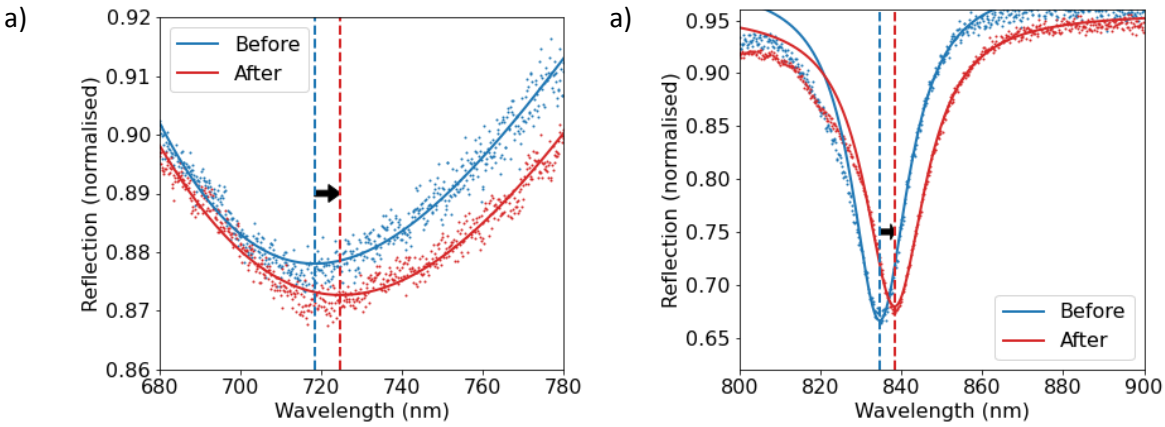

Figure 5.16. MIM and SPP resonance surface sensitivity. Peak wavelength shifts due to changing refractive index in a 10nm layer above the sensor surface for (a) the MIM peak (6.5nm) and (b) the SPP peak (3.7nm)

Figure 5.16 shows the peak wavelength shifts before and after sputtering a 10nm layer of silica onto the sensor surface. The large mode overlap between the MIM mode and 10nm silica layer causes the MIM peak wavelength to shift by as much as 6.5nm. Taking the RI of DI water as 1.33 and sputtered silica as 1.45, the RI change is 0.12, which yields a surface sensitivity of 54±15nm/RIU. The previously

mentioned large FWHM and low extinction ratio contribute to the relatively high ~25% uncertainty for this sensitivity value, estimated from the dip wavelength uncertainty from the curve fitting procedure. This value is not far from the MIM mode bulk sensitivity (78±3nm/RIU) which indicates that most of the evanescent field does not extend past 10nm of the resonator.

By contrast, the extended SPP mode has a much lower overlap with the 10 nm layer since it extends much further into the analyte layer, resulting in a surface sensitivity of only 3.6 nm for the same layer or 30nm/RIU. The strong confinement of the MIM mode turns into a real advantage - almost all of the evanescent field overlaps with the 10 nm layer. I estimate 85% of the evanescent field overlaps with analyte within 10nm of the resonator surface using the overlap integral and example estimate in section 2.5.1.

Given the emphasis on protein binding, the limit of detection at the surface is more appropriate than the bulk limit of detection to characterize the performance of these resonances for sensing. Substituting the bulk sensitivity values for surface sensitivity values but using the same estimate for the system resolution, I calculate limits of detection to be $4x10^{-3}$ RIU for the MIM peak and $3x10^{-3}$ RIU for the SPP peak. The MIM and SPP peaks are now much more comparable when the emphasis is put on surface sensitivity over bulk sensitivity.

5.3 Lithography results conclusions

I have shown that metal-insulator metal (MIM) modes have a significantly higher surface sensitivity than other sensing modalities based on the tight confinement they offer. I note that surface sensitivity is the key figure of merit for biomolecular applications because surface-bound molecules are typically located within 5-10 nm of the sensor surface. Importantly, I show that surface sensitivity is not directly related to bulk sensitivity, which is the quantity usually measured. In particular, I show a surface sensitivity of 54nm/RIU for the particular MIM mode considered here while we only measure 30nm/RIU for the SPR mode in the same structure. Conversely, the SPR mode exhibits a bulk sensitivity of 540nm/RIU, while the MIM mode only shows 78nm/RIU.

The effective index of the MIM mode studied here broadly agrees with the simulations in chapter 4, but the depth of the resonance dip does not. The small resonance dip depth may be explained by considering the metal-insulator interfaces which form the structure. Firstly, the titanium adhesion layer limits the resonance depth since its plasmonic properties are inferior to those of gold. Secondly, both interfaces have roughness arising from the grain boundaries in polycrystalline films on either

side of the silica layer which decrease the lifetime of plasmons in these MIM cavities [116]. Both these concerns may be addressed by investigating bottom-up fabrication methods which provide crystalline metal films and non-absorbing adhesion layers presented in chapter 8.

The sensitivity of the MIM mode may be improved through design considerations. Firstly, chapter 4 identifies the MIM high surface sensitivity as arising from the top metal feature corners where the E field is localised. The quality of these corners relies on a sharply defined corner in the PMMA patterning layer which is difficult to reliably produce with EBL. This PMMA layer can be damaged by excessive heating during metal evaporation, a necessary step for the gold lift-off.

There is a more fundamental consideration regarding the MIM mode sensitivity. The first order resonance increases mode overlap with the analyte, which further increases the device's sensitivity. This first order MIM mode requires resonator sizes of order 70-80 nm for the same wavelength window. Such feature sizes are realistic but more difficult to realize reproducibly with e-beam lithography and more accessible via bottom-up fabrication methods.

Chapter 6

MIM resonators based on nanocubes

There is more than one way to realise a MIM resonator. In the last chapter, I presented lithographically fabricated resonators and found their resonance dip depth and sensitivity are limited by fabrication techniques. In order to overcome these limitations, I consider MIM resonators realised by placing nanocubes on a metal-insulator substrate. These nanocube-based MIM resonators offer higher sensitivity by accessing the first order MIM mode. A higher proportion of the first order mode overlaps with its surroundings than the third order mode and this mode overlap is proportional to surface sensitivity, as I demonstrate in this chapter.

These nanocube-based MIM resonators improve the depth of the reflection feature by providing smoother surfaces and combining them with non-absorbing adhesion layers. The smoother metal surfaces are due to the single crystal nanocubes' atomically flat facets. The non-absorbing adhesion layer is an organosilane self-assembled monolayer. The nanocubes are dropcast onto this organic adhesion layer, presented in chapter 7. In order to guide these experiments, I form an expectation of the nanocubes' sensing performance from a computational model presented below.

I represent the dropcast nanocubes' random arrangement on the susbtrate in these simulations by assuming no periodicity or coupling and treating a single, isolated nanocube. Such isolated nanocubes lend themselves well to an eigenmode approach, discussed below.

6.1 Eigenfrequency modelling introduction

There are two main methods for obtaining the resonant frequency of a given nanostructure: a) sweep the frequency and fit a peak to the frequency points (e.g. [94]) , or b) obtain the resonant frequency directly by using an eigenmode solver (e.g. [5]). An eigenvalue approach is more efficient because the computation does not have to be repeated at each frequency in a sweep. The eigenvalue approach also yields a discrete number of resonant modes, which more clearly represents the underlying physics of the system. This eigenmode approach is particularly suited to individual uncoupled resonators such as the nanocubes discussed below. This introductory section provides some of the key principles of the eigenvalue formulation I used and underpins the results shown in the following sections 6.4, 6.5 and 6.6. I refer the interested reader to P. Lalanne's recent work [5]–[7], [65] for a more in-depth discussion.

A photonic system in steady state supports normal modes. These normal modes, in principle, do not experience any damping and their energy does not decay to the outside world. Because of this assumption of energy conservation, the frequency eigenvalue problem is Hermitian (the matrices acting on the electric and magnetic field vectors satisfy $M_{ij} = M^*_{ji}$ where M is a Hermitian matrix) and their eigenvalues are always real, thus can readily be interpreted as the resonance frequencies of the system [131].

A more physically complete description of a given resonator includes its energy losses. Energy can couple from the resonator to the outside world, for example in leaky modes; plasmonic systems, in particular, have energy losses arising from the intrinsic dissipation losses of metals. These material losses can be incorporated into the eigenvalue problem, but this also increases the mathematical complexity. Since energy is no longer conserved, the system is no longer Hermitian and its frequency eigenvalues become complex. How should one interpret a complex frequency?

The complex angular resonant frequency $\tilde{\omega} = \omega_{real} - i\omega_{imag}$ is explained by treating it as we would treat a real frequency and using it to define an oscillation:

$$e^{-i\tilde{\omega}t} = e^{-i(\omega_{real} - i\omega_{imag})t} = e^{-i\omega_{real}t} \times e^{-\omega_{imag}t} \quad (6.1)$$

The real part of the complex frequency is the same frequency as before, i.e the frequency at which the amplitude oscillates. The imaginary part of the frequency is not a frequency in the traditional sense, but it instead describes an exponential envelope in which the mode decays. Since the imaginary part of the complex frequency describes the mode's lifetime, it may be used to calculate

the Q factor: $Q = -\frac{\tilde{\omega}_{real}}{2\tilde{\omega}_{imag}}$ For example, a typical MIM resonator may have a complex frequency of $4.0\text{x}10^{+14}$-$1.5\text{x}10^{+13}$i, yielding a Q factor of approximately 12.

Inside the plasmonic resonator, the mode decays because it is absorbed by the metals and leaks out to its surroundings. In order to overcome this decay, the driving wave must be amplified, ie the –ve sign in front of the imaginary part of the frequency must be changed to +ve in equation (6.1) so that instead of exponentially decreasing over time, the amplitude increases over time. Inside the resonator, this amplification balances the absorption and leakage so the resonance reaches a steady state. Outside the resonator in the far field, this amplified wave diverges exponentially in with the spherical form $\exp\left[-\omega_{imag}\left(t-\frac{r}{c}\right)\right]$ where r is the radial distance from the resonator [6].

For completeness, I include a brief outline of the normalization considerations. The divergence described above and the presence of absorbing materials means that the mode cannot be normalised by energy considerations. The customary **Ẽ·Ẽ*** product derived from energy considerations must be replaced by the **Ẽ·Ẽ** product and the whole field, even regions inside a perfectly matched layer (PML) must be integrated for normalization [65]. The normalization condition then becomes:

$$\iiint_{volume}\left[\widetilde{\boldsymbol{E}}\frac{\partial(\tilde{\omega}\epsilon)}{\partial\tilde{\omega}}\,\widetilde{\boldsymbol{E}}-\widetilde{\boldsymbol{H}}\cdot\frac{\partial(\tilde{\omega}\mu)}{\partial\tilde{\omega}}\widetilde{\boldsymbol{H}}\right]d^3\boldsymbol{r}=1 \tag{6.2}$$

Where the tilde denotes fields which have been normalised using normalisation condition (6.2).These damped modes with complex eigenfrequencies are denoted "*quasi*normal" modes in the literature [5], [6], [8] to distinguish them from normal modes with entirely real eigenfrequencies. Quasinormal modes in plasmonic systems can be solved computationally by the MAN freeware provided by the Light in Complex Nanostructures group, LP2N, Univ. Bordeaux [7]. The MAN freeware is an extension to the COMSOL EMW module via the Weak Form PDE options.

6.2 COMSOL eigenfrequency modelling

The resonant modes' complex eigenfrequencies $\tilde{\omega}_m$ and their field distributions $\tilde{\mathbf{E}}_m$ are calculated from Maxwell's equations, solved by a computer. The eigenfrequency problem is made accessible to a computer by combining analytical expressions discussed in chapter 2 to form two coupled key equations. Recall that the analytical form of the Drude-Lorentz model makes it easy to insert into frequency-domain simulations [3]:

$$\epsilon(\omega) = \epsilon_\infty \left(1 - \frac{\omega_p^2}{\omega^2 - \omega_0^2 - i\gamma\omega}\right), \tag{6.3}$$

where ω_p is the plasma frequency, ω_0 is the resonance frequency, ε_∞ is the permittivity at infinite frequency ω and γ is the damping term. The dispersive material properties are separated from the constant material properties by defining an auxiliary field $\widetilde{\boldsymbol{P}}_m$ [6]:

$$\widetilde{\boldsymbol{P}}_m = -\frac{\omega_p^2}{\widetilde{\omega}_m^2 - \omega_0^2 - i\gamma\widetilde{\omega}_m}\,\widetilde{\boldsymbol{E}}_m, \tag{6.4}$$

which is rearranged to describe the material properties in the first key equation:

$$-\omega_0^2\widetilde{\boldsymbol{P}}_m - i\gamma\widetilde{\omega}_m\widetilde{\boldsymbol{P}}_m + \widetilde{\omega}_m^2\widetilde{\boldsymbol{P}}_m + \omega_p^2\,\widetilde{\boldsymbol{E}}_m = 0. \tag{6.5}$$

The second key equation describes the nature of the electromagnetic fields $\tilde{\boldsymbol{E}}_m$ and is derived from the electric field wave equation [7]:

$$\nabla \times \mu_0^{-1}\nabla \times \widetilde{\boldsymbol{E}}_m = \widetilde{\omega}_m^2\,\epsilon(\boldsymbol{r},\omega)\;\widetilde{\boldsymbol{E}}_m \tag{6.6}$$

where $\tilde{\omega}_m$ are the eigenfrequencies and $\tilde{\boldsymbol{E}}_m$ are corresponding electric fields, both labelled by the mode index m. The permittivity distribution $\varepsilon(r, \omega)$ in expression (6.6) includes both its position and frequency dependency. The frequency dependency is described by the Drude dispersion relation (6.3) so is substituted into the wave equation (6.6) with the auxiliary field (6.4) to form the second key equation:

$$\nabla \times \mu_0^{-1}\nabla \times \widetilde{\boldsymbol{E}}_m - \widetilde{\omega}_m^2\widetilde{\boldsymbol{E}}_m - \widetilde{\omega}_m^2\epsilon_\infty\widetilde{\boldsymbol{P}}_m = 0 \tag{6.7}$$

Equations the form (6.5) and (6.7) with eigenvectors $[\widetilde{\boldsymbol{E}}_m, \widetilde{\boldsymbol{P}}_m]$ define a quadratic polynomial eigenproblem in equation (6.8) below:

$$\boldsymbol{K}\begin{bmatrix}\widetilde{\boldsymbol{E}}_m \\ \widetilde{\boldsymbol{P}}_m\end{bmatrix} + \widetilde{\omega}_m\mathbf{C}\begin{bmatrix}\widetilde{\boldsymbol{E}}_m \\ \widetilde{\boldsymbol{P}}_m\end{bmatrix} + \widetilde{\omega}_m^2\boldsymbol{M}\begin{bmatrix}\widetilde{\boldsymbol{E}}_m \\ \widetilde{\boldsymbol{P}}_m\end{bmatrix} = 0 \tag{6.8}$$

Where

$$\boldsymbol{K} = \begin{bmatrix}\nabla \times \mu_0^{-1}\nabla \times & 0 \\ \epsilon_\infty\,\omega_p^2 & -\omega_0^2\end{bmatrix} \tag{6.9}$$

$$\mathbf{C} = \begin{bmatrix}0 & 0 \\ 0 & i\gamma\end{bmatrix} \tag{6.10}$$

$$\mathbf{M} = \begin{bmatrix}-\epsilon_\infty & -1 \\ 0 & 1\end{bmatrix} \tag{6.11}$$

Where **K** is the stiffness matrix, **C** is the damping matrix and **M** is the mass matrix .Note that while equation (6.8) is a quadratic polynomial eigenproblem, it is actually entered into COMSOL in the form

(6.5) and (6.7) [7]. The dispersive material properties in equation (6.5) are solved by the weak PDE module and the constant material properties in equation (6.7) are solved by the RF EMW module, exemplified by the MAN freeware [96]. The model outputs include the resonant mode complex eigenfrequencies $\tilde{\omega}_m$ and their field distributions $\tilde{\mathbf{E}}_m$.

6.3 Simulation domain

A simulation takes place within a defined numerical space called the simulation domain. The simulation domain terminates at its boundaries. The physics of these boundaries must be carefully defined in order to prevent unphysical effects such as spurious reflections or parasitic absorptions. At first, one might be tempted to set all fields at the domain boundaries to zero and proceed from there, but setting the fields to zero actually causes waves to reflect back into the domain; recall that an ideal metal forces the electric field to zero at its interface with a dielectric and returns unity reflection. In some cases, reflecting boundaries can be used as mirrors to reduce the size of the computational domain, but in other cases, these reflections may create unphysical situations and should be suppressed. These considerations show that domain boundaries require close attention. A schematic of the simulation domain and its boundaries are shown in figure 6.1. One boundary condition which prevents reflections at boundaries is a “perfectly matched layer,” or PML. This layer prevents reflections by absorbing waves as they propagate through its thickness. The layer must have sufficient mesh points to perform this absorption, and is typically 6-8 mesh points thick. Not all boundaries require PMLs. For instance, the gold substrate on the bottom of the domain in figure 6.1 will naturally reflect EM waves, so they never reach the bottom of the domain boundary and implementing a PML at this boundary would be superfluous.

Moving on to more specific examples, a nanocube on an insulator-coated metal substrate forms a highly symmetric square cavity. We can exploit the symmetry of the system to reduce the size of the computational domain, which is commonly used in the field (e.g. [8] and the QNMEig freeware example simulations [7]). These symmetries allow the computational domain to be split, and mirrors to be placed at these boundaries.

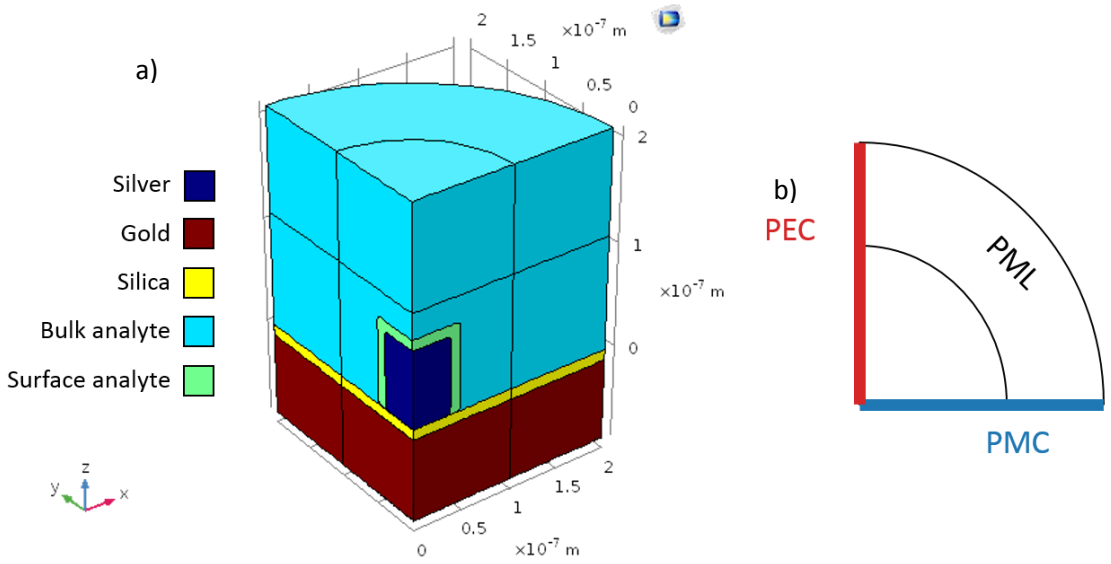

Figure 6.1. COMSOL eigenfrequency simulation domain. a) schematic of domain geometry and materials, b) top view of boundary conditions, including perfect electric conductor (PEC) and perfect magnetic conductor (PMC).

Two types of mirrors are available in COMSOL: perfect electric conductors (PEC) and perfect magnetic conductors (PMC).. The PEC preserves the direction of perpendicular electric field components, inverts the direction of the parallel electric field component and has the opposite effect on magnetic field components. The perfect magnetic conductor preserves the direction of perpendicular magnetic field components, inverts the direction of parallel magnetic field components and has the opposite effect on the electric field components. Both of these boundary conditions are used when simulating the first order MIM mode in the nanocube geometry. It should be noted that such boundary conditions restrict the allowed modes to only those with an odd number of antinode pairs (the *m* number) in the electric field distribution around the azimuthal and even-numbered (*m*) modes are realized by replacing the PMC with a PEC [8].

6.4 Simulating the nanocube MIM resonance in COMSOL

The width of the nanocube MIM resonant cavity is defined by the width of the nanocube, as described by the Fabry-Perot model in section 2.4 and computational modelling in section 4.2. The Fabry-Perot model states that the resonance wavelength is $\lambda_{res} = 2n_{eff}L_{cav} + \phi$ where Lcav is the cavity length, n_{eff} is the effective refractive index of the MIM stack and ϕ is the phase accumulation term arising from the interface. The cavity length is determined by the nanocube size; commercial

nanocubes are available in discrete sizes in multiples of 25nm. These commercial nanocubes, together with effective index of approximately n_{eff}=3.5 allow the cavity resonance to be tuned in 175nm steps. I opted for the 75 nm size, which exhibits a resonance in the 600-700 nm wavelength range that can be measured easily. The n_{eff}=3.5 is calculated from equation 2.18 with silver and silica as metal and insulator respectively The analytical form is restricted to symmetric MIM stacks with the same metal either side of the insulator.

I can tune the resonant wavelength more finely than the discrete cube sizes allow by adjusting other parameters of the system; for example, the resonant wavelength of a cavity is proportional to the effective index of the resonant modes it supports. Since the effective index is a function of the dielectric layer thickness in a MIM structure, the dielectric layer thickness can be used to fine-tune the cavity resonant wavelength.

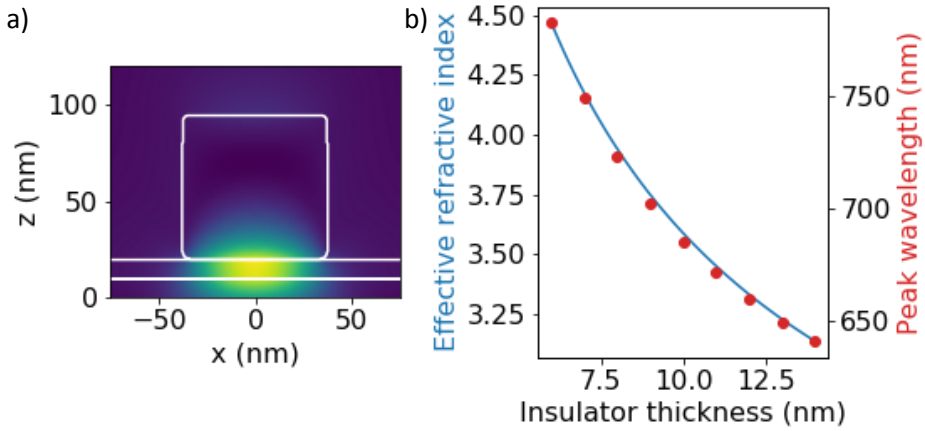

Figure 6.2. Tuning nanocube MIM resonance with insulator thickness. a) Characteristic |H| field plot of the first order MIM resonance. b) Effective refractive index as a function of dielectric thickness for symmetric silver and resonator peak wavelength calculated using QNMEig. The red dots are the peak wavelengths as a function of insulator thickness. The blue curve is the effective refractive index as a function of insulator thickness.

Figure 6.2 illustrates this tunability of the MIM resonance. Figure 6.2a identifies the resonant mode as the first order mode by showing a single lobe in the |H| field, in contrast to the three lobes in the |H| field plot for the lithographically fabricated MIM resonators. Figure 6.2b plots resonance wavelength and effective index against insulator thickness, illustrating the large tuning range that can be achieved. The red dots are the peak wavelengths as a function of insulator thickness. The blue curve is the effective refractive index as a function of insulator thickness. This comparison graph shows that the MIM peak wavelength trend agrees remarkably well with the MIM effective index trend. The MIM

effective index is calculated via the approximation in chapter 2 [12]. The insulator thickness is fixed at 10nm for the rest of the simulations in this section.

6.5 Semi-analytical approach to surface sensitivity

Sensitivity is proportional to the electric field overlap with the analyte (chapter 2). Here, I develop the mathematical framework underpinning this statement and show that the E field sensitivity is given mathematically via the overlap integral.

Starting from Maxwell's equations, the more natural parameters for this discussion are permittivity and frequency rather than refractive index and wavelength. The sensitivity is then described via the frequency shift $\Delta\tilde{\omega}$ as a function of the change in permittivity $\Delta\epsilon$,

$$\frac{\Delta\tilde{\omega}}{\Delta\epsilon} = -\tilde{\omega}\iiint_{V_d} \tilde{\boldsymbol{E}}_p(\boldsymbol{r}) \cdot \tilde{\boldsymbol{E}}\,(\boldsymbol{r}) d^3\boldsymbol{r} \tag{6.12}$$

Where V_d is the volume of the perturbed region, $\tilde{\mathbf{E}}$ is the normalized electric field and $\tilde{\mathbf{E}}_p$ is the perturbed electric field due to the presence of the analyte [65].

The integrand here is $\tilde{\mathbf{E}}\cdot\tilde{\mathbf{E}}$, rather than $\tilde{\mathbf{E}}\cdot\tilde{\mathbf{E}}^*$ found in previous surface sensitivity models for dielectric resonators [59]. The $\tilde{\mathbf{E}}\cdot\tilde{\mathbf{E}}$ integrand used here follows from the $\tilde{\mathbf{E}}\cdot\tilde{\mathbf{E}}$ normalisation condition in section 6.2 : if the total normalised E field is defined using $\tilde{\mathbf{E}}\cdot\tilde{\mathbf{E}}$ then the $\tilde{\mathbf{E}}\cdot\tilde{\mathbf{E}}$ product is also used to calculate a perturbation and using $\tilde{\mathbf{E}}\cdot\tilde{\mathbf{E}}^*$ would simply be incorrect. Using the incorrect $\tilde{\mathbf{E}}\cdot\tilde{\mathbf{E}}$ product leads to errors of the order 20% [65]. The correctness of the $\tilde{\mathbf{E}}\cdot\tilde{\mathbf{E}}$ product may also be understood from recognising that it evaluates to a complex number which includes phase-retardation effects from perturbing the resonator's evanescent E field. In contrast, the conjugated dot product $\tilde{\mathbf{E}}\cdot\tilde{\mathbf{E}}^*$ evaluates to a real number which eliminates information from the complex plane [65].

The electric field of the resonant mode $\tilde{\mathbf{E}}$ is perturbed by changing the refractive index near the resonator. This perturbation is approximated by using the E field boundary conditions at the resonator-shell interface: $\tilde{\boldsymbol{E}}_{\boldsymbol{p}}^{(\boldsymbol{T})} \approx \tilde{\boldsymbol{E}}^{(\boldsymbol{T})}$ for the tangential components and $\tilde{\boldsymbol{E}}_{\boldsymbol{p}}^{(\boldsymbol{N})} \approx \frac{\epsilon_b}{\epsilon_p}\tilde{\boldsymbol{E}}^{(\boldsymbol{N})}$ for the normal component to the nanocube surface. The tangential and normal E field components were selected in COMSOL by removing the bottom corner curvature then simply entering E field component normal to the nanocube facet in order to make the perturbation correction and underlying physics more clear.

Figure 6.3 directly compares the fully simulated resonant frequencies with overlap integral predictions for an un-perturbed ($\tilde{\mathbf{E}}\cdot\tilde{\mathbf{E}}$) and a perturbed ($\tilde{\mathbf{E}}_p\cdot\tilde{\mathbf{E}}$) E field by calculating how the MIM resonant frequency changes when permittivity increases in a 10nm region surrounding the cube. The initial permittivity in this 10nm region is 1.69 which matches the background permittivity so at this point all configurations are identical and their frequencies agree. The model then increases the permittivity in this 10nm region surrounding the cube. The most accurate prediction is the fully simulated data (red dots) but the first order analytical prediction in equation (6.12) comes close and the correcting the normal components of the E field further increases the prediction's accuracy. All three calculations are in broad agreement: the resonant frequency decreases as the permittivity increases. Since the un-perturbed prediction is only linear, it loses accuracy as the permittivity increases and starts to alter the E field at the corners. These discrepancies are smaller for the integral with the corrected E field which estimates the permittivity perturbation. Furthermore, the overlap integral prediction can be converted to more familiar units and is 95nm/RIU.

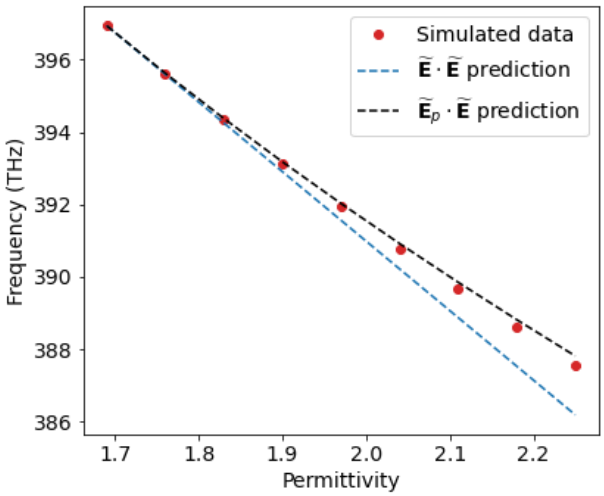

Figure 6.3. Overlap integral predictions compared with simulated resonance wavelength points for permittivity changes in a 10nm region surrounding the nanocube. Two overlap integral predictions are shown: the first makes no correction to the E field, the second corrects the E field components normal to the nanocube surface.

The surface sensitivity physical description is clear: the resonant frequency shift is proportional to the E field overlap with the analyte. The analyte perturbs the evanescent E field by decreasing the amplitude of its component normal to the resonator. This perturbation approximation is provided by the standard E field boundary condition for this normal E field component: $\tilde{\boldsymbol{E}}_{\boldsymbol{p}}^{(\boldsymbol{N})} \approx \frac{\epsilon_b}{\epsilon_p}\tilde{\boldsymbol{E}}^{(\boldsymbol{N})}$. This

physical description makes the MIM's high surface sensitivity origin apparent from a simple E field plot and lays the foundations for further investigations into the MIM's sensitivity.

6.6 Sensitivity of nanocube resonator

The sensing performance of the nanocube MIM was further investigated using the quasinormal mode simulation to calculate the resonance wavelength. These further investigations include the effect of rounding the bottom edge of the nanocube, since the bottom corners of the resonator are where the electric field is largest. TEM images from the certificate of analysis confirm that the nanocube corners are rounded (figure 6.4a) and indications in the literature suggest that corners have a 4nm radius of curvature [5], [40], [132] which agrees with measuring the radius of curvature of figure 6.4a in ImageJ. The refractive index within 10nm and 3nm of the surface was then swept to investigate surface sensitivity while the refractive index of the medium surrounding the cube on top of the entire substrate was swept to calculate bulk sensitivity.

As clearly established above, the sensitivity of the resonant mode is proportional to its E field overlap with the analyte, and the corner curvature directly impacts on the evanescent E field. Figure 6.4b, c detail the E field at the bottom corners of the nanocube. Both electric fields in Figure 6.4b, c are normalised with equation (6.12), because there is no incident field in the QNM framework with which they may otherwise be normalised. Rounding the bottom corners has the effect of pulling the E field up and out of the insulator layer so that more of it overlaps with the analyte. This comparison indicates that the rounded corner geometry leads to a slightly larger sensitivity, both in terms of bulk and surface sensitivity.

The surface sensitivity results are summarized in figure 6.4d, e for nanocube geometries with rounded and sharp bottom corners. The nanocubes are coated with an approximately 3nm thick layer of polyvinylpyrrolidone so I include surface sensitivity for a 3nm layer as well as the 10nm layer used in chapters 4 and 5. The surface sensitivity for the 3nm layer is 54nm/RIU with rounded corners and 41nm/RIU for the sharp corners. The sensitivity is higher for the rounded corner geometry because the rounded corner acts to lift the electric field up and out of the insulator layer so it overlaps more with the analyte layer surrounding the cube, as can be seen when comparing the corresponding field plots in figure 6.4 b and c. These values are similar to the 65nm/RIU sensitivity estimate for the 3nm layer in the next section which, while a coarse estimate, provides a sensitivity estimate in a similar range to these simulations. The surface sensitivity for the 10nm thickness is 105.1 nm/RIU when the

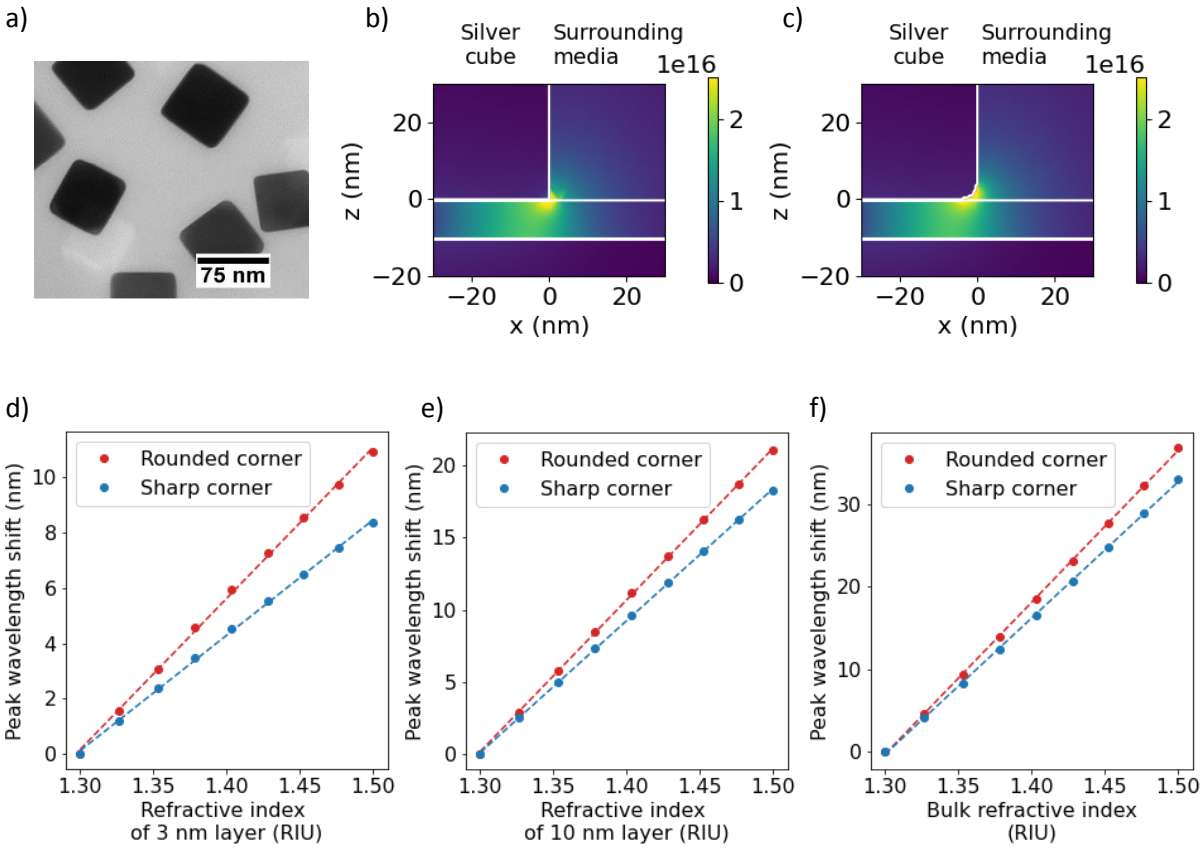

Figure 6.4. Simulated bulk and surface sensitivity for nanocube MIM resonators. a) Rounded corners of nanocubes in TEM image taken from the supplier (Nanocomposix) certificate of analysis. Plots b) and c) detail E field at a sharp and rounded corner geometries respectively normalised with equation (6.2). d), e) and f) show peak wavelength shifts for 3nm thickness, 10nm thickness and a bulk change respectively, for both sharp (b) and rounded (c) corners.

bottom edges are curved and 91.5 nm/RIU without the curved bottom corner. The values for the 10nm layer here compare well to the 95nm/RIU overlap integral estimate in section 6.4.

These simulations provide the opportunity to determine a sensor's bulk sensitivity too. Bulk sensitivity is a convenient way to quantify a sensor's performance and is often used as a benchmark experiment. The simulated bulk sensitivity results are summarized in figure 6.4f for geometries with and without rounded bottom corners. The bulk sensitivity of the nanocube MIM with rounded base corners is 184.0 nm/RIU and without rounded base corners is 165.0 nm/RIU.

For both geometries, the bulk sensitivity is higher than surface sensitivity. The comparatively higher bulk sensitivity indicates that the E field extends beyond the 10nm layer defined around the cube.

Therefore, it is clear that the evanescent tail of the mode extends beyond the 10 nm layer thickness, despite the tightly confined hotspots at the corners.

I attribute meaning to these numbers by comparing them to experimental surface sensitivity results from example dielectric and plasmonic resonators. A dielectric resonator such as a guided mode resonance grating (GMR) has an experimental surface sensitivity of approximately 20nm/RIU for a 10nm layer [85]. Two high performing plasmonic techniques are a gold nanohole array with 30nm/RIU for an 8nm layer shown in experiment [64] or nanodisks with 50nm/RIU for a 10nm layer shown in experiment [77]. The simulations here indicate that the nanocube MIM resonator has approximately 100nm/RIU surface sensitivity for a 10nm layer, surpassing these three techniques found in the literature.

6.7 Limitations of the sensitivity model

The higher sensitivity values due to the nanocube curvature need to be treated with caution. There are three reasons: numerical instability, polymer capping layer and biomolecule binding. These concerns are expanded on in the following three paragraphs.

First of all, numerical instabilities. While the trend of increasing the electric field amplitude by curving the bottom edges of the nanocube is physical, the electric field values may not be accurate. I limited the triangular mesh on the surfaces and tetrahedral mesh in the volumes to have points spaced no larger than 2nm apart in this region. Even with meshes finer than that used here, the sharp wedges of cover media at the corners of these cubes are prone to numerical instability and even numerical singularities [122].

Secondly, commercial nanocubes are coated in a polymer capping layer during their synthesis. This capping layer is quoted as 2nm [40] or 3nm [42], [132] thick in the literature. The capping layer occupies space around the cube, thereby reducing the E field overlap with the analyte and thus reducing the nanocube experimental sensitivity. It should be noted that this polymer layer is not one homogeneous layer in index and thickness because different parts of each polymer chain will bind and unbind to the silver cube over time. And fluid may penetrate the PVP layer to some (unknown) extent. Accounting for these molecular dynamics is beyond the scope of the simulations presented in this chapter. Instead, the bulk sensitivity can be measured by experiment (section 7.2).

Thirdly, biomolecule binding. Since the principle aim of these structures is to measure biomolecule binding, it should be questioned whether a biomolecule would bind at the corner on the underside of

the curved edge where the E field is highest. A biomolecule is more likely to attach at a more accessible binding site on the cube, for example, the middle of the curved corners where silver atoms have lower coordination numbers and are more exposed to the analyte solution. Therefore, the 105.1 nm/RIU surface sensitivity which results from the curved cube edges may be somewhat idealised.

In fact, the exact values for bulk and surface sensitivity presented here should be treated as over-estimates for the three reasons above. While the simulations conducted here are meant to guide the experiments, they do not offer a full picture of a fabricated sensor's sensitivity to biomolecule binding. For a more complete picture, we proceed to fabricating and experimentally measuring the nanocube MIM's sensing performance in the next sections.

Chapter 7

Nanocube MIM fabrication and readout

In this chapter I fabricate nanocube MIM resonators and present their bulk sensitivity. I discuss the bottom-up methods used to pattern the layered substrate presented in chapter 3 and sensing-specific fabrication concerns. Bulk sensitivity is measured first with a spectrometer, then with an intensity-based technique. The intensity based technique yields similar limit of detection when realized research-grade equipment. A low-cost hand-held realization is presented and discussed at the end of the chapter, paving the way to using MIM sensors outside of a laboratory setting.

7.1 Fabricating nanocube MIM

Fabricating a nanocube MIM chip shares a number of steps with fabricating the lithographic MIM chip. Both structures require the same two bottom layers: a smooth gold substrate coated with a thin insulator layer. As with the lithography structures, I start with template-stripped gold, then sputter a 0.6nm Ti adhesion layer followed by 10nm of silica to realize the insulator layer.

Defining the top metal layer is where the similarities between the lithography and nanocube structures end. The top layer of discrete metal features is made by drop-casting 75nm silver nanocubes (Sigma Aldrich NCXSCPH75, stock concentration 1mg/ml) onto the insulator layer described above. The first experiment I conducted was then to use different dilutions of the stock solution and to drop-cast them onto the metal-insulator substrates to study the dependence of concentration on the resulting relative depth of reflection dips in the spectrum.

7.1.1 Dropcasting nanocubes onto the layered substrate surface

I started by diluting the nanocubes in MiliQ (deionized, filtered) water because the water drop has a pinned contact line on the chip which defines a clear, circular shape with clean substrate areas which are useful for normalizing the reflection spectra. The size of drop deposited onto the substrate was held constant at 50µl by using a StarLab ErgoOne Single Channel autopipette. Figure 7.1 summarizes the experiment; as the concentration decreases, the drop of nanocube solution changes from semi-transparent (2.5%) to opaque (20%). The photographs of dried nanocube solution also show that the nanocube area density on the same chip is not uniform. The different coloured areas on the same chip indicate different area densities, especially the "coffee rings" at the edge of all the dried drops.

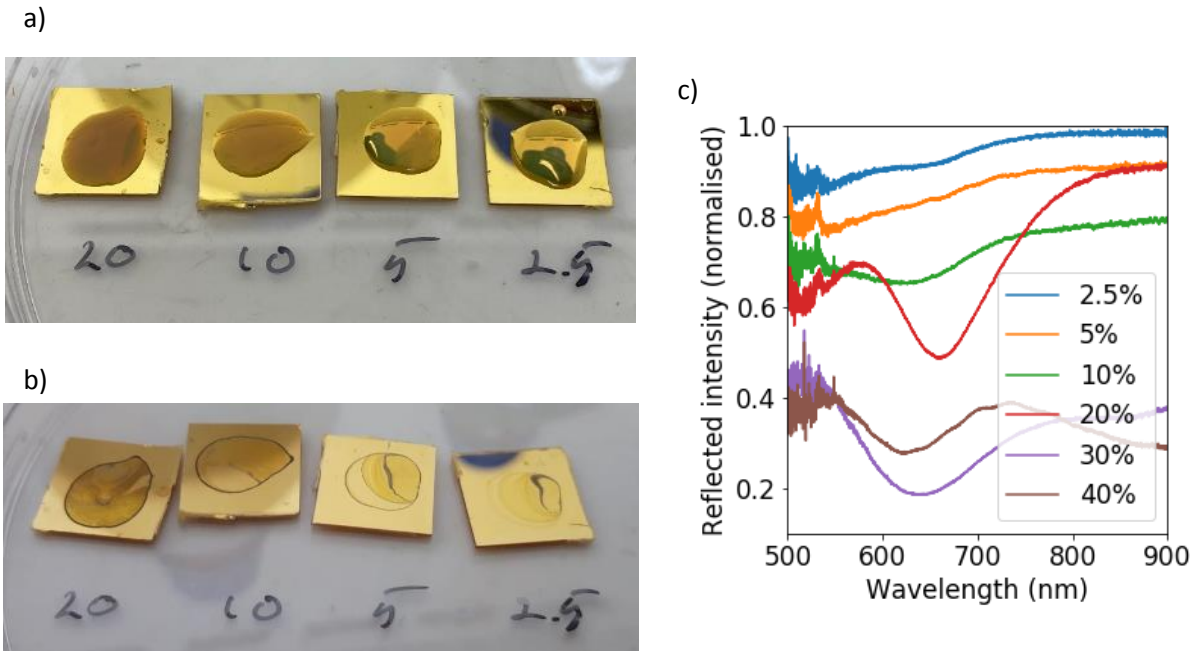

Figure 7.1. Different nanocube concentrations in ultrapure water. a) photographs of nanocube drops and b) dried drops on the MIM substrate. c) reflection spectra of different nanocube concentrations.

Reflection spectra of the different dropcast cube concentrations are measured by taking a spectrum on the cube area and dividing this by a background spectrum on the bare substrate sample. The reflection spectra in figure 7.1 indicate that at 20% concentration, the MIM reflection dip is deepest when compared to the background reflection. Example separation of the cubes and their surface density which resulted in this reflection dip is shown in Figure 7.3a. Below 20% concentration, the MIM signal becomes less well defined. Above 20%, the MIM peak is still present but the background reflection decreases so that the absorption dip relative to this background actually decreases.

Microscopic observation confirms that the “coffee rings” at the edges of the dry drops are areas of high density nanocubes. These coffee rings are undesirable because they remove nanocubes from the middle of the chip thereby reducing the MIM extinction ratio. Also, the dense packing reduces performance, as shown in figure 7.1c. Since the coffee rings need a pinned contact line where the solvent meets the surface for their formation [133] removing this contact line should remove the rings.

To this end, I diluted the nanocubes in ethanol instead of water. Figure 7.2a shows the same wet ethanol drop on a substrate at increasing times after the drop was deposited on the substrate. At first, the nanocubes diluted with ethanol spread out over the entire chip surface, but over time the ethanol drop contact line recedes. The receding contact line negates the coffee ring effect. However, since the drop spreads out over the entire surface, cubes are also deposited over the surface and there is no longer any blank substrate area with which the reflection spectrum can be normalized. In order to define a clean substrate area for normalization and ensure no cubes stick to this clean substrate region, I used a kapton tape mask to cover parts of the substrate. The kapton tape mask kept most of the ethanol drop inside the defined area, and ensured nanocubes did not land on the masked areas. The photograph of a dried masked drop of nanocubes in figure 7.2b using this method shows a more uniform colour distribution, indicating a more uniform distribution of nanocubes. In particular, the edges of the covered areas show a lighter-coloured coffee ring, indicating that ethanol suppresses the coffee ring effect. A 10% concentration of stock concentration now causes the

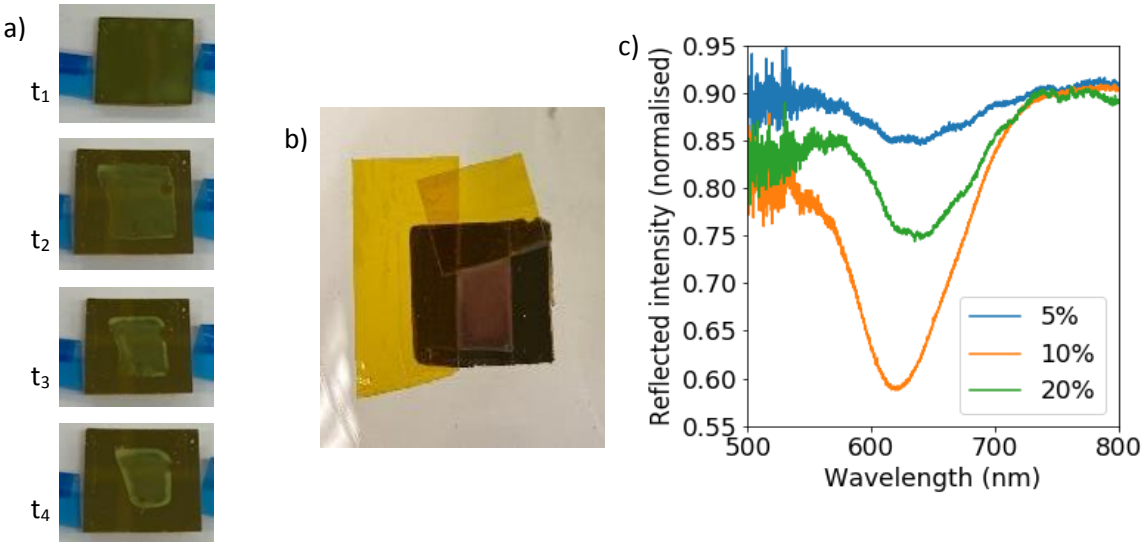

Figure 7.2. Diluting and dropcasting nanocubes in ethanol a) receding contact line of the same ethanol solution on substrate over time, b) kapton tape mask used to create cube covered and clean regions, c) spectra resulting from different cube dilutions

deepest nanocube absoption dip when the cubes are diluted in ethanol, compared to 20% concentration in water which further indicates that more nanocubes land in the middle of the chip rather than at the edges. Both higher and lower concentrations result in a lower absorption signal from the nanocubes as shown by the spectra of figure 7.2c.

The next issue arose when rinsing the sensor chips after deposition. When using water or isopropyl alcohol, the nanocubes were also removed from the surface, as shown in figure 7.3b. To address this problem, I coated the surface with an organo-silane adhesion layer prior to depositing the nanocubes. In particular, I used (3mercatopropyl)trimethoxysilane (MPTMS) because it is a commonly used organosilane adhesion layer both in the research group and in the literature [109], [110], [134]–[136].

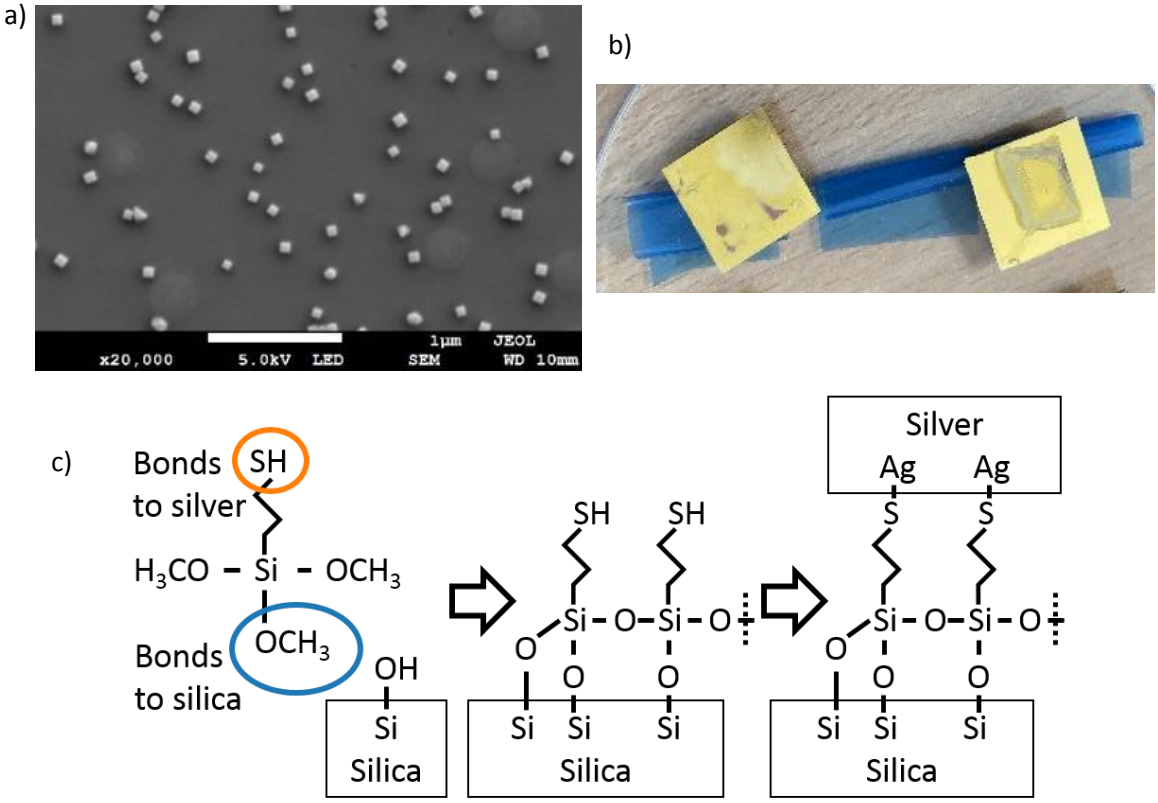

Figure 7.3. Attatching nanocubes to the silica surface with MPTMS a) SEM example nanocube distribution on the substrate. b) nanocubes without (left) and with (right) MPTMS adhesion layer and c) schematic of how MPTMS molecule may attach to silver, silica and other MPTMS molecules

Figure 7.3 compares the sample surface with and without coating the silica layer with MPTMS (mercaptopropyltrimethoxysilane), showing that the MPTMS causes the nanocubes to adsorb to the surface without getting rinsed off. I note that the organosilane adhesion layer is optically transparent, so it does not impact on the optical performance of the sensor, in contrast to the

metallic adhesion layer that was required for the lithographic MIM (chapter 5) that caused additional loss [109]. In order to apply the coating, the substrates were left in a 4% solution of MTPMS dissolved in anhydrous isopropyl alcohol overnight before dropcasting the nanocubes onto them. The reaction between MTPMS and a silica surface is illustrated in figure 7.3c: the methoxy ($–OCH_3$) groups are substituted by surface hydroxyl groups (-OH) on the silica surface to form Si-O-Si bonds between the surface and the silicon atom in MPTMS while eliminating methanol (CH_3OH). The reaction between MPTMS and water can result in Si-O-Si bonds between the organosilicon groups as illustrated in figure 7.3 [136]. The sulfur atom in the mercapto- group forms strong covalent bonds to the metals (gold, silver and copper) [137].

7.1.2 Verifying the nanocube MIM resonance by varying insulator layer thickness

The reflection dips apparent around 630 nm wavelength in figure 7.2 can be verified as a MIM resonances by observing how their position is affected by insulator thickness. Increasing insulator thickness reduces the effective index of the MIM waveguide, as modelled in section 2.3.2 which in turn reduces the resonance wavelength as shown in section 6.3. Three different silica thicknesses were sputtered onto template stripped gold, as shown in figure 7.4, in order to verify that the dip at ~630nm is due to a MIM resonance. The result is shown in figure 7.4, and the resonances display the expected trend: the resonance wavelength decreases as the insulator thickness increases for the same size nanocubes.

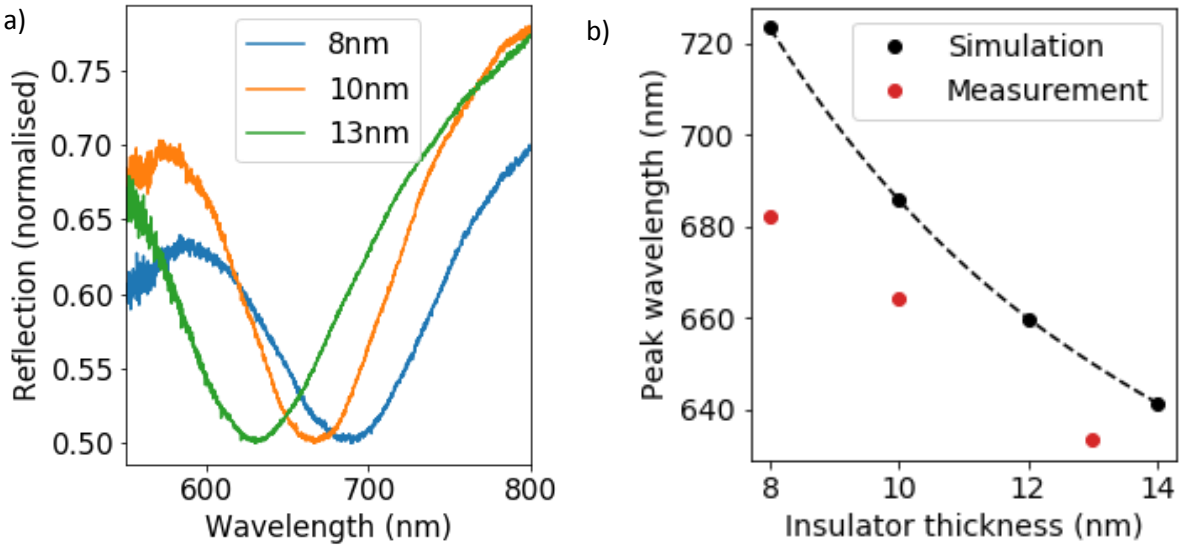

Figure 7.4. Nanocube MIM resonance position with different insulator thicknesses a) reflection spectra and b) experimental vs simulated resonacne wavelength at different insulator thicknesses.

While the trend observed in this experiment qualitatively agrees with the simulated data, I note that there is a 30-40nm offset between the absolute peak values. This offset indicates that the sputtered silica layer is thicker than the value quoted; comparing simulation and experiment, the difference can be explained by a thickness variation of approx. 2nm; this difference can be explained by the presence of the coatings, i.e. substrate being coated in MPTMS and the nanocubes being coated in a polymer polyvinylpyrrolidone (PVP) capping layer to avoid cluster formation. These extra layers will contribute to the total insulator layer thickness. For comparison, previous work on other nanocube structures quote PVP thicknesses of 2nm [40] or 3nm [42], [132] and a MPTMS monolayer thickness of ~1nm [134]. Additionally, thiolated molecules such as MPTMS have been shown to completely displace PVP in solution [138], but since these cubes are deposited onto a surface it is likely that some PVP remains between the cubes and the silica surface contributing to the total insulator layer thickness.

7.2 Bulk sensitivity measured with spectrometer

The bulk sensitivity describes the system response to the change in refractive index in the bulk space above the sensor [9], [58], [62], [72]. The bulk sensitivity result presented here is analogous to the bulk sensitivity result presented in section 5.2. The bulk refractive index above the sensor chip is varied by flowing aqueous solutions of salt (sodium chloride) over the sensor surface, encased in the microfluidic flow cell detailed in chapter 3. Salt concentrations of 75, 100, 125 and 150 sodium chloride in mg/ml were prepared and pumped through the fluidic channel which provide refractive index shifts of approximately 0.005 RIU between concentrations. The refractive index of the different

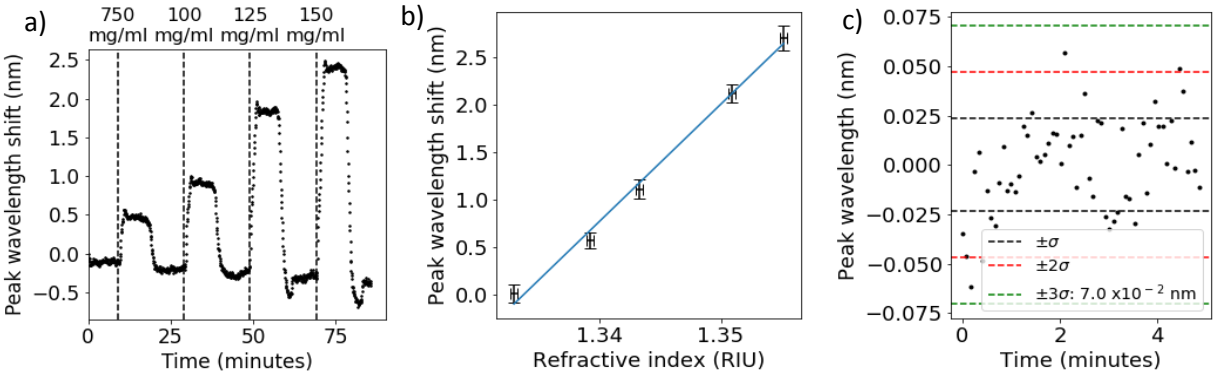

Figure 7.5. Bulk sensitivity measured with a spectrometer. a) Peak wavelength shift over time. b) Peak wavelength shift vs. refractive index with linear fit to calculate sensitivity. c) Noise floor of the bulk measurement.

solutions was measured using a digital refractometer (Reichert brix/ri-chek refractometer). Here, I measure the peak wavelength shift in nanometers so bulk sensitivity is quantified in units of nm/RIU.

The spectra were recorded every 10 seconds with a thorlabs CCS175 spectrometer while salt solutions were flowed through the fluidic assembly. The peak wavelength was determined by fitting a peak to these recorded spectra. My assumption is that the width of the wavelength response of the system is given by the statistical size variation of the nanocubes (not the individual resonances curves), so I used a Gaussian curve to fit the spectra. This approach is confirmed by noting that the resulting Gaussian curve has a full-width at half maximum of 22% which is greater than the 10% full-width half-maximum of the individual resonance peaks. Therefore, the Gaussian nature of the distribution dominates and a Gaussian peak is fitted to determine the peak wavelength.

An increase in peak wavelength occurs when a salt solution of higher refractive index is flowed over the sensor, consistent with the expectation that the peak red-shifts when the evanescent tails experience a higher refractive index, as described by the simulations in section Sensitivity of nanocube resonator6.5 and 6.6. The peak wavelength shift is quantified by subtracting the mean peak wavelength from the top of a “step” in peak wavelength while a salt solution is flowing over the sensor. The standard deviations in peak wavelength before and after each step were combined in quadrature to provide the wavelength error bars in figure 7.5. The peak wavelength shows no change while DI water flows through the fluidics which allows a “zero point” to be included. The standard deviation of a repeated refractive index measurement of the same solution is $3x10^{-4}$ RIU, which provides the refractive index error bars.

The bulk sensitivity was calculated by fitting a straight line to the peak wavelength shifts as a function of refractive index to determine the 122nm/RIU bulk sensitivity for the nanocube refractive index sensor. This value is lower than the 180nm/RIU from chapter 6’s simulations because the commercial nanocubes are covered in a capping layer which occupies volume in the evanescent electric field and reduces E field overlap with the changing bulk analyte. The minimum bulk refractive index change that this system is able to resolve is the ratio of noise floor to the bulk sensitivity. The 3σ noise floor is $7.0x10^{-2}$ nm, which gives the minimum resolvable refractive index change as $5.7x10^{-4}$ RIU.

I note that figure 7.5a shows a drift, i.e. the baseline peak wavelength slowly decreases with time. As a possible explanation, I note that the previously mentioned PVP capping layer is still present on the nanocubes during this bulk measurement, and PVP is soluble in water. The downward drift may

therefore be caused by PVP gradually rinsing off the cube surfaces which will lower the average refractive index of the space surrounding the nanocubes. Therefore, the effective index of the resonance gradually decreases, which is consistent with the gradual but steady blue shift in resonance wavelength observed here. This downward drift is consistent across measurements taken with the spectrometer. Given sufficient time, all the PVP will be removed and this downward drift should flatten out. The cubes are attached to the silica surface via MPTMS and not PVP, although it is highly likely that a small number of cubes detach during each measurement.

7.3 Intensity-based readout

The ideal readout method for a sensing device should be low-cost and use commercially available components for simple assembly. To this end, this section describes investigations into measuring the peak wavelength shift of the MIM resonator with a simple photodiode and detector. The prototype design and assembly is summarized in figure 7.6. This design is also compact and only uses one lens: the ball lens on the LED. The intensity-based readout was first realized using research grade electronics equipment (section 7.3.2), then a low-cost microcontroller board (section 7.3.4).

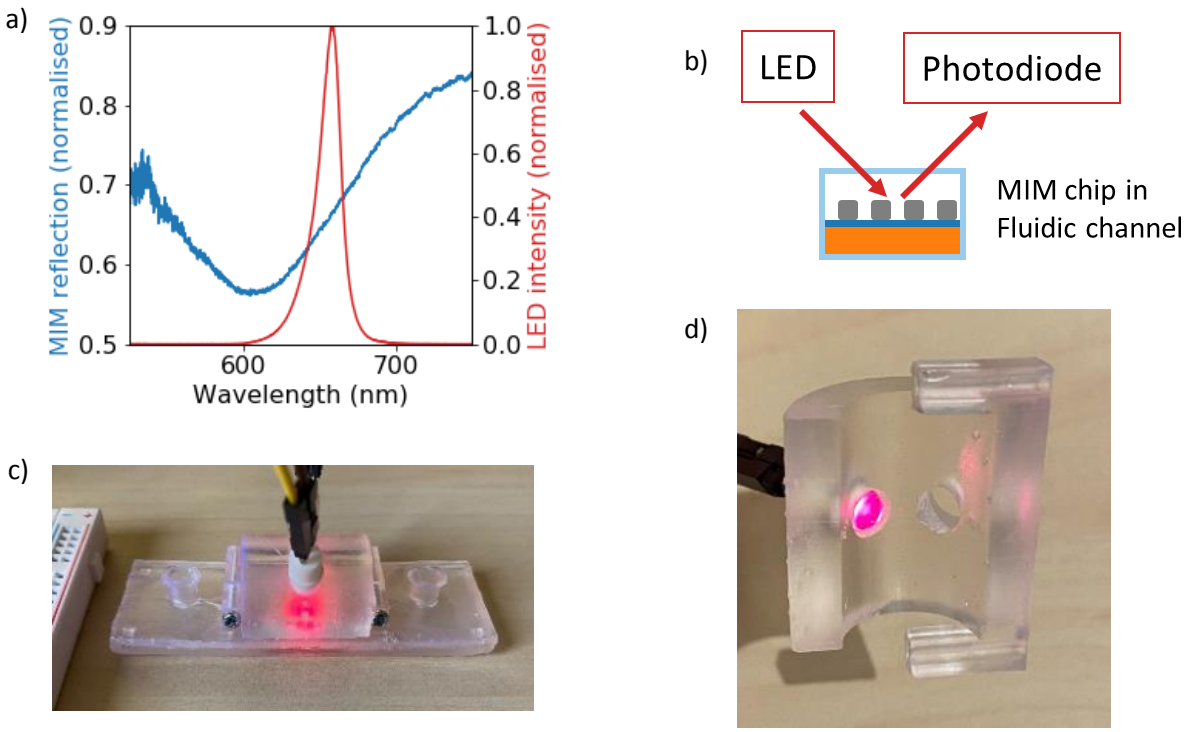

Figure 7.6. LED intensity based setup: a) spectra, b) schematic of measurement setup, c) photograph 3D printed holder incorporated into microfluidics and d) underside of 3D printed component holder including LED.

The idea is to detect the wavelength shift directly via a change in reflectivity; as the refractive index causes the resonance wavelength to increase, the corresponding shift of the resonance curve will change the total reflected signal of the LED. These changes in reflectivity can be monitored via a 660nm LED incident on the nanocube sample and its reflection is measured by a silicon photodiode. As the resonance wavelength increases, the MIM resonance dip overlaps more with the LED emission spectrum and less light is reflected. In short: the setup converts a refractive index change into a voltage.

Unfortunately, this approach, while very simple, is highly susceptible to various sources of noise. The LED intensity is affected by electrical noise in the LED driving signal. The photodiode introduces optical noise from the surroundings since it collects light from across the visible spectrum, not only the 650-700nm spectral region of interest. The assembly is susceptible to mechanical noise from the surroundings since mechanical noise can move LED and photodiode, thus changing the intensity of incident light on the photodiode from the LED beam profile. An analogy can be drawn between an intensity-based readout and fitting a spectrum by considering AM vs FM encoding of radio transmission. Both FM and curve fitting are robust against changes in source intensity since the signal is demodulated by comparing values relative to each other at different frequencies/wavelengths, which results in lower noise. However, the reduced noise comes at the cost of a higher bandwidth. Conversely, AM and intensity-based readouts use a smaller bandwidth but are more susceptible to noise from changes in the source intensity [71].

The remaining source of noise is optical noise from the surroundings, i.e. background light. This noise can be removed by a simple version of the lock-in technique, i.e. by modulating the LED at a set frequency and amplifying only the signals in a narrow band around this modulating frequency. Signals outside this frequency band are not amplified since any periodic signal can be decomposed into sine waves, which are orthogonal to the frequency of the amplified signal. Any DC background signal is then subtracted as an offset.

7.3.1 Intensity readout performance estimate

Suitable components for this assembly are selected by first estimating magnitude of shifts that these components must detect. A convenient starting point to estimate these shifts is the bulk sensitivity data presented in figure 7.5 and spectra in figure 7.6. Figure 7.5 states the wavelength shifts caused by different bulk refractive indices and the spectra in figure 7.6 allows the absorption of the LED signal by MIM structure to be calculated by an overlap integral between the two profiles. The result is

that a 0.01 bulk refractive index change causes a 0.5nm peak wavelength shift which, in turn, causes an estimated 0.1% change in reflected LED intensity. Therefore, the intensity-based configuration must, at a bare minimum, be able to resolve 0.1% changes in LED brightness to detect the same concentration salt solutions used in figure 7.5.

The photodiode transduces the reflected optical intensity into an electrical current, proportional to the intensity of incident light. The photodiode's sensitivity to illumination is increased by increasing the width of the region which is sensitive to illuminating photons- the depletion region. The width of this region is increased by applying a negative or reverse bias to the photodiode, but applying a reverse bias also increases the dark current. At 5V reverse bias an OSRAM TO18 BPX65 detector has 0.5A/W sensitivity and 1nA dark current. I expect that the 1nA dark current is negligible, but proceed with the estimation regardless.

The incident power of a Thorlabs LED660L LED on the photodiode is in the 100µW range, which means that the current flowing through a 0.5 A/W detector is in the 100µA range. The anticipated changes in the photocurrent are 0.1% of 100µA, or $1x10^{-7}$ A, two orders of magnitude larger than the $1x10^{-9}$ A dark current. Therefore, I conclude that the signal due to a bulk refractive index shift should be readily resolvable above the dark current in the system.

Assuming, conversely, that the readout is limited by the dark current from the photodiode, the above estimation can be run "backwards," calculating the refractive index change which 1nA current shift indicates. This bulk refractive index change is of the order of $1x10^{-4}$ RIU, which provides an estimate for the intensity-based readout's limit of detection.

7.3.2 Research grade assembly

As a first step, the assembly was tested with research-grade electronics equipment (Keithley 2110 multimeter, Yokogawa 7651 programmable DC source) in order to assess the performance of the low-cost LED and photodiode while introducing minimal electrical noise from the voltage source and measurement. Both the signal modulation and amplification are performed by a Stanford research systems SR810 DSP lock-in amplifier. Figure 7.5 was measured using a spectrometer, not with the intensity based measurement. The mechanical noise was suppressed by fixing the components in place with optical retention putty and attaching wires to the lab bench with tape.

The research grade electronics equipment required some intermediate circuitry in order to drive the LED with a sinusoidal voltage and measure the current flowing through the photodiode. I used a

research grade multimeter and voltage source throughout the measurements in the following sections (Keithley 2110 multimeter, Yokogawa 7651 programmable DC source, SRS810 DSP lock-in amplifier).

The first element to consider is the lock-in amplifier; it provides a sine wave to modulate the LED source. The problem is that this sine signal oscillates between positive and negative voltages around 0V but the LED only emits light when a positive voltage is applied. The sinusoidal driving voltage therefore requires a DC offset to ensure the LED has only positive voltages applied and to increase the LED brightness. Simply adding the DC offset in series is ineffective, because the offset would be removed by the ground terminal of the instrument providing the sinusoidal signal. Instead, the signals must be added at a junction with low input impedance. Such a low input impedance junction is provided by a non-inverting summing amplifier, schematically shown in figure 7.7. The DC offset is selected with a variable resistor in series with a 5 V power supply. This amplifier configuration adds the sine wave and the DC offset so that the LED driving voltage is entirely positive. The resistors are then selected to ensure that the amplifier's gain is equal to unity (gain=1) [139].

Measuring the incident light on the photodiode is simpler. The current which flows through the photodiode is converted to a voltage by connecting the photodiode in series with a 1MΩ resistor. Since V=IR, a small change in current can be converted to a larger change in voltage by a large resistor value. However, this resistor must not exceed the input impedance of the lock-in amplifier, otherwise the majority of the current will flow through the lock-in amplifier rather than the external resistor. The input impedance of the lock-in amplifier is 10MΩ so I selected a 1MΩ resistor to go in series with the photodiode. The voltage across the 1MΩ resistor was used as the input to the lock-in amplifier so the intensity of the modulated LED signal could be measured after it had reflected from the sample.

Another consideration for the measurement circuit is its response time. A circuit takes time to respond to changes in current flow due to components and having a capacitance C. The capacitance of the photodiode is 11pF and the resistance of the series resistor is 1MΩ so the response time $\tau = RC$ for this circuit is 1.1µs, corresponding to response frequency $f_r = \frac{1}{2\pi\tau}$ = 14.5kHz, well above the 513Hz operating frequency selected for the lock-in amplifier measurement.

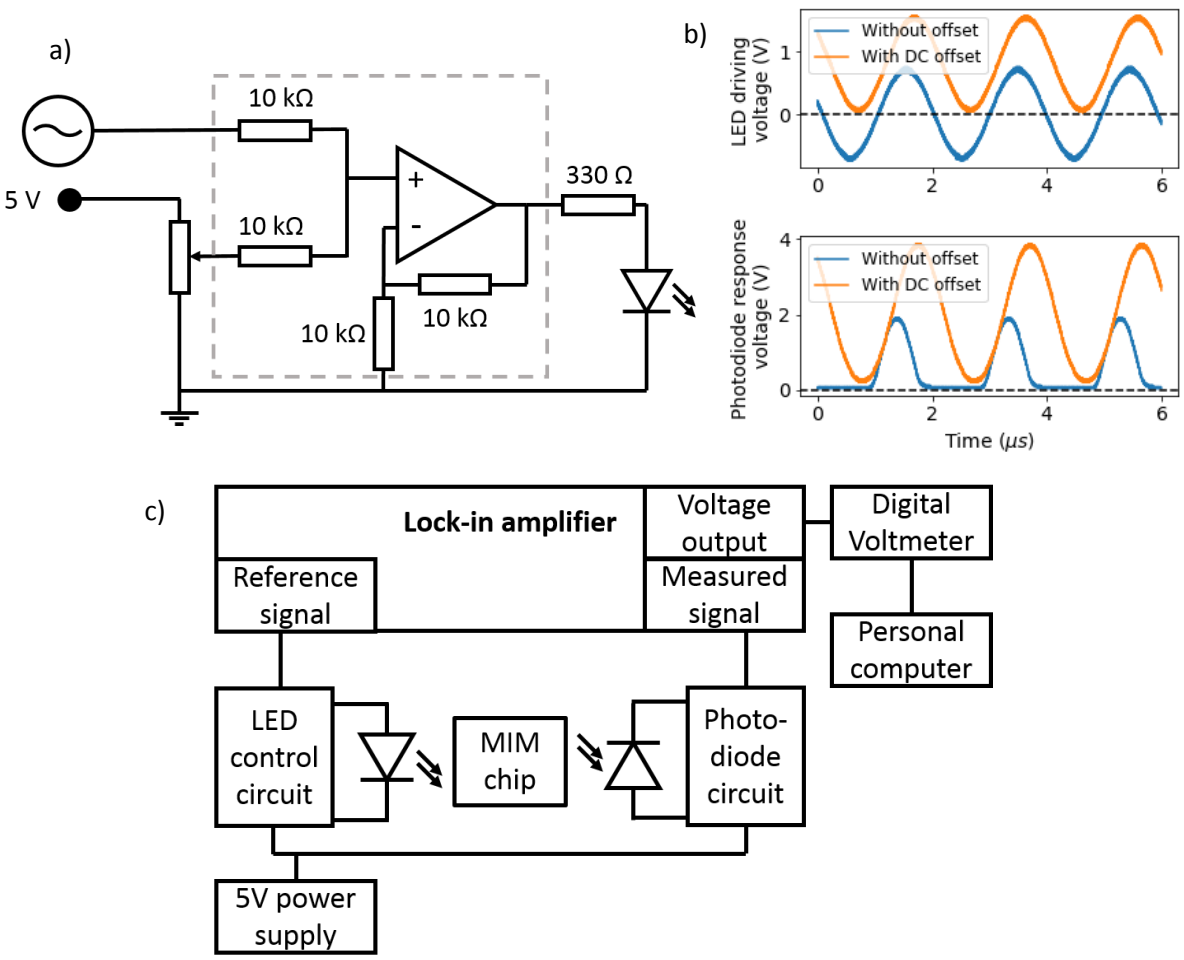

Figure 7.7. LED driving circuit for intensity-based readout. a) Schematic of the driving circuit with non-inverting amplifier within the grey dashed box. b) Measured voltage from the photodiode when illuminated by the LED with and without offset. c) Schematic showing the full experimental setup and which different electronic devices were connected.

Using this setup, I conducted the bulk sensitivity measurement for a typical duration of an hour and a half, taking intensity measurements every few seconds to obtain an accurate intensity trace. Recording the data at such a frequency and duration was enabled by computer automation. A LabVIEW program recorded the output voltage from the lock-in amplifier, measured by a Keithley 2110 multimeter every two seconds.

7.3.3 Research grade assembly bulk sensitivity results

The performance of the LED assembly described above was assessed by measuring the bulk sensitivity of a nanocube MIM sensor. The bulk sensitivity was chosen to benchmark this configuration because

it is easy to conduct and because its results can be readily compared to the spectrometer measurements in section 7.2.

In order to conduct this measurement, I injected 1ml of 3 different salt solutions into the flow system with a sample loop and pumped them through microfluidic channels at 70 µl/min. I measured the detector voltage every two seconds using the LabVIEW program. The change in voltage over time is plotted in figure 7.8 along with the change in voltage as a function of refractive index and the noise floor. The LED-photodiode configuration measures the sensitivity in V/RIU, since the change in readout voltage is the dependent variable, in contrast to the spectrometer measurement which measures the sensitivity in nm/RIU.

The graphs show clear a shift with refractive index. These shifts in voltage are negative and are consistent with the expectation that the sensor's reflection with will decrease when covered with a higher refractive index solution as previously described. The repeated measurements show that the steps in voltage due to a refractive index change have similar magnitudes and the same shape steps within the same measurement.

However, the repeated measurements show that the voltage steps for different salt solutions have different shapes between repeated measurements. The difference in step shapes must be due to a factor which is constant during a single measurement but varies between measurements and only becomes apparent when a new fluid is introduced to the system. One such factor is the microfluidics. The ideal microfluidic assembly would only support laminar flow, but the experimental 3D printed assembly may have bumps, voids or large particulate contaminants which introduce turbulence and eddies. These eddies would cause the salt solution to pass non-uniformly over the sensor surface and reach some areas before others due to the fluid front getting pinned at different points within the fluidic channel. This non-uniform coverage will cause the voltage to shift in irregular steps while different portions of the sensor become covered with salt solution, which in turn causes the differently shaped voltage steps between repeated measurements in figure 7.8.

The standard deviation of voltage before and after each step were combined in quadrature to provide the voltage error bars in figure 7.8. The refractive index of the different salt solutions was measured with a digital refractometer (Reichert brix/ri-chek refractometer) and are approximately 0.01RIU apart, as shown in figure 7.8. The standard deviation of a repeated refractive index measurement of the same solution is 3x10-4 RIU which provides the refractive index error bars. The output voltage

shows no change while DI water flows through the fluidics (and in the absence of any movement in the vicinity of the setup) which allows a “zero point” to be included.

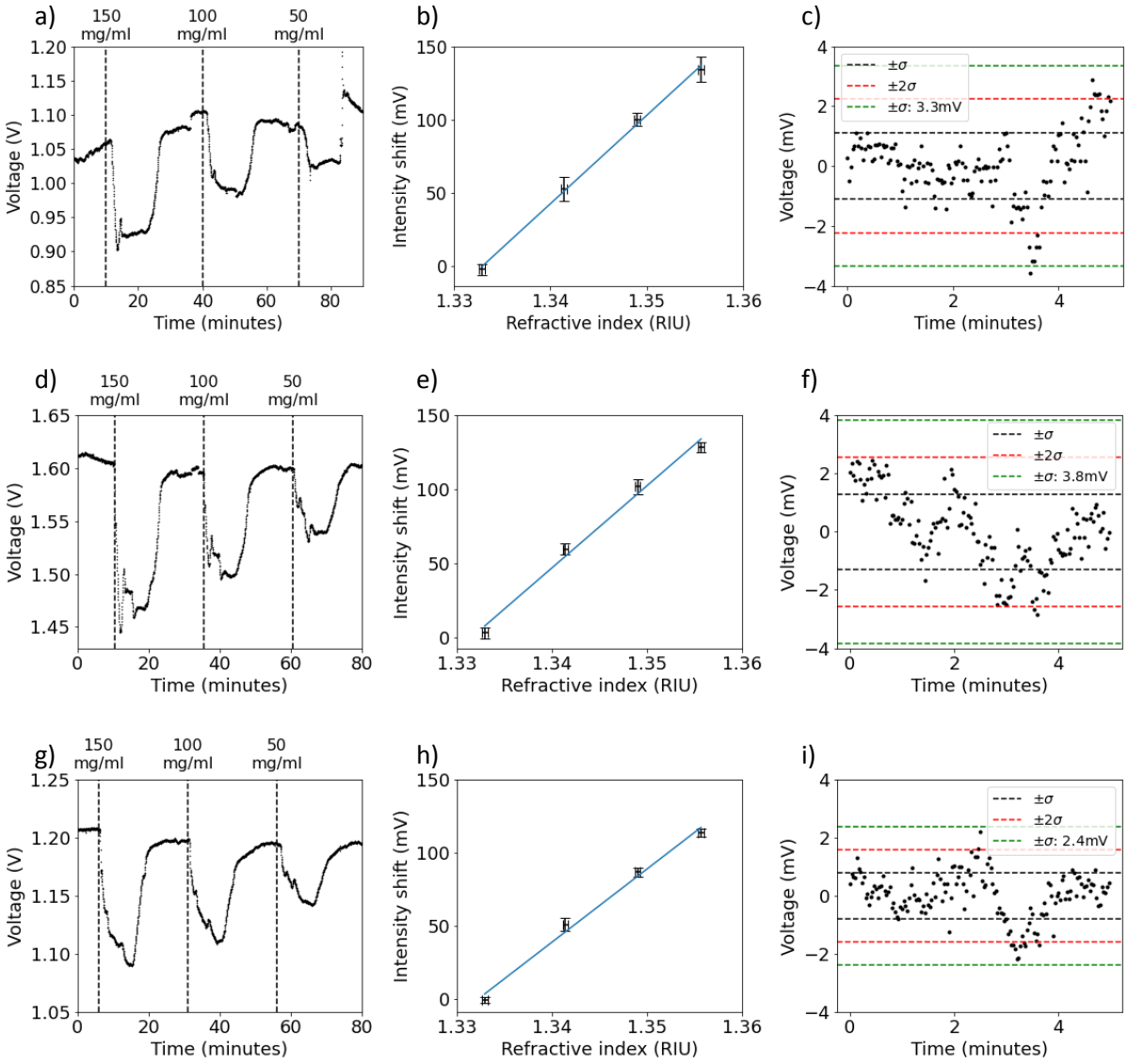

Figure 7.8. Summary of research-grade assembly intensity readout results. Rows are experimental repeats. a, d and g) are voltages measured over time while different concentration salt solutions flow through the fluidics. b, e and h) are the sensitivity graphs of change in voltage as a function of refractive index. c, f and i) are noise floors from each experiment.

The sensitivity of this technique was determined by fitting a straight line to the voltage points as a function of change in refractive index. The sensitivity values across the experiments are 6.01 V/RIU, 5.53 V/RIU and 5.00V/RIU. These figures provide some expectation as to the shifts that can be expected with such an amplified system, but they do not yet allow this experimental setup to be readily compared to the former spectrometer setup.

A more comparable figure of merit is the minimum refractive index change which can be determined by this configuration. This limit of detection is calculated by dividing the observed shifts by the noise floor (third column in figure 7.8). The corresponding limits of detection are 5.6×10^{-4} RIU, 6.9×10^{-4} RIU and 4.8×10^{-4} RIU. These limits of detection are close in value to 5.7×10^{-4} RIU obtained when measuring bulk sensitivity with the spectrometer in section 7.2.

The setup's limitations may arise from electronics, mechanics and fluidics. The electronics limitation appears to be the dark current from the photodiode, since the above limit of detection is reasonably similar to the estimate based on the dark current in 7.3.1. Both electrical and mechanical noise are introduced by the presence of the microfluidic pump and its vibrations, which may increase the setup's limit of detection from the estimated 1×10^{-4} RIU to 5×10^{-4} RIU. The fluidics and contamination therein cause turbulence and irregular steps in voltage discussed above.

Following these tests with research grade instrumentation, I investigate the same setup with low-cost electronics as a next step in order to check the suitability of the system for handheld operation.

7.3.4 Low-cost assembly readout

I designed and assembled a low-cost alternative to the research grade intensity based readout method. The low-cost assembly must modulate the LED brightness, convert the analog voltage from a photodiode to a digital value and send this digital value to a personal computer. These three tasks may be performed by a microcontroller. Microcontrollers are small, low-cost computers in a single integrated circuit (IC) which are programmed to execute the aforementioned tasks. They may even be programmed to digitally filter signals [140], making them ideal for this low-cost lock-in assembly. This section uses a Texas Instruments MSP432P401R microcontroller Launchpad board. The circuit schematic for this configuration is given in figure 7.9.

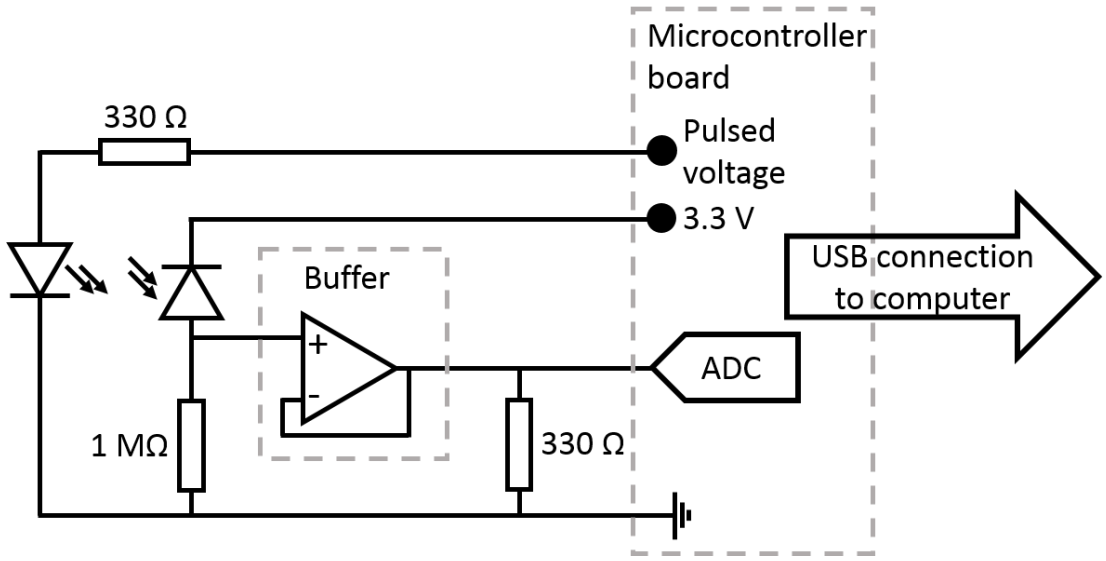

Figure 7.9. Circuit diagram of low-cost microcontroller intensity readout. The unity-gain or buffer amplifier is highlighted by the dashed grey box.

Since the microcontroller is a purely digital device whose output signals are either high (3.3V) or low (0V), this low-cost setup was limited to modulating the LED with a square wave and measuring the detector voltage at the Nyquist frequency (512 Hz in this case). Sampling at the lowest possible frequency appears exceedingly reductionist, but sampling this way using a microcontroller has been shown to recover signals down to 85dB below interference [140]. 200 digital values were recorded for the duration of 100 LED pulses then sent to a personal computer to be averaged and recover the original signal.

Changes in the analog voltage input of the order 0.1% must be resolved to detect refractive index changes of the order 0.01 RIU. These analog voltages are converted to digital values using the microcontroller's analog to digital converter (ADC). The ADC measures voltages in 200 µV, or 0.006% variations between its low (ground) and high (3.3V) logic levels. The ADC resolution is determined by its 14 bit depth, corresponding to 16384 divisions between the high and low voltage levels and is sufficient to resolve the anticipated ~0.1% changes in input voltage

In fact, the quantization staircase imposed by the ADC may not be as strict as first appears, due to dithering between the digital voltage levels. The signal is expected to include noise which, if of the order of 200 µV, serves to add random variation between the voltage levels. The random variation is removed when the digital output values are averaged to recover the original signal, with the effect of returning an average value somewhere between the discrete ADC voltage levels. In some cases this dither technique is intentionally employed to smooth an otherwise discretized signal [141].

As with the research-grade assembly, the current which flows through the photodiode is converted into a voltage by a 1MΩ resistor in series. The external resistor must not exceed the ADC input pin impedance in order to successfully measure a potential difference. However, unlike the 10 MΩ SRS lock-in amplifier input impedance, the ADC pin has a relatively low 1kΩ maximum input impedance. Fortunately, it is possible to reduce the output impedance of the photodiode circuit through a unity-gain, or buffer amplifier [142]. The output of the sensing circuit is input to an op amp (MCP6002), configured to have unity gain. The output voltage is the same as the input voltage, but with a low impedance (an ideal op amp has zero output impedance). Thus, the output impedance of the photodiode circuit is lower than the ADC pin input impedance.

The measurement process has a number of tasks which have different timing requirements. The lock-in process itself requires that the frequency of the LED pulses and ADC triggering be precisely controlled and synchronized. The LED is pulsed at 512Hz frequency (to closely match the 513Hz used in section 7.3.3) and the ADC is triggered twice per cycle to record the reflected LED brightness and the background brightness. The timing of both these tasks is controlled by the precision low-frequency clock in the microcontroller which is in turn sourced by an external low-frequency 32.768 kHz oscillator on the circuit board to ensure the processes are well-synchronized.

The ADC conversion and serial communication also require timing. The ADC conversion requires multiple clock cycles per ADC sample before the next sample may be triggered. The timing of these processes must not interfere with the lock-in measurement and must not be interrupted by the ADC trigger, so I selected the internal master clock, sourced by a separate 12MHz oscillator. This oscillator is 3 orders of magnitude faster than the low-frequency oscillator which controls the LED pulses and hardware, ensuring sufficient clock cycles to perform ADC conversions between ADC trigger events.

7.3.5 Low-cost bulk sensitivity results

The results of using the low-cost intensity based readout to measure different salt solutions are presented in figure 7.10. The voltage shows clear downward steps with the injection of each new salt solution to the sensor, consistent with the previous results in section 7.3.3. The shift magnitude is approximately 0.1% for a 0.01 change in bulk refractive index, consistent with the estimation in 7.3.1.

The three experiments have 1.6V/RIU, 1.8V/RIU and 1.9V/RIU sensitivities to bulk refractive index changes which have a spread (standard deviation) of 0.1 V/RIU or approximately 7% between values. The error bars of these voltage shifts in the sensitivity graphs are calculated by combining the

standard deviations of the voltage before and after the refractive index change in quadrature, the same method as the research-grade assembly results in figure 7.8. The noise floor was calculated by selecting a 5 minute period over which there was no refractive index change and calculating the standard deviation in voltage.

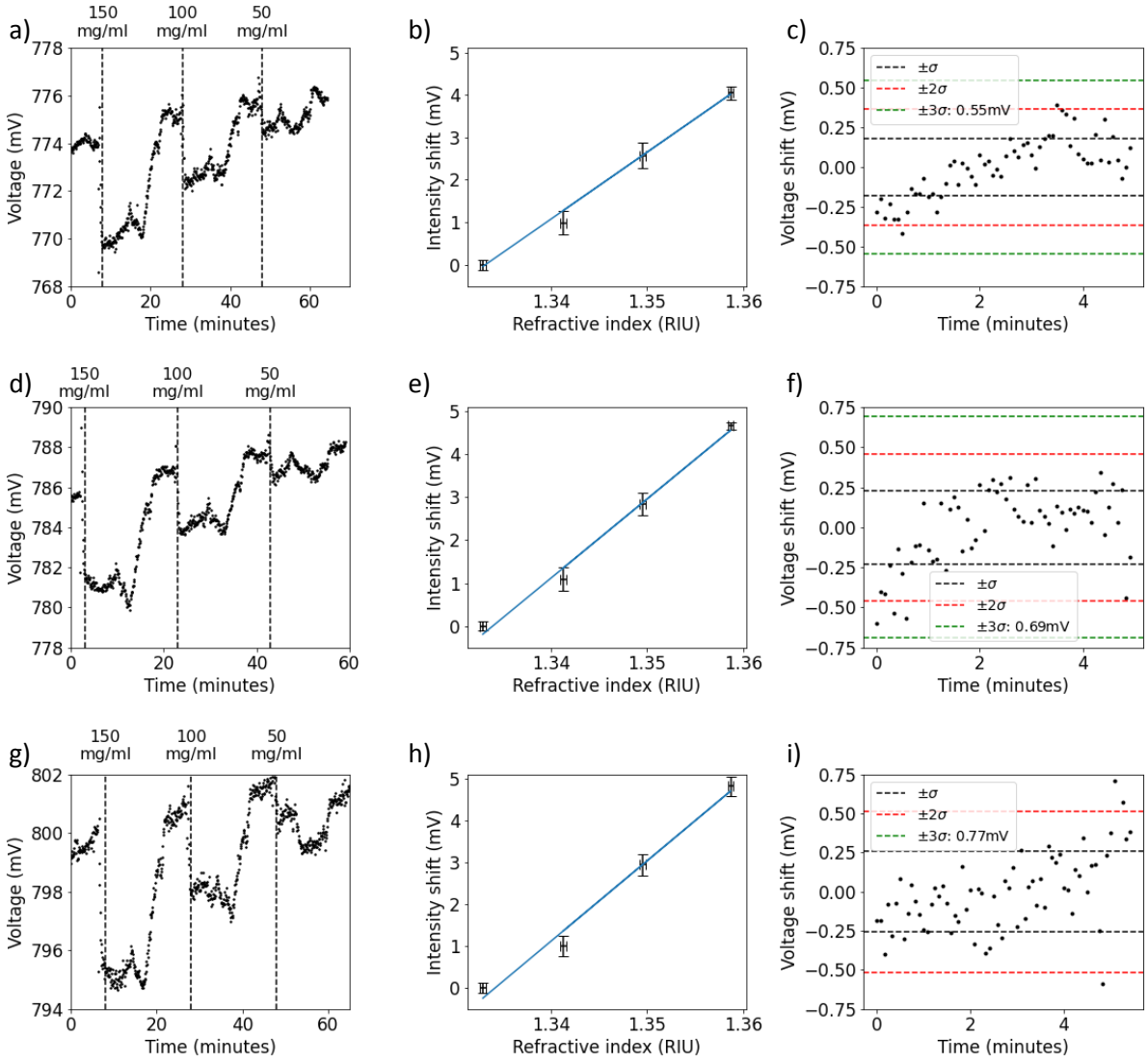

Figure 7.10. Summary of low-cost bulk sensitivity results. Rows are experimental repeats. a, d and g) are voltages measured over time while different concentration salt solutions flow through the fluidics. b, e and h) are the sensitivity graphs of change in voltage as a function of refractive index. c, f and i) are noise floors from each experiment.

As with the two preceding readout configurations, one method of comparing performance is to calculate the smallest refractive change which the setup is capable of resolving: its limit of detection (LoD). The LoD combines a configuration's sensitivity and noise floor, thus eliminating the output shift dimension (eg nm for wavelength or V for volts) and displaying the intrinsic minimum refractive index unit difference which the configuration could detect. The calculated limits of detection are 3.4×10^{-3}, 3.7×10^{-3} and 4.0×10^{-3} RIU showing the limit of detection is reproducible between repeated experiments.

I noted a distinct difference in noise floor when the microcontroller was powered by its battery or by a mains power supply. The above measurements were all performed using the laptop battery and have an average $3\sigma=0.66$mV noise floor. However, the noise floor increased to $3\sigma=0.93$mV when the experiment was powered from the mains supply. From this observation, I infer that a steady current battery power supply reduces the system's electrical noise, which in turn improves its limit of detection. Future iterations of this configuration should therefore employ a stable current source such as a battery.

7.3.6 Comparing research-grade and low-cost results

The primary difference between the research grade and low-cost assemblies is two orders of magnitude in price. The cost of the research grade assembly is dominated by the ~5,000 lock-in amplifier whereas the low-cost electronics cost approximately £50 in total. The low-cost assembly has a limit of detection which is an order of magnitude higher than the research-grade assembly. This decrease in performance with decrease in component cost is to be expected. Comparing the two systems allows reasons for increased noise in the low-cost setup to be identified.

One substantial difference is the reduced lock-in algorithm used by the microcontroller compared to the research-grade assembly. The research-grade system uses a full sine wave as the carrier signal, sampled over multiple points to recover the intensity at this frequency, orthogonal to noise at any other frequency in the system including higher harmonics. In contrast, the microcontroller supplies a digital square wave carrier signal which is sampled at the Nyquist frequency. Using a square carrier wave and sampling at the Nyquist frequency is less robust because it does not reject noise in higher odd harmonics of the carrier frequency.

Another limiting factor is thermal drift. The research-grade lock-in amplifier contains an active cooling system, ensuring sensitive electrical components are thermally stable throughout a measurement.

The microcontroller relies purely on ambient cooling throughout a measurement and became hot to the touch after half an hour of continuous operation. This increase in temperature with continuous operation is indicated by upward drift in the low-cost setup and is known to affect the performance of analog-to-digital converters [143]. Another possible effect of increasing temperature is to decrease the refractive index of water e.g. by ~0.001 RIU between 20 °C and 30 °C [144]. This decrease in refractive index would also cause an upward drift in the device readout voltage.

Despite its limiting factors, the low-cost assembly of the intensity-based readout was able to measure the small refractive index (0.01 RIU) differences between salt solutions and water. The preliminary low-cost setup here may be further improved by, for example, implementing a full sine-wave carrier signal and higher sampling rates. In its form presented here, the low-cost setup achieved a limit of detection only one order of magnitude higher than the research-grade assembly, despite its two orders of magnitude lower price point. The results for this prototype configuration indicate that a competitive limit of detection may well be achievable at a modest price point with further improvements in electronic design.

7.4 Conclusions

The results presented in this chapter provide key information for the quality of the resonance dip and the MIM's performance as a refractive index sensor. A deeper absorption dip is realized by smoother metal surfaces. The smoothest surface in the structure is provided by the commercial single-crystal silver nanocubes, which are smoother than the polycrystalline template-stripped gold films in chapter 3. These smooth films are provided by the relatively cheap, quick and scalable bottom-up fabrication techniques.

The peak wavelength shift may be read either by a spectrometer or by an intensity-based technique. The spectrometer sets the benchmark limit of detection, 5×10^{-4} RIU, to which the research-grade intensity based readout technique compares favorably. The lower-cost setup demonstrates the potential for a compact and handheld system. These sensing results form a large of the MIM's performance description, but this description is still incomplete. Further characterization of the nanocube MIM's ability to detect changes at its surface on the molecular level is required. These experiments and results are presented in the following chapter.

Chapter 8

Nanocube MIM binding experiments

8.1.1 Mercapto-alcohol background

The intended purpose of these refractive index sensors is to detect molecules binding to their surface. Therefore, it is important to extend the sensing experiments beyond bulk sensitivity, into surface sensitivity and molecular binding. One method to further assess the sensor's surface sensitivity is to take simple molecules with one or two functional groups, whose effect on PVP-coated nanocubes is already known. The –SH group, or thiol group, is one such functional group which is known to bind to silver [137] as discussed in chapter 7 and has been shown to displace PVP from a silver nanocube surface [138]. Molecules containing –SH groups are named by either adding the suffix "thiol," or the prefix "mercapto-" in the following sections, consistent with IUPAC naming rules.

Thiols are known to bind to silver and gold [137]. I previously demonstrated that the silver nanocubes adhere to a thiolated surface but are easily rinsed off a non-thiolated surface. Furthermore, alkanethiols form self-assembled monolayers on silver and gold surfaces, the properties of which have been studied since the mid-1980s and are well-understood [145], [146]. First, the thiol group bonds to the metal surface which anchors the molecule in place. Then, the bound molecules pack closely together driven by van-der-Waals interactions between the molecules' carbon chains [147].

The nanocubes are already coated in a molecule: polyvinyl pyridine (PVP), which is attached to the silver cubes by its carbonyl (C=O) group, shown in figure 8.1. Moran et al [138] measured the SERS signal from C=O bond stretching due to its interaction with the silver nanocube surfaces. They observed that adding thiol solutions causes the C=O stretching signal to decrease over a matter of minutes, indicating that thiols replace PVP on silver nanocubes. The PVP can be replaced by a thiol group because the covalent thiolate-metal bond is stronger than the carbonyl-metal interaction. Because of this covalent nature of the thiol bond, the PVP replacement happens on a relatively short timescale.

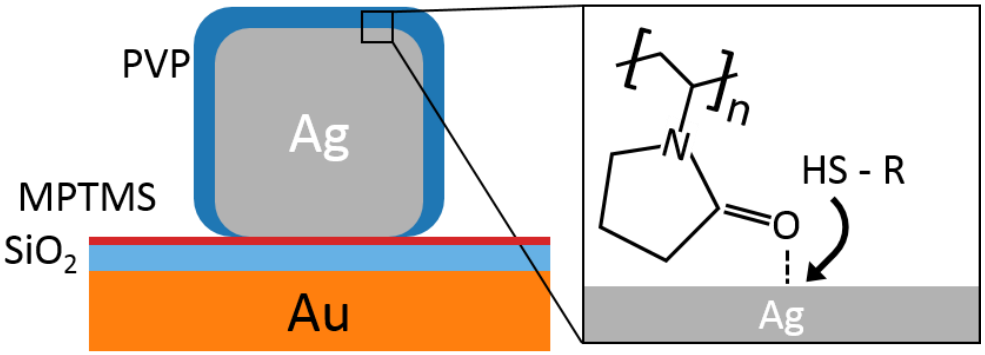

Figure 8.1. Schematic of alkane thiol binding. The left hand side of the figure shows PVP surrounding the silver nanocube placed on the silica-coated gold substrate. The insert on the right shows how an alkane thiol attacks the silver-oxygen dative covalent bond to substitute the PVP on the silver surface. R = $(CH_2)_nOH$, n = 3, 6, 9.

8.1.2 Mercapto-alcohols binding results

I investigated alkane thiol binding and PVP displacement on the nanocube MIM sensor by flowing different concentrations of mercapto-alcohols over the sensor while simultaneously recording reflectance spectra.

Three MIM sensors were prepared simultaneously to minimize fabrication variation between the three mercapto-alcohol experiments shown in figure 8.2. The substrates were template-stripped from the same gold-coated wafer then loaded into the sputterer at the same time for identical silica deposition. The silica-coated substrates were thiolated at the same time in the same container of 4% MPTMS. The same diluted nanocube solution was drop-cast onto each of the three substrates in 25µL volumes for each, and left to dry simultaneously in the same ambient conditions to ensure high consistency between nanocube films across sensor samples.

I used three different mercapto alcohols: 3-mercapto-1-propanol (MCP), 6-mercapto-1-hexanol (MCH) and 9-mercapto-1-nonanol (MCN); their skeletal diagrams are shown in figure 8.2a). These three molecules all have an –SH group at one end of the carbon chain and an –OH alcohol group at the other end of the carbon chain. The alcohol group increases miscibility between the molecule and the aqueous 1M NaCl, 1xTE buffer solution. This buffer solution was selected because it has previously been used to form MCH monolayers on gold surfaces [148], [149]. I prepared solutions of all three mercapto-alcohol molecules in 1.0 and 10 mM concentrations. The solutions were sonicated and gently warmed for 10 minutes before each measurement to ensure that the mercapto-alcohol molecules were well mixed with the buffer solution. I noted that the MCP dissolved after minimal sonication, but the mixture containing larger MCN molecules required more than 5 minutes of sonication to become uniformly mixed.

The experiment proceeded by flowing 1ml of the mercapto alcohol solutions (the analyte solutions) over a MIM sensor using the sealed channel fluidics presented in chapter 3 at a flow rate of 50µL/min with a LEGATO 101 Syringe Pump. 1ml of solution flowing at 50µL/min takes 20 minutes to flow over the sensor surface, allowing sufficient time for silver-thiol binding to occur. After each mercapto alcohol solution, a buffer solution followed for at least 10 minutes to remove any unbound thiol molecules from the sensor surface and the fluidic tubing.

Reflectance spectra were recorded every 10 seconds using a ThorLabs CCS175 Spectrometer. The measurements were normalized to a background spectrum taken from a blank substrate area without any nanocubes. This background spectrum was taken while the sample was in the fluidic assembly with fluid present in order to remove any background reflections resulting from air/glass/fluid interfaces. The spectra acquisition timing was controlled by the ThorLabs OSA software. The peak wavelength was calculated by fitting a Gaussian profile to the reflectance spectrum, the same as in chapter 7. The delay between introducing an analyte solution to the flow system and this analyte solution reaching the sensor surface was accounted for by live-monitoring the peak wavelength shift during the experiment using a LabVIEW fitting program.

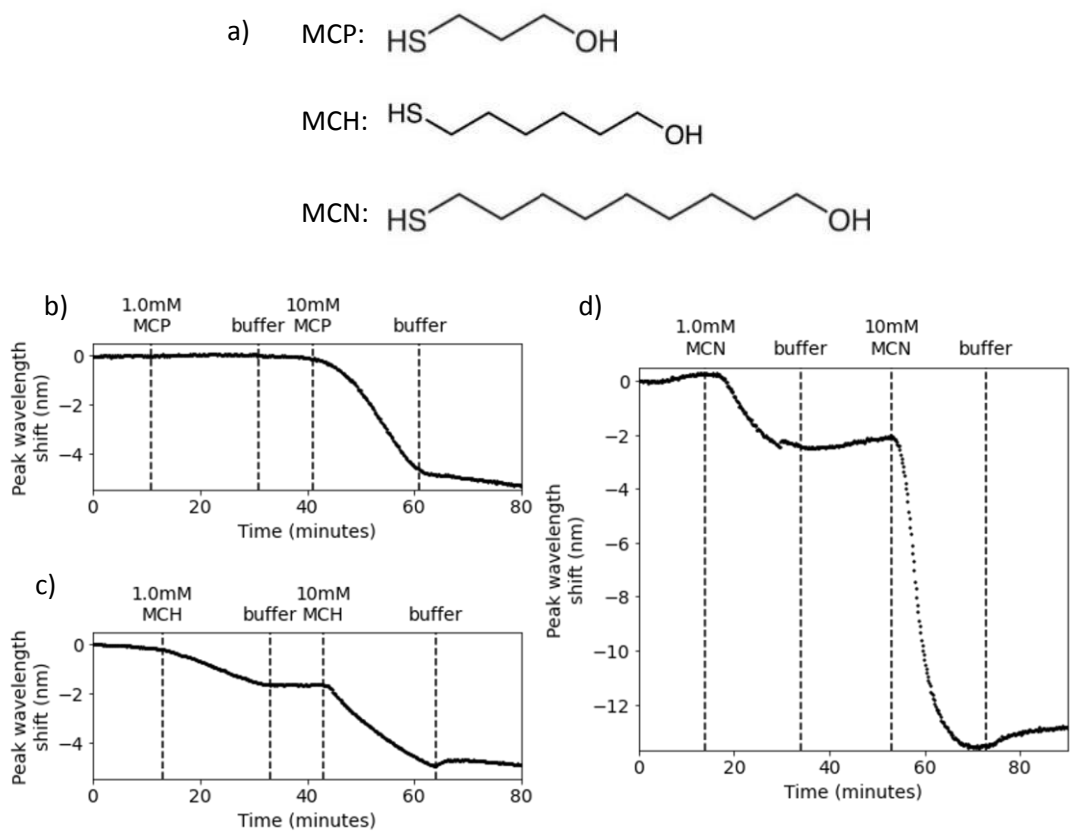

Figure 8.2. PVP displacement from silver nanocube MIM via alkane thiol replacement. a) skeletal diagrams of molecules, labelled by abbreviations. b) ,c) and d) are peak wavelength shift over time for 1.0mM and 10mM concentrations of MCP, MCH and MCN flowed over the nanocube MIM refractive index sensor respectively.

First, consider figure 8.2b). A 1.0mM concentration of MCP does not cause a discernable peak wavelength shift, but increasing the concentration to 10mM causes a 5nm negative shift. The negative peak wavelength shift indicates that there is a net refractive index decrease at the nanocube surface. This negative peak wavelength shift is linear in time and stops abruptly when the flow solution is changed from 10mM MCP back to buffer solution. The discontinuous gradient when changing from 10mM MCP to buffer solution indicates that 10mM MCP flowed for 20 minutes is insufficient to saturate the nanocube surface.

We now move to figure 8.2c). Here, both 1.0mM and 10mM of MCH cause negative peak wavelength shifts of 2nm and 3nm between wash steps, respectively. The larger concentration of MCH causes a larger peak wavelength shift and the gradient of the peak wavelength shift for 10mM is noticeably steeper than the gradient of the 1.0mM concentration. These observations indicate that the reaction on the nanocube surface is proceeding faster for a higher concentration.

Finally, as shown in figure 8.2d), 10mM concentration of MCN causes the largest peak wavelength shift and steepest gradient over time of the three solutions tested. In fact, the peak wavelength shift resulting from 10mM MCN already saturates while MCN is still supplied to the sensor surface. This saturation indicates that a 10mM solution of MCN is sufficient to cause a maximum PVP displacement from the nanocube corners where the MIM resonance probes its surrounding environment.

8.1.3 Trends in mercapto-alcohol nanocube MIM data

We can observe clear trends in the peak wavelength shifts caused by the mercapto-alcohol molecules. The first trend is that a higher concentration of mercapto-alcohol causes a faster peak wavelength shift for all three molecules. The reaction proceeds faster for higher concentrations because there are more thiol molecules colliding with a given area of cube surface per unit time, increasing the macroscopic rate of reaction.

The second trend is that mercapto-alcohol molecules with longer carbon chains cause a higher rate of peak wavelength shift for concentrations of 1.0mM, indicating PVP is displaced more quickly by the formation of a self-assembled monolayer. Interpreted slightly differently, the mercapto alcohol self-assembled monolayer appears to form faster for molecules with longer carbon chains. The energy driving this faster monolayer formation comes from van-der-Waals interactions between the carbon chains, described in section 8.1.1 and ref [147]. The van-der-Waals interaction is proportional to the length of the carbon chain, which explains the trend described here.

10mM of MCN caused the peak wavelength shift to saturate at -12.5nm. This saturated peak wavelength shift, combined with the refractive index and thickness of the PVP layer encourages an estimation of the nanocube MIM's surface sensitivity. PVP has a thickness of 3nm [42], [132] and a refractive index of n=1.52 [150], which is Δn=0.19 RIU greater than water (1.52-1.33 = 0.19), and the molecule far larger than the mercapto alcohol molecules by which it is displaced. Therefore, I assume a 3nm region surrounding the nanocubes undergoes a Δn=0.19RIU change in refractive index which causes a 12.5nm shift and calculate 66nm/RIU surface sensitivity for a 3nm layer on the cube surface. This value of surface sensitivity surpasses the lithography structures which showed 54nm/RIU for a 10nm layer for two reasons. The first reason is that a greater proportion of the first order mode electric field overlaps with the analyte. The second reason is that the cubes have rounded corners at the bottom, which effectively pull the electric field from the insulator layer and into the analyte as discussed in section 6.6.

8.1.4 Limitations of the mercapto alcohol experiments

The accuracy of this 66nm/RIU surface sensitivity estimate may be assessed by comparing the value to other sensitivity values in chapters 6 and 7, and considering the quality of assumptions made. Some assumptions imply the experimental refractive index change is larger than estimated, some assumptions indicate the change is smaller than estimated. The conclusion is that these experiments certainly confirm high surface sensitivity but provide a coarse numerical value for the device performance.

The estimate passes first sanity check: that 66nm/RIU for 3nm thickness is lower than the bulk sensitivity simulated and experimental values (180nm/RIU and 120nm respectively). Furthermore, the estimated value for a 3nm layer index change is somewhere between the simulated 10nm and 3nm thick surface sensitivity values (100nm/RIU and 55nm/RIU respectively). The 3nm PVP at the nanocube corners may be thicker than quoted, resulting in a larger experimental refractive index change than assumed and explaining the discrepancy between simulation and experiment.

The estimate may be innacurate due to two further assumptions. One assumption is that the PVP uniformly covers the nanocubes. However, PVP coverage may well be non-uniform in density, particularly at the nanocube corners where the MIM resonance is most sensitive to changes in refractive index. Another assumption is that the mercapto-alcohol layer has a negligible thickness, when this layer may occupy a significant space within the MIM's evanescent field. However, both of these assumptions actually create a larger refractive index change for the same peak wavelength shift. Therefore, I conclude that this estimate is exactly that: an estimate based on reasonable, but not exact, assumptions and should be treated as a coarse and cautious statement of the nanocube MIM sensor's performance metrics.

While the above trends and maximum -12.5nm shift were consistent across experiments, the exact peak wavelength shifts caused by concentrations of each substance were not reproducible between experiments. I identify a number of factors that limit the experimental reproducibility. The quality of the PVP layer on the dried nanocube films following drop casting may be variable due to limited control of ambient temperature and relative humidity. The longer-chain MCH and MCN substances were not readily soluble in the aqueous buffer owing to their oily 6 and 9 long carbon chains respectively, despite the gentle warming and sonication mentioned in section 8.1.2. The poor solubility of these substances may cause a disparity between their intended and actual

concentrations, especially when diluting a higher concentration of mercapto alcohol solutions to a lower concentration.

8.2 DNA strand attaching to silver nanocube MIM

8.2.1 Thiolated DNA strand binding experiments

The molecular binding experiments were taken further towards detecting biologically relevant molecules by observing the effect of single-stranded DNA (ssDNA) on the nanocube MIM system. DNA is a well-understood system [149], [151], [152] and immobilized DNA strands can be used to detect other DNA strands via hybridization [148] or proteins through highly selective aptasensors [56]. DNA molecules are customizable; custom DNA strands with additional modifications are offered by a number of major suppliers (Integrated DNA Technologies, ThermoFisher Scientific and Sigma Aldrich).

I investigated DNA strands binding to the MIM by comparing two DNA molecules: one molecule which should not bind and another molecule which should bind. An unmodified single DNA strand should not bind to the MIM surface since it does not contain a functional group which would form an attachment to a silver or silica surface. The same DNA sequence can have a thiol attached to one end of the DNA strand, so that it binds to a silver surface via this thiol. In order to confirm this hypothesis, I applied both modified and unmodified DNA molecules to the sensor to determine firstly whether a DNA strand binds to the MIM and secondly if the binding was due to the presence of a thiol on the DNA molecule.

1ml of the 300nM DNA solution[1] in 1xTE 1M NaCl solution was flowed over the MIM sensor using the two part fluidic assembly presented in chapter 3 at a flow rate of 50µL/min with a LEGATO 101 Syringe Pump. 1ml of solution flowing at 50µL/min takes 20 minutes to flow over the sensor surface, allowing sufficient time for silver-thiol binding to occur because the thiolated DNA strand binding curve saturates and shows no further increase after approximately 15 minutes. The buffer solution followed after each DNA solution for at least 10 minutes to remove any unbound DNA molecules from the sensor surface and fluidic tubing.

[1] sequence GAA CAG CCG ACC ACG CAA AGA AGA GAG ACA AGG AAA CAA AAG AGC ACC AGA AAC CAC GA

Figure 8.3 summarizes the DNA binding results. The thiolated DNA causes a 0.3nm positive peak wavelength shift in both instances, whereas the non-thiolated DNA does not cause the peak wavelength to shift appreciably. Figure 8.3c shows a disruption at time t=10, which is due to the mechanical noise caused by inserting a new fluid sample into the fluidic assembly which was not properly secured for this measurement. The sample takes 5 minutes to reach the sensor surface, calibrated from bulk sensitivity measurements in chapter 7.

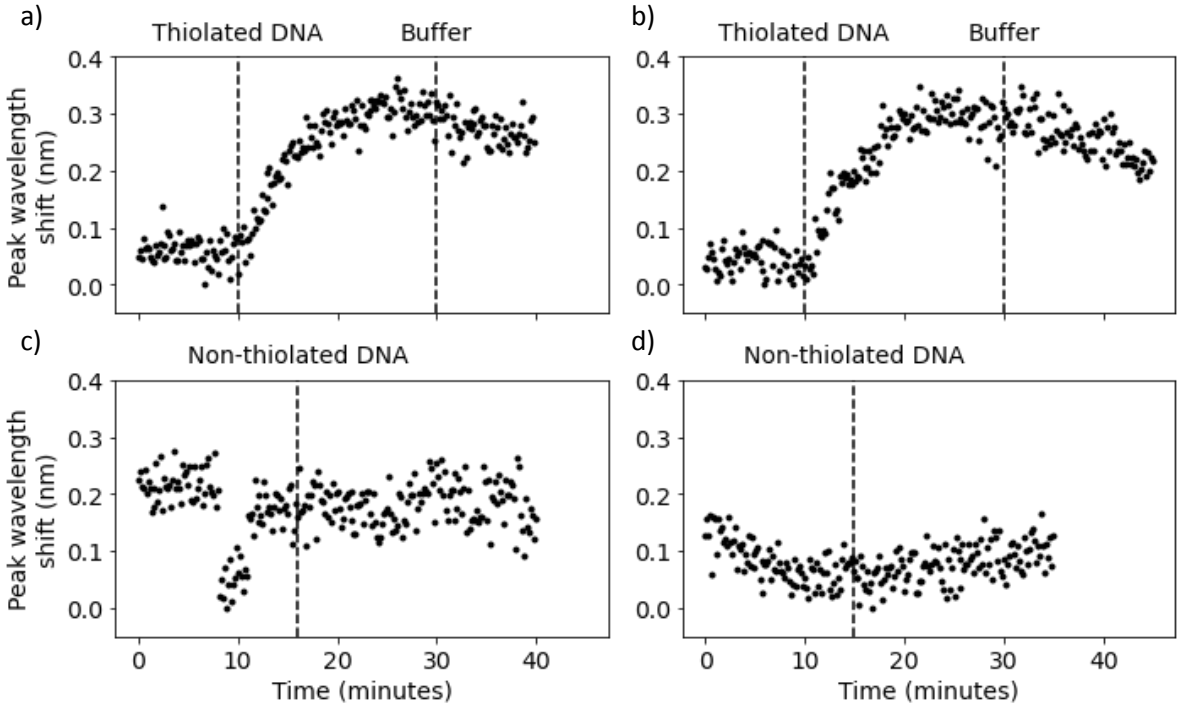

Figure 8.3. Nanocube MIM resonance wavelength shifts resulting from DNA strands flowing over a nanocube MIM surface. a) and b) show a peak wavelength shift for thiolated DNA, whereas b) and c) show no discernible peak wavelength shift for non-thiolated DNA.

8.2.2 DNA binding discussion

First of all, by comparing figure 8.3a,b) to figure 8.3c,d), we note that the non-thiolated DNA does not attach to the surface. This is no surprise, but it is good to confirm that the chemistry behaves as expected.

Secondly, the thiolated DNA clearly binds to the sensor surface, and it does so within about 10 mins, at which point the resonance shift saturates. Once the buffer is introduced, we note a small downward shift, which may be due to a small proportion of the DNA molecules leaving the sensor over time or mechanical drift.

DNA binding causes a positive shift in contrast to the negative shifts observed for the alkane thiols in figure 8.2 for two reasons: the relative size of the molecules and the density of molecules on the silver cube surface.

Firstly, the DNA molecules used here are 18.7 kDa in mass, two orders of magnitude larger than the 134 Da 6-mercapto-1-hexanol. Molecule for molecule, the DNA will occupy a larger volume with a larger mass at the sensor surface than any of the three mercapto alcohol molecules, corresponding to a larger positive change in refractive index.

Secondly, a 300nM concentration of DNA was used which is 4 orders of magnitude less than concentration of alkane thiols used in section 8.1.2. The alkane thiol experiments show that PVP displacement depends on concentration of thiols and at lower concentrations of thiols cause little or no PVP displacement. Therefore, this relatively low concentration of DNA thiol molecules is expected to cause little to no PVP displacement. Instead, the DNA binds to the silver nanocube in the gaps between the non-uniform PVP coating without displacing it.

8.3 Conclusions and further work

The DNA experiments may be extended by, for example, optically detecting DNA hybridization using the MIM refractive index sensor. Here, I provide preliminary quartz crystal microbalance with dissipation (QCM-D) data to inspire confidence in the next researcher who may continue with the MIM sensing experiments.

8.3.1 Preliminary QCM-D DNA hybridization data

The QCM-D detects mass binding to a surface by monitoring the resonant frequency of a quartz crystal. Just as with the time-honored mass on a spring example, an increase in mass serves to decrease the resonant frequency of both the spring and the quartz crystal oscillation. For these preliminary experiments, I replicated the nanocube MIM surface by grafting MPTMS to silica coated QCM-D sensors and drop-casted nanocubes in an identical manner to that with which the optical MIM sensors were prepared.

For this experiment, I prepared 300nM solutions of the thiolated DNA capture strand, complementary DNA strand and non-thiolated DNA capture strand to use in a parallel control experiment. I also prepared 1mM 6-mercapto-1-hexanol solution as a blocking layer to inhibit non-specific binding of the second DNA strands to the silica surface. The above substances were dissolved in 1xTE 1M NaCl buffer solution consistent with previous DNA QCM-D experiments [148], [149].

Figure 8.4 shows QCM-D data for both complementary and non-complementary strands flowing over an initially attached thiolated DNA capture strand. The thiolated DNA strand causes a decrease in frequency for both QCM-D sensors. The complementary DNA strand causes a further decrease in frequency, in stark contrast to the non-complementary control strand which causes no visible change in sensor frequency.

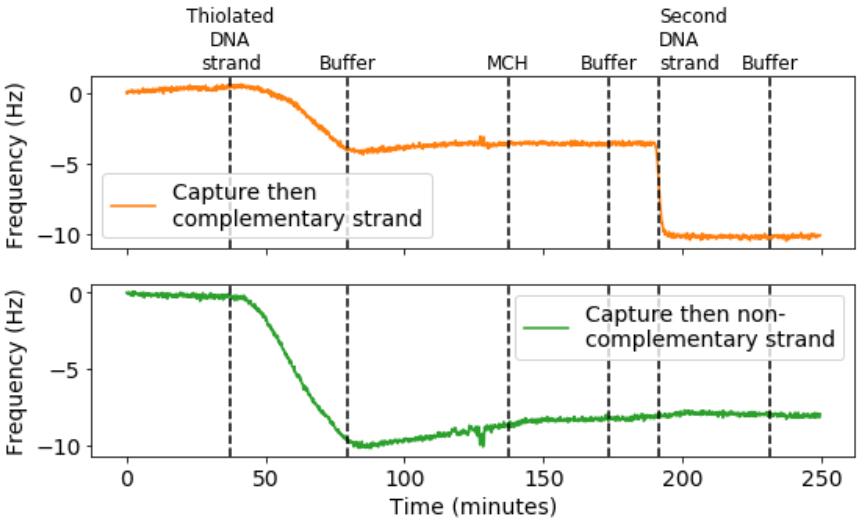

Figure 8.4. Preliminary DNA QCM-D binding experiment indicating hybridisation between complementary DNA strands (top) while there is no change for a non-complementary DNA strand used as control (bottom).

8.3.2 Concluding remarks on binding experiments

In this section I investigated the MIM's surface sensitivity using two different types of molecule: mercapto-alcohols and DNA strands. High concentrations (mM) of small mercapto alcohols displace PVP from the nanocube surface, inducing a negative peak wavelength shift. Low concentrations (nM) of larger DNA molecules bind to the MIM surface alongside the PVP layer which causes a positive peak wavelength shift. A control experiment showed that the modified DNA attaches to the MIM surface by a thiol group, since unmodified DNA without the thiol group causes no peak wavelength shift.

I added further information to these binding experiments by replicating the nanocube MIM surface on a silica QCM-D sensor and demonstrating that performing DNA hybridization on the MIM surface is indeed possible. These preliminary DNA hybridization data motivate further nanocube MIM sensing experiments beyond this PhD project.

Chapter 9

Conclusions and outlook

The original research question of this thesis was **how well do metal-insulator-metal nanoresonators perform as refractive index sensors for detecting molecules?** The thesis concludes with a discursive answer to this question, evidenced by the simulations, fabrication and experiments performed in this work. The discussion includes recommendations for how the next researcher can continue to improve the design, fabrication and application of these MIM refractive index sensors to detect biomolecules.

A refractive index sensor's performance comprises a number of parameters. One vital parameter is its sensitivity to refractive index changes within a (bio) molecule's length of its surface. The collection of simulation and experimental data show that MIM resonators are highly sensitive to refractive index changes within 10nm of their surfaces. The lithography MIM's surface sensitivity was experimentally shown to be 55nm/RIU from sputtering 10nm of silica, in good agreement with the 58nm/RIU value calculated with COMSOL multiphysics. The nanocube MIM's surface sensitivity performance surpasses these values in simulation and experiment. Experiments yield approximately 60nm/RIU from displacing a ~3nm polymer layer surrounding the cubes with alkane thiols. This 60nm/RIU estimate is in broad agreement with the ~50nm/RIU for a 3nm layer shown through COMSOL simulations.

The lithography structures provide two resonant modes, whose sensitivity metrics may be compared. The tightly confined MIM mode shows approximately twice the surface sensitivity that the extended SPP-like mode (55nm/RIU compared with 30nm/RIU), showing that the MIM mode compensates for its lower Q factor with its higher surface sensitivity when compared to the higher Q distributed resonant mode, and that the high bulk sensitivity of the SPP mode is no guarantee of high surface sensitivity.

The physical principles through which the MIMs obtain sensitivity to their surroundings is the overlap between the evanescent electric field and the region in which the refractive index changes. This statement was expressed mathematically in chapter 2 and the semi-analytical wavelength shift predicted simulation results in chapter 6. The prediction accuracy was improved by understanding how the analyte perturbs the evanescent electric field. Specific to the MIM resonator, the E field is found to be sharpest at the base corners of the metal feature where it meets the substrates from E field plots. The sensitivity of the corners in particular was demonstrated using a FEM comsol simulation which confirms the corners are the most sensitive region of the structure.

These sensors should be designed in order to maximise their surface sensitivity. The first order MIM mode is more sensitive than the third order mode because a greater proportion of the total electric field is made up of the evanescent field around the resonator. Therefore, MIM resonant cavities should be tuned to support the first order mode. While accessing this ~75nm length scale is possible with EBL, it proved quicker and easier to fabricate first order resonators with nanoparticles. Drop-casting nanocubes provided a scalable, method to fabricate first order resonators.

The fabrication aims to produce the best quality resonance with the deepest absorption dip. The depth of this absorption feature is increased by considering the metal-insulator interfaces. These

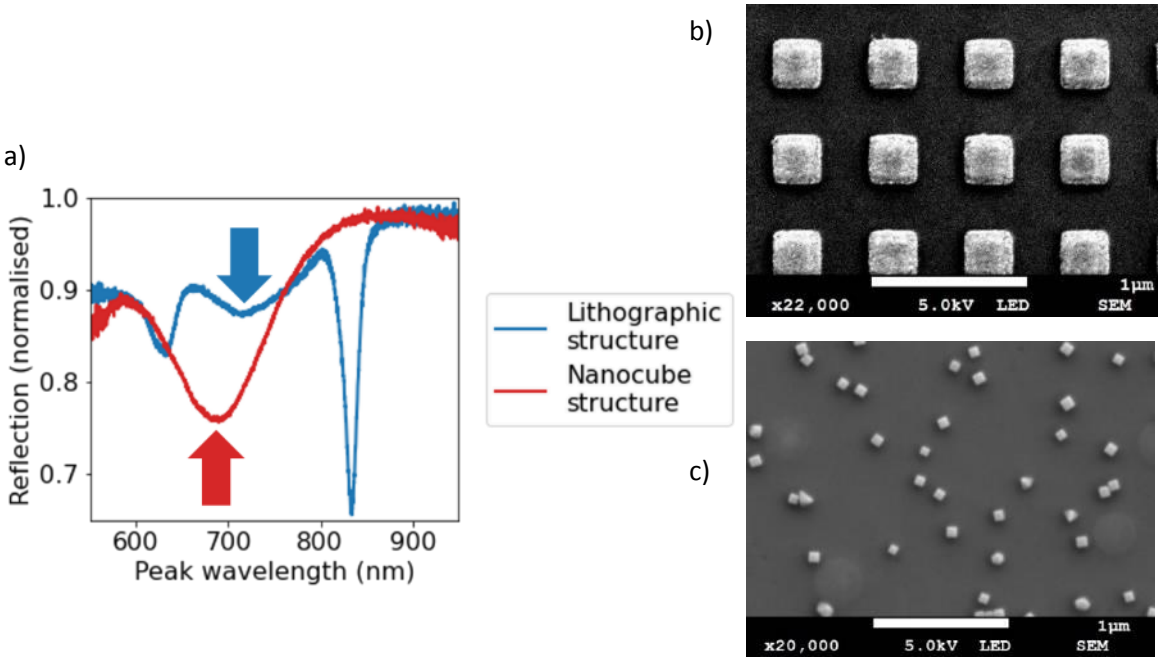

Figure 9.1. Top-down lithographic structures compared with bottom-up nanocube structures. a) Reflection spectra from the two structures with MIM peak indicated by corresponding colour arrow. Density of a) lithographically fabricated and nanocube features forming MIM resonators.

interfaces are formed differently by the top-down lithographic methods and the bottom-up nanocube drop-casting. I identify two differences between interfaces realised by these methods: surface roughness and adhesion layers. The bottom-up nanocube MIM structures show deeper resonance dips due to improvements in both these areas, despite their rarer spatial distribution on the substrate.

Reducing surface roughness was crucial to realising the MIM resonance. Template stripping provided sufficiently smooth films to realise the MIM resonance by lithographically patterning the top metal layer. The evaporator-deposited metal on both sides of the insulator was polycrystalline with valleys and voids between crystal planes. These defects were minimised by employing nanocubes with crystal-plane smooth facets top side of the insulator. The resonance quality could be improved further with similarly crystalline chemically synthesised metal substrate.

The depth of the resonance dip may also be improved by carefully choosing adhesion layers. Simulations in chapter 4 show that even a few nanometres of titanium adhesion layer reduces the depth of the resonance dip, whereas non-absorbing organosilane based adhesion layers such as MPTMS do not. Other transparent adhesion layers such as metal oxides may be used instead of titanium in lithographic fabrication, reducing the adhesion layer absorption and improving the resonance.

I advise the next researcher to start with bottom-up fabrication methods due to their low-cost, smoother surfaces and transparent adhesion layers rather than spending as much time on top-down methods as I did.

Bulk sensitivity experiments proved useful to compare resonators and readout techniques, despite their limited description of a refractive index sensor's performance. Both the lithographically fabricated and nanocube resonators only show modest bulk sensitivity when measured with salt solutions: 78nm/RIU and 122nm/RIU for the lithography and nanocube structures respectively. The ability to monitor resonance wavelength shifts of the structures may be compared by considering the noise floor (3σ values) from their wavelength traces. These 3σ values demonstrate that a resonator with a deeper resonance dip makes smaller peak wavelength shifts resolvable. Tracing the peak wavelength shifts for the lithography peak showed 3σ=0.2nm, whereas using the nanocube structures produced $3\sigma=7.0\times10^{-2}$ nm, approximately a factor 3 lower. The nanocube structures higher bulk

sensitivity and lower 3σ result in their 5.7×10^{-4} RIU limit of detection approximately 5 times lower than the 3.00×10^{-3} RIU limit of detection from the lithography structures.

I show that changes in the nanocube MIM resonance position may be measured using low-cost components. The components do not depreciate the MIM readout performance and are capable of achieving ~5.5×10^{-4} RIU limit of detection when combined with research-grade electronics equipment. This LoD value is remarkably close to the 5.7×10^{-4} RIU bulk limit of detection from spectrometer measurements. I perform the measurement with low-cost electronics, albeit at the expense of reduced performance indicated by the higher 3.7×10^{-3} RIU limit of detection.

I recommend the next researcher improve the low-cost electronics to decrease the limit of detection by resolving even smaller wavelength shifts. One strategy they could use is to increase the digital resolution of the intensity shifts by applying the photodiode output over a wider bit range than the measurements in chapter 7. Scaling the photodiode voltage range can be achieved with a differential amplifier, effectively zooming in on the voltage region of interest.

A second improvement strategy the next researcher could use to increase the low-cost configuration performance is to combine intensity shifts from a plurality of different wavelength LEDs. For example, if two LEDs are spectrally positioned either side of the MIM resonance dip then as the dip wavelength changes, the reflection signal from one LED will increase and the other will decrease. Summing the absolute value of these intensity shifts doubles the change in intensity signal. I make the ansatz that the noise in both these LED signals will be similar and combine in quadrature, increasing the signal by factor 2 while increasing the noise by factor $\sqrt{2}$, therefore increasing the SNR by $\sqrt{2}$.

The intensity-based configuration may be mass-produced with surface-mount components and pick-and-place machines. Surface-mount components are even lower cost and smaller footprint than the TO-18 components used in chapter 7, and are soldered directly onto a PCB. The small footprint (2mm x 1mm) of these PCB-mounted components allow multiple sensing sites to be monitored on the same MIM chip for detecting multiple analytes simultaneously.

The final research question of this work, and possibly the broadest, is how the next researcher could detect specific substances by functionalising the MIM surface. A direction in which thiolated DNA binding results at the end of chapter 8 may be extended is detecting a complementary strand binding to the first thiolated strand attached to the nanocube. Preliminary results of this complementary DNA binding are shown in figure 9.2: a small upward step results from a complementary strand (300nM concentration) hybridising with previously attached capture strand. The mercapto-hexanol (MCH) blocking layer was used to inhibit non-specific binding to the silver cube and also displaced PVP from the surface, evidenced by the negative wavelength shift.

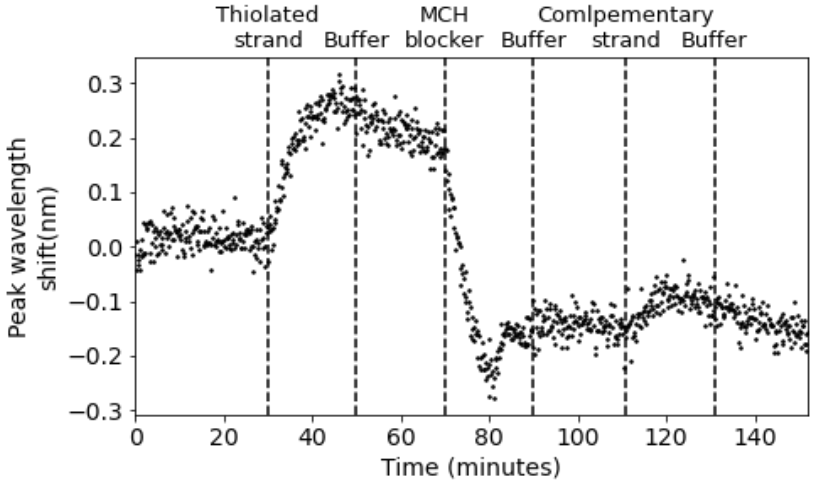

Figure 9.2. Complementary DNA strand binding to a thiolated capture strand, causing the resonance wavelength to increase.

The upward step caused by the complementary strand is not conclusive proof of selective DNA strand detection because it lacks a control experiment showing that a non-complementary strand does not cause a wavelength shift. The surface chemistry also requires optimisation to increase the size of the upward step due to the complementary DNA strand. However, these are preliminary data from which further research may follow.

The next researcher could functionalise the surface of commercial silver nanocubes in this work by simultaneously attaching capture molecules while displacing PVP. The results in chapter 8 indicate that a high concentration of thiolated capture molecules are able to displace the PVP capping layer as they attach to the nanocubes. The MIM structure may then be exposed to the analyte once the capture molecules are bound in order to detect its presence and infer its concentration.

Another option available to the next researcher is to avoid the complication of capping layers all together. Gold nanoparticles often come stabilised in a citrate buffer and are available in many

shapes with facets that could form MIM cavities. Gold and silver nanoparticles both have a wealth of standard surface functionalisation protocols from previous SPR research which could be applied.

Primarily for their high surface sensitivity combined with their potential for a low-cost readout assembly, I determine that **MIM nanoresonators perform competitively as refractive index sensors for detecting molecules.** The simulation and experimental results presented in this work will inform the design and evaluation of the next generation of biosensors.

Bibliography

[1] GE, “SPR Systems,” *General Electric Life Sciences*, 2018. [Online]. Available: https://www.gelifesciences.com/en/gb/solutions/protein-research/products-and-technologies/spr-systems. [Accessed: 12-Dec-2019].

[2] A. G. Brolo, “Plasmonics for future biosensors,” *Nat. Photonics*, vol. 6, no. 11, pp. 709–713, Nov. 2012.

[3] S. A. Maier, *Plasmonics: Fundamentals and Applications*. New York, NY: Springer, 2007.

[4] P. B. Johnson and R. W. Christy, “Optical constants of the noble metals,” *Phys. Rev. B*, vol. 6, no. 12, pp. 4370–4379, Dec. 1972.

[5] P. Lalanne *et al.*, “Quasinormal mode solvers for resonators with dispersive materials,” *J. Opt. Soc. Am. A*, vol. 36, no. 4, p. 686, Nov. 2019.

[6] P. Lalanne, W. Yan, K. Vynck, C. Sauvan, and J. P. Hugonin, “Light Interaction with Photonic and Plasmonic Resonances,” *Laser and Photonics Reviews*, vol. 12, no. 5. Wiley-VCH Verlag, 01-May-2018.

[7] W. Yan, R. Faggiani, and P. Lalanne, “Rigorous modal analysis of plasmonic nanoresonators,” *Phys. Rev. B*, vol. 97, no. 20, p. 205422, May 2018.

[8] N. Kongsuwan, A. Demetriadou, M. Horton, R. Chikkaraddy, J. J. Baumberg, and O. Hess, “Plasmonic Nanocavity Modes: From Near-Field to Far-Field Radiation,” *ACS Photonics*, vol. 7, no. 2, pp. 463–471, Feb. 2020.

[9] M.-C. Estevez, M. A. Otte, B. Sepulveda, and L. M. Lechuga, “Trends and challenges of refractometric nanoplasmonic biosensors: A review,” *Anal. Chim. Acta*, vol. 806, pp. 55–73, Jan. 2014.

[10] S. I. Bozhevolnyi and T. Søndergaard, “General properties of slow-plasmon resonant nanostructures: nano-antennas and resonators,” *Opt. Express*, vol. 15, no. 17, p. 10869, Aug. 2007.

[11] Y. Kurokawa and H. T. Miyazaki, “Metal-insulator-metal plasmon nanocavities: Analysis of optical properties,” *Phys. Rev. B*, vol. 75, p. 035411, 2007.

[12] S. Collin, F. Pardo, and J.-L. Pelouard, “Waveguiding in nanoscale metallic apertures,” *Opt. Express*, vol. 15, no. 7, p. 4310, Apr. 2007.

[13] P. Lalanne, S. Coudert, G. Duchateau, S. Dilhaire, and K. Vynck, “Structural Slow Waves: Parallels between Photonic Crystals and Plasmonic Waveguides,” *ACS Photonics*, vol. 6, no. 1. pp. 4–17, 2019.

[14] H. T. Miyazaki and Y. Kurokawa, “Squeezing visible light waves into a 3-nm-thick and 55-nm-long plasmon cavity,” *Phys. Rev. Lett.*, vol. 96, no. 9, 2006.

[15] M. Kuttge, W. Cai, F. J. García De Abajo, and A. Polman, “Dispersion of metal-insulator-metal plasmon polaritons probed by cathodoluminescence imaging spectroscopy,” *Phys. Rev. B*, vol. 80, p. 033409, 2009.

[16] J. J. Baumberg, J. Aizpurua, M. H. Mikkelsen, and D. R. Smith, “Extreme nanophotonics from ultrathin metallic gaps,” *Nature Materials*, vol. 18, no. 7. Nature Publishing Group, pp. 668–678, 01-Jul-2019.

[17] K. L. Tsakmakidis, O. Hess, R. W. Boyd, and X. Zhang, “Ultraslow waves on the nanoscale,” *Science*, vol. 358, no. 6361. American Association for the Advancement of Science, 20-Oct-2017.

[18] M. Merano, A. Aiello, G. W. ’t Hooft, M. P. van Exter, E. R. Eliel, and J. P. Woerdman, “Observation of Goos-Hänchen shifts in metallic reflection,” *Opt. Express*, vol. 15, no. 24, p. 15928, Nov. 2007.

[19] B. Bahari, R. Tellez-Limon, and B. Kante, “Directive and enhanced spontaneous emission using shifted cubes nanoantenna,” *J. Appl. Phys.*, vol. 120, no. 9, p. 093106, Sep. 2016.

[20] P. K. Aravind and H. Metiu, “The effects of the interaction between resonances in the electromagnetic response of a sphere-plane structure; applications to surface enhanced spectroscopy,” *Surf. Sci.*, vol. 124, no. 2–3, pp. 506–528, Jan. 1983.

[21] G.-C. Li, Q. Zhang, S. A. Maier, and D. Lei, “Plasmonic particle-on-film nanocavities: a versatile platform for plasmon-enhanced spectroscopy and photochemistry,” *Nanophotonics*, vol. 7, no.

12, pp. 1865–1889, Dec. 2018.

[22] K. J. Savage, M. M. Hawkeye, R. Esteban, A. G. Borisov, J. Aizpurua, and J. J. Baumberg, "Revealing the quantum regime in tunnelling plasmonics," *Nature*, vol. 491, no. 7425, pp. 574–577, Nov. 2012.

[23] H. Duan, A. I. Fernández-Domínguez, M. Bosman, S. A. Maier, and J. K. W. Yang, "Nanoplasmonics: Classical down to the nanometer scale," *Nano Lett.*, vol. 12, no. 3, pp. 1683–1689, Mar. 2012.

[24] D. Conteduca *et al.*, "Ultra-high Q/V hybrid cavity for strong light-matter interaction," *APL Photonics*, vol. 2, no. 8, p. 086101, Aug. 2017.

[25] J. H. Lee *et al.*, "Tuning and maximizing the single-molecule surface-enhanced Raman scattering from DNA-tethered nanodumbbells," *ACS Nano*, vol. 6, no. 11, pp. 9574–9584, Nov. 2012.

[26] D. K. Lim, K. S. Jeon, H. M. Kim, J. M. Nam, and Y. D. Suh, "Nanogap-engineerable raman-active nanodumbbells for single-molecule detection," *Nat. Mater.*, vol. 9, no. 1, pp. 60–67, Dec. 2010.

[27] L. Cheng, J. Song, J. Yin, and H. Duan, "Self-assembled plasmonic dimers of amphiphilic gold nanocrystals," *J. Phys. Chem. Lett.*, vol. 2, no. 17, pp. 2258–2262, Sep. 2011.

[28] K. Esashika, R. Ishii, S. Tokihiro, and T. Saiki, "Simple and rapid method for homogeneous dimer formation of gold nanoparticles in a bulk suspension based on van der Waals interactions between alkyl chains," *Opt. Mater. Express*, vol. 9, no. 4, p. 1667, Apr. 2019.

[29] G. Chen *et al.*, "High-purity separation of gold nanoparticle dimers and trimers," *J. Am. Chem. Soc.*, vol. 131, no. 12, pp. 4218–4219, Apr. 2009.

[30] G. Chen *et al.*, "Measuring ensemble-averaged surface-enhanced Raman scattering in the hotspots of colloidal nanoparticle dimers and trimers," *J. Am. Chem. Soc.*, vol. 132, no. 11, pp. 3644–3645, Mar. 2010.

[31] R. Chikkaraddy *et al.*, "Mapping Nanoscale Hotspots with Single-Molecule Emitters Assembled into Plasmonic Nanocavities Using DNA Origami," *Nano Lett.*, vol. 18, no. 1, pp. 405–411, Jan. 2018.

[32] L. Li *et al.*, “Gap-mode excitation, manipulation, and refractive-index sensing application by gold nanocube arrays,” *Nanoscale*, vol. 11, no. 12, pp. 5467–5473, Mar. 2019.

[33] C. Ciracì *et al.*, “Probing the ultimate limits of plasmonic enhancement,” *Science.*, vol. 337, no. 6098, pp. 1072–1074, 2012.

[34] H. T. Miyazaki, T. Kasaya, M. Iwanaga, B. Choi, Y. Sugimoto, and K. Sakoda, “Dual-band infrared metasurface thermal emitter for CO2sensing,” *Appl. Phys. Lett.*, vol. 105, no. 12, p. 121107, Sep. 2014.

[35] A. Cattoni *et al.*, “λ3/1000 plasmonic nanocavities for biosensing fabricated by soft UV nanoimprint lithography,” *Nano Lett.*, vol. 11, no. 9, pp. 3557–3563, Sep. 2011.

[36] G. Duffett, R. Wirth, M. Rayer, E. R. Martins, and T. F. Krauss, “Metal-insulator-metal nanoresonators - Strongly confined modes for high surface sensitivity,” *Nanophotonics*, vol. 9, no. 6, pp. 1547–1552, 2020.

[37] C. Kinnear *et al.*, “Directed Chemical Assembly of Single and Clustered Nanoparticles with Silanized Templates,” *Langmuir*, vol. 34, no. 25, pp. 7355–7363, Jun. 2018.

[38] J. Yang, C. Sauvan, A. Jouanin, S. Collin, J.-L. Pelouard, and P. Lalanne, “Ultrasmall metal-insulator-metal nanoresonators: impact of slow-wave effects on the quality factor,” *Opt. Express*, vol. 20, no. 15, p. 16880, Jul. 2012.

[39] R. Filter, J. Qi, C. Rockstuhl, and F. Lederer, “Circular optical nanoantennas: An analytical theory,” *Phys. Rev. B - Condens. Matter Mater. Phys.*, vol. 85, no. 12, Mar. 2012.

[40] R. Chikkaraddy *et al.*, “How Ultranarrow Gap Symmetries Control Plasmonic Nanocavity Modes: From Cubes to Spheres in the Nanoparticle-on-Mirror,” *ACS Photonics*, vol. 4, no. 3, pp. 469–475, Mar. 2017.

[41] A. Rose *et al.*, “Control of Radiative Processes Using Tunable Plasmonic Nanopatch Antennas,” *Nano Lett.*, vol. 14, no. 8, pp. 4797–4802, Aug. 2014.

[42] T. B. Hoang, G. M. Akselrod, and M. H. Mikkelsen, “Ultrafast Room-Temperature Single Photon Emission from Quantum Dots Coupled to Plasmonic Nanocavities,” *ACS Nano Lett.*, 2015.

[43] G. M. Akselrod *et al.*, “Leveraging nanocavity harmonics for control of optical processes in 2d semiconductors,” *Nano Lett.*, vol. 15, no. 5, pp. 3578–3584, May 2015.

[44] J. Huang, G. M. Akselrod, T. Ming, J. Kong, and M. H. Mikkelsen, “Tailored Emission Spectrum of 2D Semiconductors Using Plasmonic Nanocavities,” *ACS Photonics*, vol. 5, no. 2, pp. 552–558, Feb. 2018.

[45] N. Kongsuwan *et al.*, “Suppressed Quenching and Strong-Coupling of Purcell-Enhanced Single-Molecule Emission in Plasmonic Nanocavities,” *ACS Photonics*, vol. 5, no. 1, pp. 186–191, Jan. 2018.

[46] R. Chikkaraddy *et al.*, “Single-molecule strong coupling at room temperature in plasmonic nanocavities,” *Nature*, 2016.

[47] J. B. Lassiter *et al.*, “Third-Harmonic Generation Enhancement by Film-Coupled Plasmonic Stripe Resonators,” *ACS Photonics*, vol. 1, no. 11, pp. 1212–1217, Nov. 2014.

[48] A. R. L. Marshall *et al.*, “Determining molecular orientation: Via single molecule SERS in a plasmonic nano-gap,” *Nanoscale*, vol. 9, no. 44, pp. 17415–17421, Nov. 2017.

[49] A. R. L. Marshall, M. Roberts, J. Gierschner, J.-S. G. Bouillard, and A. M. Adawi, “Probing the Molecular Orientation of a Single Conjugated Polymer via Nanogap SERS,” *ACS Appl. Polym. Mater.*, vol. 1, no. 5, pp. 1175–1180, May 2019.

[50] A. Lochbaum, Y. Fedoryshyn, A. Dorodnyy, U. Koch, C. Hafner, and J. Leuthold, “On-Chip Narrowband Thermal Emitter for Mid-IR Optical Gas Sensing,” *ACS Photonics*, vol. 4, no. 6, pp. 1371–1380, Jun. 2017.

[51] A. Pors, O. Albrektsen, I. P. Radko, and S. I. Bozhevolnyi, “Gap plasmon-based metasurfaces for total control of reflected light,” *Sci. Rep.*, vol. 3, 2013.

[52] T. Xu, Y.-K. Wu, X. Luo, and L. J. Guo, “Plasmonic nanoresonators for high-resolution colour filtering and spectral imaging,” *Nat. Commun.*, 2010.

[53] J. Peng *et al.*, “Scalable electrochromic nanopixels using plasmonics,” *Sci. Adv.*, vol. 5, no. 5, p. eaaw2205, May 2019.

[54] A. O. Hamza, F. N. Viscomi, J.-S. G. Bouillard, and A. M. Adawi, “Förster Resonance Energy Transfer and the Local Optical Density of States in Plasmonic Nanogaps,” *J. Phys. Chem. Lett.*, vol. 12, no. 5, pp. 1507–1513, Feb. 2021.

[55] N. Liu, M. Mesch, T. Weiss, M. Hentschel, and H. Giessen, “Infrared Perfect Absorber and Its

Application As Plasmonic Sensor," *Nano Lett.*, vol. 10, no. 7, pp. 2342–2348, Jul. 2010.

[56] M. Oliverio, S. Perotto, G. C. Messina, L. Lovato, and F. De Angelis, "Chemical Functionalization of Plasmonic Surface Biosensors: A Tutorial Review on Issues, Strategies, and Costs," *ACS Appl. Mater. Interfaces*, vol. 9, no. 35, pp. 29394–29411, Sep. 2017.

[57] A. Yariv, *Optical Electronics in Modern Communications*, 5th ed. New York: Oxford University Press, 1997.

[58] G. Pitruzzello and T. F. Krauss, "Photonic crystal resonances for sensing and imaging," *Journal of Optics (United Kingdom)*, vol. 20, no. 7. IOP Publishing, p. 073004, 01-Jul-2018.

[59] I. D. Block, N. Ganesh, M. Lu, and B. T. Cunningham, "A Sensitivity Model for Predicting Photonic Crystal Biosensor Performance," *IEEE Sens. J.*, vol. 8, no. 3, pp. 274–280, 2008.

[60] P. K. Sahoo, S. Sarkar, and J. Joseph, "High sensitivity guided-mode- resonance optical sensor employing phase detection," *Sci. Rep.*, vol. 7, p. 7607, 2017.

[61] H. Chen, X. Kou, Z. Yang, W. Ni, and J. Wang, "Shape- and size-dependent refractive index sensitivity of gold nanoparticles," *Langmuir*, vol. 24, no. 10, pp. 5233–5237, May 2008.

[62] I. M. White and X. Fan, "On the performance quantification of resonant refractive index sensors," *Opt. Express*, vol. 16, no. 2, p. 1020, Jan. 2008.

[63] J. Homola, "Surface plasmon resonance sensors for detection of chemical and biological species," *Chemical Reviews*, vol. 108, no. 2. pp. 462–493, Feb-2008.

[64] A. E. Cetin, D. Etezadi, B. C. Galarreta, M. P. Busson, Y. Eksioglu, and H. Altug, "Plasmonic Nanohole Arrays on a Robust Hybrid Substrate for Highly Sensitive Label-Free Biosensing," *ACS Photonics*, vol. 2, no. 8, pp. 1167–1174, Aug. 2015.

[65] J. Yang, H. Giessen, and P. Lalanne, "Simple analytical expression for the peak-frequency shifts of plasmonic resonances for sensing," *Nano Lett.*, vol. 15, no. 5, pp. 3439–3444, May 2015.

[66] M. Schauen, F. Opazo, and R. S, "New Labeling Tools Can Help to Realize the Full Potential of Super-Resolution Microscopy," *Leica Microsystems*, 2013. [Online]. Available: https://www.leica-microsystems.com/science-lab/new-labeling-tools-can-help-to-realize-the-full-potential-of-super-resolution-microscopy/. [Accessed: 18-Jun-2019].

[67] J. Homola, “Present and future of surface plasmon resonance biosensors,” *Anal. Bioanal. Chem.*, vol. 377, no. 3, pp. 528–539, Oct. 2003.

[68] M. Paulsen, S. Jahns, and M. Gerken, “Intensity-based readout of resonant-waveguide grating biosensors: Systems and nanostructures,” *Photonics Nanostructures - Fundam. Appl.*, vol. 26, pp. 69–79, Sep. 2017.

[69] Y. Shen *et al.*, “Plasmonic gold mushroom arrays with refractive index sensing figures of merit approaching the theoretical limit,” *Nat. Commun.*, vol. 4, p. 2381, Aug. 2013.

[70] M. El Beheiry, V. Liu, S. Fan, and O. Levi, “Sensitivity enhancement in photonic crystal slab biosensors,” *Opt. Express*, vol. 18, no. 22, p. 22702, Oct. 2010.

[71] A. Drayton, K. Li, M. Simmons, C. Reardon, and T. F. Krauss, “Performance limitations of resonant refractive index sensors with low-cost components,” *Opt. Express*, vol. 28, no. 22, p. 32239, Oct. 2020.

[72] A. B. González-Guerrero, J. Maldonado, S. Herranz, and L. M. Lechuga, “Trends in photonic lab-on-chip interferometric biosensors for point-of-care diagnostics,” *Anal. Methods*, vol. 8, no. 48, pp. 8380–8394, Dec. 2016.

[73] Z. Altintas, Y. Uludag, Y. Gurbuz, and I. E. Tothill, “Surface plasmon resonance based immunosensor for the detection of the cancer biomarker carcinoembryonic antigen,” *Talanta*, vol. 86, pp. 377–383, Oct. 2011.

[74] S. G. Patching, “Surface plasmon resonance spectroscopy for characterisation of membrane protein–ligand interactions and its potential for drug discovery,” *BBA - Biomembr.*, vol. 1838, pp. 43–55, 2014.

[75] X. Li, M. Soler, C. I. Özdemir, A. Belushkin, F. Yesilköy, and H. Altug, “Plasmonic nanohole array biosensor for label-free and real-time analysis of live cell secretion,” *Lab Chip*, vol. 17, no. 13, pp. 2208–2217, Jun. 2017.

[76] A. E. Cetin *et al.*, “Handheld high-throughput plasmonic biosensor using computational on-chip imaging,” *Light Sci. Appl.*, vol. 3, no. 1, pp. e122–e122, Jan. 2014.

[77] J. Li *et al.*, “Revisiting the Surface Sensitivity of Nanoplasmonic Biosensors,” *ACS Photonics*, vol. 2, no. 3, pp. 425–431, Mar. 2015.

[78] LamdaGen, “LSPR Biosensors.” [Online]. Available: http://lamdagen.com/products/lspr-biosensors/.

[79] D. Gerion and R. Storer, “Mobile/wearable devices incorporating lspr sensors,” US20170370836A1, 2015.

[80] A. F. Gavela, D. G. García, J. C. Ramirez, and L. M. Lechuga, “Last advances in silicon-based optical biosensors,” *Sensors (Switzerland)*, vol. 16, no. 3. MDPI AG, p. 285, 24-Feb-2016.

[81] Y. Zou *et al.*, “Cavity-Waveguide Coupling Engineered High Sensitivity Silicon Photonic Crystal Microcavity Biosensors With High Yield,” *IEEE J. Sel. Top. Quantum Electron.*, vol. 20, no. 4, Jul. 2014.

[82] I. D. Block, L. L. Chan, and B. T. Cunningham, “Photonic crystal optical biosensor incorporating structured low-index porous dielectric,” *Sensors Actuators, B Chem.*, vol. 120, no. 1, pp. 187–193, Dec. 2006.

[83] B. Cunningham, P. Li, B. Lin, and J. Pepper, “Colorimetric resonant reflection as a direct biochemical assay technique,” *Sensors Actuators, B Chem.*, vol. 81, no. 2–3, pp. 316–328, Jan. 2002.

[84] M. Huang, A. A. Yanik, T.-Y. Chang, and H. Altug, “Sub-wavelength nanofluidics in photonic crystal sensors,” *Opt. Express*, vol. 17, no. 26, p. 24224, Dec. 2009.

[85] D. Conteduca, R. Romão, E. R. Martins, and T. F. Krauss, “All-dielectric nanohole array for high-resolution imaging and enhanced sensitivity,” in *2019 Conference on Lasers and Electro-Optics Europe and European Quantum Electronics Conference, CLEO/Europe-EQEC 2019*, 2019.

[86] Y. Nazirizadeh, U. Bog, S. Sekula, T. Mappes, U. Lemmer, and M. Gerken, “Low-cost label-free biosensors using photonic crystals embedded between crossed polarizers,” *Opt. Express*, vol. 18, no. 18, p. 19120, Aug. 2010.

[87] S. Jahns *et al.*, “Handheld imaging photonic crystal biosensor for multiplexed, label-free protein detection,” *Biomed. Opt. Express*, vol. 6, no. 10, p. 3724, Oct. 2015.

[88] A. Tittl *et al.*, “Imaging-based molecular barcoding with pixelated dielectric metasurfaces,” *Science (80-.).*, vol. 360, no. 6393, 2018.

[89] F. Yesilkoy *et al.*, “Ultrasensitive hyperspectral imaging and biodetection enabled by dielectric

metasurfaces," *Nat. Photonics*, vol. 13, no. 6, pp. 390–396, Jun. 2019.

[90] G. J. Triggs, Y. Wang, C. P. Reardon, M. Fischer, G. J. O. Evans, and T. F. Krauss, "Chirped guided-mode resonance biosensor," *Optica*, vol. 4, no. 2, p. 229, Feb. 2017.

[91] K. Li *et al.*, "Extended Kalman Filtering Projection Method to Reduce the 3σ Noise Value of Optical Biosensors," *ACS Sensors*, vol. 5, no. 11, pp. 3474–3482, Nov. 2020.

[92] M. G. Moharam and T. K. Gaylord, "Three-dimensional vector coupled-wave analysis of planar-grating diffraction," *J. Opt. Soc. Am.*, 1983.

[93] G. Yoon and J. Rho, "MAXIM: Metasurfaces-oriented electromagnetic wave simulation software with intuitive graphical user interfaces," *Comput. Phys. Commun.*, vol. 264, p. 107846, Jul. 2021.

[94] V. Liu and S. Fan, "S4 : A free electromagnetic solver for layered periodic structures," *Comput. Phys. Commun.*, vol. 183, no. 10, pp. 2233–2244, Oct. 2012.

[95] J. J. D. Joannopoulos, S. Johnson, J. N. J. Winn, and R. R. D. Meade, *Photonic crystals: molding the flow of light*, Second Edi. Princeton, New Jersey: PRINCETON UNIVERSITY PRESS, 2008.

[96] "COMSOL Multiphysics® v. 5.3." COMSOL AB, Stockholm, Sweden, 2017.

[97] Comsol, *Wave Optics Module User's Guide*, V5.3. Stockholm, Sweden: COMSOL AB, 2017.

[98] R. Chikkaraddy, "Light and Single-molecule Coupling in Plasmonic Nanogaps," University of Cambridge, 2017.

[99] J. Bohdansky, "A universal relation for the sputtering yield of monatomic solids at normal ion incidence," *Nucl. Inst. Methods Phys. Res. B*, vol. 2, no. 1–3, pp. 587–591, Mar. 1984.

[100] P. Sigmund, "Theory of sputtering. I. Sputtering yield of amorphous and polycrystalline targets," *Phys. Rev.*, vol. 184, no. 2, pp. 383–416, Aug. 1969.

[101] Y. Yamamura and H. Tawara, "Energy dependence of ion-induced sputtering yields from monatomic solids at normal incidence," *At. Data Nucl. Data Tables*, vol. 62, no. 2, pp. 149–253, Mar. 1996.

[102] A. Sarangan, *Nanofabrication*. Boca Raton : CRC Press, Taylor & Francis Group, 2017. | Series: Optical sciences and applications of light: CRC Press, 2016.

[103] L. Holland and W. Steckelmacher, “The distribution of thin films condensed on surfaces by the vacuum evaporation method,” *Vacuum*, vol. 2, no. 4, pp. 346–364, Oct. 1952.

[104] M. Morita, T. Ohmi, E. Hasegawa, M. Kawakami, and M. Ohwada, “Growth of native oxide on a silicon surface,” *J. Appl. Phys.*, vol. 68, no. 3, pp. 1272–1281, Aug. 1990.

[105] J. N. Shive and R. L. Weber, *Similarities in Physics*. Bristol: Adam Hilger, 1982.

[106] A. Belkind, A. Freilich, J. Lopez, Z. Zhao, W. Zhu, and K. Becker, “Characterization of pulsed dc magnetron sputtering plasmas,” *New J. Phys.*, vol. 7, no. 1, p. 90, Apr. 2005.

[107] A. Anders, “Tutorial: Reactive high power impulse magnetron sputtering (R-HiPIMS),” *J. Appl. Phys.*, vol. 121, no. 17, p. 117, May 2017.

[108] M. Todeschini, A. Bastos Da Silva Fanta, F. Jensen, J. B. Wagner, and A. Han, “Influence of Ti and Cr Adhesion Layers on Ultrathin Au Films,” *ACS Appl. Mater. Interfaces*, vol. 9, no. 42, pp. 37374–37385, Oct. 2017.

[109] T. G. Habteyes *et al.*, “Metallic adhesion layer induced plasmon damping and molecular linker as a nondamping alternative,” *ACS Nano*, vol. 6, no. 6, pp. 5702–5709, Jun. 2012.

[110] M. Lamy de la Chapelle, H. Shen, N. Guillot, B. Frémaux, B. Guelorget, and T. Toury, “New Gold Nanoparticles Adhesion Process Opening the Way of Improved and Highly Sensitive Plasmonics Technologies,” *Plasmonics*, vol. 8, no. 2, pp. 411–415, Jun. 2013.

[111] R. Fowler and E. A. Guggenheim, “Staatistical Thermodynamics: A version of Statistical Mechanics for Students of Physics and Chemistry,” in *Staatistical Thermodynamics: A version of Statistical Mechanics for Students of Physics and Chemistry*, 1956, p. 124.

[112] C. B. Alcock, V. P. Itkin, and M. K. Horrigan, “Vapour pressure equations for the metallic elements: 298-2500k,” *Can. Metall. Q.*, vol. 23, no. 3, pp. 309–313, Jan. 1984.

[113] C. Min and G. Veronis, “Theoretical investigation of fabrication-related disorders on the properties of subwavelength metal-dielectric-metal plasmonic waveguides,” *Opt. Express*, vol. 18, no. 20, p. 20939, Sep. 2010.

[114] J. H. Park, P. Nagpal, K. M. McPeak, N. C. Lindquist, S.-H. Oh, and D. J. Norris, “Fabrication of Smooth Patterned Structures of Refractory Metals, Semiconductors, and Oxides via Template Stripping,” *ACS Appl. Mater. Interfaces*, vol. 5, no. 19, pp. 9701–9708, Oct. 2013.

[115] K. M. Mcpeak *et al.*, “Plasmonic Films Can Easily Be Better: Rules and Recipes,” *ACS Photonics*, vol. 2, p. 12, 2015.

[116] S. Coudert, G. Duchateau, S. Dilhaire, and P. Lalanne, “Attenuation of slow Metal-Insulator-Metal plasmonic waveguides, from Joule absorption to roughness-induced backscattering,” Oct. 2018.

[117] A. K. Au, W. Lee, and A. Folch, “Mail-order microfluidics: Evaluation of stereolithography for the production of microfluidic devices,” *Lab Chip*, vol. 14, no. 7, pp. 1294–1301, Apr. 2014.

[118] N. Bhattacharjee, A. Urrios, S. Kang, and A. Folch, “The upcoming 3D-printing revolution in microfluidics,” *Lab on a Chip*, vol. 16, no. 10. Royal Society of Chemistry, pp. 1720–1742, 10-May-2016.

[119] M. F. Limonov, M. V. Rybin, A. N. Poddubny, and Y. S. Kivshar, “Fano resonances in photonics,” *Nat. Photonics*, vol. 11, no. 9, pp. 543–554, Sep. 2017.

[120] J. R. Mejía-Salazar and O. N. Oliveira, “Plasmonic Biosensing,” *Chemical Reviews*, vol. 118, no. 20. American Chemical Society, pp. 10617–10625, 24-Oct-2018.

[121] J. Vörös, “The density and refractive index of adsorbing protein layers,” *Biophys. J.*, vol. 87, no. 1, pp. 553–561, 2004.

[122] Linus Andersson, “Fillet Away Your Electromagnetic Field Singularities,” *COMSOL Blog*, 2014. [Online]. Available: https://uk.comsol.com/blogs/fillet-away-your-electromagnetic-field-singularities/. [Accessed: 17-Feb-2021].

[123] Raith GmbH, “Electron beam lithography system VOYAGER,” 2020. [Online]. Available: https://www.raith.com/products/voyager.html. [Accessed: 14-May-2020].

[124] S. Prakash and J. Yeom, *Nanofluidics and Microfluidics: Systems and Applications*. Elsevier Inc., 2014.

[125] E. Hecht, *Optics*. Addison-Wesley, 2002.

[126] M. Nayfeh, *Fundamentals and applications of nano silicon in plasmonics and fullerines: Current and future trends*. Elsevier, 2018.

[127] Y. Chen, K. Peng, and Z. Cui, “A lift-off process for high resolution patterns using PMMA/LOR

resist stack," *Microelectron. Eng.*, vol. 73–74, pp. 278–281, Jun. 2004.

[128] G. J. Triggs, "Resonant Grating Surfaces for Biosensing," York, 2016.

[129] L. A. Reeves, "Studies of Novel Gain Materials and Resonant Light Emitters for Silicon Photonics," University of York, 2019.

[130] N. Vogel, J. Zieleniecki, and I. Köper, "As flat as it gets: ultrasmooth surfaces from template-stripping procedures," *Nanoscale*, vol. 4, no. 13, p. 3820, Jun. 2012.

[131] K. F. (Kenneth F. Riley, M. P. (Michael P. Hobson, and S. J. (Stephen J. Bence, *Mathematical methods for physics and engineering*. Cambridge University Press, 2006.

[132] G. M. Akselrod *et al.*, "Probing the mechanisms of large Purcell enhancement in plasmonic nanoantennas," *Nat. Photonics*, 2014.

[133] R. D. Deegan, O. Bakajin, T. F. Dupont, G. Huber, S. R. Nagel, and T. A. Witten, "Capillary flow as the cause of ring stains from dried liquid drops," *Nature*, vol. 389, no. 6653, pp. 827–829, 1997.

[134] P. K. Gothe, D. Gaur, and V. G. Achanta, "Mptms self-assembled monolayer deposition for ultra-thin gold films for plasmonics," *J. Phys. Commun.*, vol. 2, no. 3, p. 035005, Mar. 2018.

[135] T. Siegfried, Y. Ekinci, O. J. F. Martin, and H. Sigg, "Engineering Metal Adhesion Layers That Do Not Deteriorate Plasmon Resonances," *ACS Nano*, vol. 7, no. 3, pp. 2751–2757, Mar. 2013.

[136] A. K. Mahapatro, A. Scott, A. Manning, and D. B. Janes, "Gold surface with sub-nm roughness realized by evaporation on a molecular adhesion monolayer," *Appl. Phys. Lett.*, vol. 88, no. 15, p. 151917, Apr. 2006.

[137] A. H. Pakiari and Z. Jamshidi, "Nature and strength of MS bonds (M = Au, Ag, and Cu) in binary alloy gold clusters," *J. Phys. Chem. A*, vol. 114, no. 34, pp. 9212–9221, Sep. 2010.

[138] C. H. Moran, M. Rycenga, Q. Zhang, and Y. Xia, "Replacement of poly(vinyl pyrrolidone) by thiols: A systematic study of Ag nanocube functionalization by surface-enhanced raman scattering," *J. Phys. Chem. C*, vol. 115, no. 44, pp. 21852–21857, Nov. 2011.

[139] Texas Instruments, *AN-31 amplifier circuit collection*. Texas Instruments, 2020.

[140] A. A. Dorrington and R. Künnemeyer, "A simple microcontroller based digital lock-in amplifier

for the detection of low level optical signals," in *Proceedings - 1st IEEE International Workshop on Electronic Design, Test and Applications, DELTA 2002*, 2002, pp. 486–488.

[141] J. C. . Lesurf, *Information and Measurement*. CRC Press, 2018.

[142] Texas Instruments, "Analog Engineer's - Circuit Cookbook : Op Amps," First., Texas Instruments, 2018.

[143] B. Lizon, *Fundamentals of Precision ADC Noise Analysis*. Texas Instruments, 2020.

[144] K. V. Larin, M. Motamedi, R. O. Esenaliev, T. Akkin, and T. E. Milner, "Phase-sensitive optical low-coherence reflectometry for the detection of analyte concentrations," *Appl. Opt. Vol. 43, Issue 17, pp. 3408-3414*, vol. 43, no. 17, pp. 3408–3414, Jun. 2004.

[145] M. H. Schoenfisch and J. E. Pemberton, "Air stability of alkanethiol self-assembled monolayers on silver and gold surfaces," *J. Am. Chem. Soc.*, vol. 120, no. 18, pp. 4502–5413, May 1998.

[146] B. M. Boeckl and D. Graham, "Self-Assembled Monolayers : Advantages of Pure Alkanethiols Self-Assembly : From Nature to The Lab Self-Assembly : Purity Matters," *Mater. Matters*, pp. 2–5, 2006.

[147] J. C. Love, L. A. Estroff, J. K. Kriebel, R. G. Nuzzo, and G. M. Whitesides, "Self-assembled monolayers of thiolates on metals as a form of nanotechnology," *Chemical Reviews*, vol. 105, no. 4. American Chemical Society , pp. 1103–1169, Apr-2005.

[148] K. E. Dunn, M. A. Trefzer, S. Johnson, and A. M. Tyrrell, "Assessing the potential of surface-immobilized molecular logic machines for integration with solid state technology," *BioSystems*, vol. 146, pp. 3–9, Aug. 2016.

[149] K. E. Dunn, M. A. Trefzer, S. Johnson, and A. M. Tyrrell, "Investigating the dynamics of surface-immobilized DNA nanomachines," *Sci. Rep.*, vol. 6, no. 1, pp. 1–10, Jul. 2016.

[150] T. A. F. König *et al.*, "Electrically tunable plasmonic behavior of nanocube-polymer nanomaterials induced by a redox-active electrochromic polymer," *ACS Nano*, vol. 8, no. 6, pp. 6182–6192, Jun. 2014.

[151] J. N. Zadeh *et al.*, "NUPACK: Analysis and design of nucleic acid systems," *J. Comput. Chem.*, vol. 32, no. 1, pp. 170–173, Jan. 2011.

[152] J. Juan-Colás, T. F. Krauss, and S. D. Johnson, “Real-Time Analysis of Molecular Conformation Using Silicon Electrophotonic Biosensors,” *ACS Photonics*, vol. 4, no. 9, pp. 2320–2326, Sep. 2017.

[153] J. W. Stewart, J. H. Vella, W. Li, S. Fan, and M. H. Mikkelsen, “Ultrafast pyroelectric photodetection with on-chip spectral filters.”